UNIVERSITY OF CALIFORNIA

Los Angeles

Transport Study of Three-Dimensional Topological Insulators

A dissertation submitted in partial satisfaction of the

requirements for the degree Doctor of Philosophy

in Electrical Engineering

by

Murong Lang

2015

ABSTRACT OF THE DISSERTATION

Transport Study of Three-Dimensional Topological Insulators

by

Murong Lang

Doctor of Philosophy in Electrical Engineering

University of California, Los Angeles, 2015

Professor Kang L. Wang, Chair

The recently discovered time-reversal-invariant topological insulator (TI) has led to the flourishing of unique physics along with promises for innovative electronic and spintronic applications. However, the as-grown TI materials are not truly insulating but with a non-trivial bulk carrier density, which makes difficulties to the transport methods. In our work, we study the fundamental transport properties of TI and its heterostructure, in which various approaches are utilized to better reveal the surface state properties. In particular, in Chapter 2, *in-situ* Al surface passivation of Bi_2Se_3 inside MBE is investigated to inhibit the degradation process, reduce carrier density and reveal the pristine topological surface states. In contrast, we show the degradation of surface states for the unpassivated control samples, in which the 2D carrier density is increased by 39.2% due to ambient *n*-doping, the Shubnikov-de Hass oscillations are completely absent, and a deviation from weak

antilocalization is observed. In Chapter 3, through optimizing the material composition to achieve bulk insulating state, we present the ambipolar effect in 4-9 quintuple layers $(B_{i0.57}Sb_{0.43})_2Te_3$ thin films. We also demonstrate the evidence of a hybridized surface gap opening in $(B_{i0.57}Sb_{0.43})_2Te_3$ sample with thickness below six quintuple layers through transport and scanning tunneling spectroscopy measurements. By effective tuning the Fermi level via gate-voltage control, we unveil a striking competition between weak antilocalization and weak localization at low magnetic fields in nonmagnetic ultrathin films. In Chapter 4, we study the magnetic properties of Bi_2Se_3 surface states in the proximity of a high T_c ferrimagnetic insulator YIG. Proximity-induced magnetoresistance loops are observed by transport measurements with out-of-plane and in-plane magnetic fields applied. More importantly, a magnetic signal from the Bi_2Se_3 up to 130 K is clearly observed by magneto-optical Kerr effect measurements. Our results demonstrate the proximity-induced TI magnetism at higher temperatures, which is an important step toward room-temperature application of TI-based spintronic devices.

The engineering of a TI and FMI heterostructure will open up numerous opportunities to study high temperature TI-based spintronic devices, in which the TI is controlled by breaking the TRS using a FMI with perpendicular magnetization component. A YIG film with out-of-plane anisotropy at > 300 K could potentially manipulate the magnetic properties of a TI may even above room temperature.

The dissertation of Murong Lang is approved.

Oscar M. Stafsudd

Louis Bouchard

Kang L. Wang, Committee Chair

University of California, Los Angeles

2015

Table of Contents

List of Figures

Acknowledgements

First of all, I would like to express my sincere gratitude to Professor Kang L. Wang, my PhD advisor, for providing me excellent opportunities as well as valuable resources to conduct research in the topological insulator field. Without his patient guidance and persistent help and caring throughout the years in Device Research lab, this dissertation would not have been written. His enthusiasm and rigorous attitude in physics and engineering inspire me a lot and make me become a productive researcher. I am sure that I will benefit a lot in my future career life from the knowledge, experience, profession and personality I learned from my advisor.

I also wish to thank Professor Oscar M. Stafsudd, Professor Louis Bouchard and Professor Benjamin Williams for their valuable suggestions and comments, and spending their precious time serving in my committee. I especially appreciate the collaboration with Prof. Caroline A. Ross and her PhD student Mehmet C. Onbasli for continuously providing us high quality YIG films and support our research projects. Without Prof. Yong Wang and his student Ying Jiang's effort at Zhejiang University, we could never obtain such beautiful TEM figures for publications. Moreover, I would also like to acknowledge Dr. Eun Sang Choi for his help with our measurements in National high magnetic field lab at Tallahassee.

Special thanks go to all my DRL colleagues. I really learned a lot from every one of you. Appreciation goes to our previous members Professor Liang He, Professor Faxian Xiu, who led me into the field of topological insulators. I also greatly appreciate Dr. Yi Zhou and Dr.

Kin Wong for their fabrication training in my earlier days of PhD study. I particularly would like to express my gratitude to my dear colleagues Xufeng Kou, Yabin Fan, Mohammad Montazeri, Li-Te Chang, Jianshi Tang, Pramey Upadhyaya, who provide me with helpful technique support as well as fruitful discussions.

Finally, there are no words in the world to express my deepest gratitude to my parents and my husband. Their unlimited love, understanding, support and encouragement guided my life over the years.

Vita

Education

M.S. in Electrical Engineering Nov. 2011

University of California, Los Angeles, United States

B.S. in Electrical Engineering June. 2009

Zhejiang University, Hangzhou, China

Publications (*co-first author)

1. **M. Lang**, M. Montazeri, M. Onbasli, X. Kou, *et al.*, Proximity Induced High Temperature Magnetic Order in Topological Insulator-Ferrimagnetic Insulator Heterostructure, ***Nano Letters*** 14 (6) 3459–3465 (2014).
2. **M. Lang**, L. He, X. Kou, P. Upadhyaya, *et al*., Competing weak localization and weak antilocalization in ultrathin topological insulators, ***Nano Letters*** 13 (1), 48–53 (2013).
3. **M. Lang**, L. He, F. Xiu, X. Yu, J. Tang, *et al*., Revelation of topological surface states in Bi_2Se_3 thin films by *in situ* Al passivation, ***ACS Nano*** *6*, 295–302 (2012).
4. L. He,* X. Kou,* **M. Lang**,* E. S. Choi, *et al.*, Evidence of the two surface states of $(Bi_{0.53}Sb_{0.47})_2Te_3$ films grown by van der Waals epitaxy, ***Scientific reports*** 3 (2013).
5. X. Kou,* L. He,* **M. Lang**,* Y. Fan, *et al*., Manipulating surface-related ferromagnetism in modulation-doped topological insulators, ***Nano Letters*** 13 (10), 4587-4593 (2013).

6. X. Kou, **M. Lang**, Y. Fan, Y. Jiang, T. Nie, J. Zhang, *et al.*, Interplay between different magnetisms in Cr-doped topological insulators, ***ACS Nano*** 7 (10), 9205-9212, (2013).
7. Y. Fan, P. Upadhyaya , X. Kou, **M. Lang**, S. Takei, *et al*., Magnetization Switching via Giant Spin-Orbit Torque in a Magnetically Doped Topological Insulator Heterostructure, ***Nature material*** 13, 699-704, (2014).
8. X. Kou, Y. Fan, **M. Lang**, P. Upadhyaya, K. Wang, Magnetic topological insulators and quantum anomalous hall effect, ***Solid State Communications*** (2014).
9. T. Nie, X. Kou, J. Tang, Y. Fan, **M. Lang**, L. Chang, C. Chu, L. He, *et al.*, Superlattice of Fe_xGe_{1-x} nanodots and nanolayers for spintronics application, ***Nanotechnology*** 25 (50), 505702, (2014)
10. X. Yu, L. He, **M. Lang**, W. Jiang, F. Xiu, Z. Liao, Y. Wang, *et al*., Separation of top and bottom surface conduction in Bi_2Te_3 thin films, ***Nanotechnology*** 24, 015705, (2013).
11. F. Xiu, L. He, Y. Wang, L. Cheng, L. T. Chang, **M. Lang**, G. Huang, *et al.*, Manipulating surface states in topological insulator nanoribbons, ***Nature Nanotechnology*** 6, 216-221 (2011).
12. G. Yu, P. Upadhyaya, Y. Fan, J. Alzate, W. Jiang, K. Wong, S. Takei, S. Bender, L. T. Chang, Y. Jiang, **M. Lang**, *et al.*, Switching of perpendicular magnetization by spin-orbit torques in the absence of external magnetic fields, ***Nature Nanotechnology*** 9, 548-554 (2014).

13. W. Jiang, P. Upadhyaya, Y. Fan, J. Zhao, M. Wang, L. T. Chang, **M. Lang**, *et al*., Direct imaging of thermally driven domain wall motion in magnetic insulators, ***Physical Review Letters*** 110 (17), 177202 (2013).

14. X. Kou, W. Jiang, **M. Lang**, F. Xiu, L. He, Y. Wang, *et al*., Magnetically doped semiconducting topological insulators, ***Journal of Applied Physics*** 112 (2012).

15. Y. Wang, F. Xiu, L. Cheng, L. He, **M. Lang**, J. Tang, X. Kou, *et al*., Gate-controlled surface conduction in Na-doped Bi_2Te_3 topological insulator nanoplates, ***Nano Letters*** 12 (3), 1170–1175(2012).

16. W. Jiang, Y. Fan, P. Upadhyaya, **M. Lang**, *et al*., Mapping the domain wall pinning profile by stochastic imaging reconstruction, ***Physical Review B*** 87 (1), 014427 (2013).

17. M. Wang, E.B. Song, S. Lee, J. Tang, **M. Lang**, C. Zeng, *et al*., Quantum dot behavior in bilayer graphene nanoribbons, ***ACS Nano*** 5, 8769 (2011).

18. J. Tang, C. Y. Wang, F. Xiu, **M. Lang**, L. W. Chu, *et al.*, Oxide-confined formation of germanium nanowire heterostructures for high-performance transistors, ***ACS Nano*** 5, 6008 (2011).

19. L. He, F. Xiu, Y. Wang, G. Huang, X. Kou, **M. Lang**, W. P. Beyermann, J. Zou, K. Wang, Epitaxial growth of Bi_2Se_3 topological insulator thin films on Si (111), ***Journal of Applied Physics,*** 109, 103702 (2011).

20. X. Kou, L. He, F. Xiu, **M. Lang**, Z. Liao, Y. Wang, *et al*., Epitaxial growth of high mobility Bi_2Se_3 thin films on CdS, ***Applied Physics Letters***, 98, 242102 (2011).

21. F. Xiu, N. Meyer, X. Kou, L. He, **M. Lang**, Y. Wang, X. Yu, *et al*., Quantum capacitance in topological insulators, ***Scientific Reports***, 2:669 1-7 (2012).
22. L. He, F. Xiu, X. Yu, M. Teague, W. Jiang, Y. Fan, X. Kou, **M. Lang,** Y Wang, *et al.*, Surface-dominated conduction in a 6 nm thick Bi_2Se_3 Thin Film, ***Nano letters*** 12 (3), 1486-1490 (2012)
23. K. Wang, Y. Liu, W. Wang, N. Meyer, L. Bao, L. He, **M. Lang**, Z. Chen, *et al.*, High-quality Bi_2Te_3 thin films grown on mica substrates for potential optoelectronic applications, ***Applied Physics Letters*** 103 (3), 031605
24. C. Zeng, M. Wang, Y. Zhou, **M. Lang,** B. Lian, *et al*., Tunneling spectroscopy of metal-oxide-graphene structure, ***Applied Physics Letter*** 97, 032104 (2010).
25. E. Song, B. Lian, G. Xu, B. Yuan, C. Zeng, A. Chen, M. Wang, S. Kim, **M. Lang**, Y.Zhou, and K. Wang, Visibility and Raman spectroscopy of mono and bilayer graphene on crystalline silicon, ***Applied Physics Letters*** 96 (8), 081911 (2010).

Conferences

1. **M. Lang**, X. Kou, Y. Fan, *et al*., Proximity induced high temperature magnetic order in topological insulator and YIG heterostructure, INC 10, Gaithersburg, Maryland, 2014
2. **M. Lang**, M. C. Onbasli, K. Yao, *et al.*, Proximity-induced magnetoresistance in topological insulator thin films on YIG, 58th MMM, Denver, Colorado, 2013

3. **M. Lang**, L. He, X. Kou, *et al.*, Competing weak localization and weak antilocalization in ultrathin topological insulators, APS march meeting, Baltimore, Maryland, 2013
4. **M. Lang**, L. He, X Yu, *et al.*, Clear revelation of topological surface states in Bi_2Se_3 thin films by *in situ* Al passivation, APS march meeting, Boston, Massachusetts, 2012
5. M. Montazeri, **M. Lang**, M. Onbasli, *et al.*, Proximity effect induced magnetoresistance hysteresis loops in a topological insulator/YIG heterostructure, APS march meeting, Denver, Colorado, 2014
6. Y. Fan, P. Upadhyaya, X. Kou, **M. Lang**, S. Takei, *et al.*, Magnetization Switching via Giant Spin-Orbit Torque in a Magnetically Doped Topological Insulator Heterostructure, APS march meeting, Denver, Colorado, 2014
7. T. Nie, X. Kou, Y. Fan, J. Tang, S. Lee, **M. Lang**, C. Chu, *et al.*, MBE Growth of Si/MnGe Quantum Dot Superlattice with Curie Temperature beyond 400 K, APS march meeting, Denver, Colorado, 2014
8. L. He, X. Kou, **M. Lang**, K. Wang, *et al.*, Evidence of the two surface states of $(Bi_{0.53}Sb_{0.47})_2Te_3$ films grown by van der Waals, APS march meeting, Denver, Colorado, 2014
9. C. Chen, M. Teague, N. Woodward, N. Yeh, L. He, X. Kou, **M. Lang**, *et al.*, Scanning tunneling spectroscopic (STS) studies of the bulk magnetic doping effects on the surface state of Bi_2Se_3, APS march meeting, Denver, Colorado, 2014

10. H Chu, M Teague, CC Chen, N Woodward, NC Yeh, X Kou, L He, **M Lang**, *et al.*, Scanning tunneling spectroscopic (STS) studies of magnetically doped MBE-grown topological insulators (TIs), APS march meeting, Baltimore, Maryland, 2013
11. X. Kou, L. He, **M. Lang**, Y. Fan, Y. Jiang, *et al.*, Manipulating Surface-induced Ferromagnetism in Modulation-doped Topological Insulators, APS march meeting, Boston, Massachusetts, 2012
12. L. He, X. Yu, X. Kou, **M. Lang**, K. Wang, *et al.*, Surface-dominated conduction in a 6nm-thick Bi_2Se_3 thin film, APS march meeting, Boston, Massachusetts, 2012

Awards

- 2012-2013 Qualcomm Innovation Fellowship (8 winning teams out of 109)
- Best paper award and travel award of 10th International Nanotechnology Conference on Communication and Cooperation (INC 10)

Chapter 1

Introduction

In the last few decades, the discoveries of novel material often propelled the progress in condensed-matter physics. In this regard, the recently discovered time-reversal-invariant topological insulator (TI), a novel state of quantum matter, has led to the flourishing of unique physics along with promises for innovative electronic and spintronic applications.[1-3]

Topological insulator is a class of quantum material featuring with an energy gap in its bulk band structure and unique Dirac-like metallic states on the surface.[3-7] It behaves as an ordinary insulator in its bulk, *i.e*., the Fermi level falling between the conduction and valence bands. However, the surface (or edge in two dimensions) of a topological insulator has gapless states that are protected by time-reversal symmetry (TRS).[6, 8, 9] Consequent to the TRS, the spin of the Dirac-like surface states (SS) is tightly locked to the momentum, resulting in a spin-polarized current at the surface of the TI which is immune to direct back-scattering.[1, 3, 6-9] Furthermore, these topological properties are robust against non-magnetic external perturbations. Such properties make TIs perfect candidates for low dissipation spintronic devices.

In order to appreciate the relevance and the importance of TIs in condensed matter physics, it is necessary to study the historical background. In this chapter, we will discuss several important concepts that preceded the discovery of TIs.

1.1. Integer Quantum Hall Effect

In 1980, German physicist von Klitzing, working at the high magnetic field laboratory with high mobility 2D silicon-based field effect transistors developed by Pepper and Dorda, made the unexpected discovery that the Hall conductivity was precisely quantized (no need of any corrections), as a total surprise to the physics community[10]. For this significant finding of integer quantum Hall effect (IQHE), von Klitzing was awarded the 1985 Nobel Prize in Physics.

Quantum Hall effect (QHE) usually occurs in two-dimensional electron gas systems subjected to low temperature and high magnetic fields, resulting in the formation of conducting one-dimensional channels that develop at the edges of the sample. In QHE, an energy gap results from the quantization of the closed circular orbits that electrons follow in a magnetic field. The energy levels, also known as Landau level (LL), arising from the quantization of the orbits take on discrete values:

$$E_n = \hbar\omega_c(\mathrm{N}+\frac{1}{2}) \tag{1-1}$$

where $\omega_c=eB/m$ is the cyclotron frequency, and N is a non-negative integer.[11] The electrons inside the material (bulk electrons) become localized (because they trace only small and closed orbits) and the bulk is thus inert like an insulator. However, at the boundary of the material a different type of motion occurs, which allows carrier to flow in one-dimensional edge states, known as chiral edge state.[12] Each edge channel in which the carrier flows only in one direction and avoids dissipation, gives rise to a quantized Hall conductance. The

number of edge channels in the sample is directly related to the value of the quantum Hall conductance [10, 12]

$$\sigma_{xy} = \nu \frac{e^2}{h} \tag{1-2}$$

where e is the elementary charge and h is Planck's constant. The factor ν is known as the "filling factor", and can take on either integer (ν = 1, 2, 3, …)[12] and fractional (ν = 1/3, 2/5, 3/7, 2/3, 3/5, 1/5, 2/9, 3/13, 5/2, 12/5 ...) values.[13] The QHE was previously believed to only be observable at temperatures close to absolute zero. However, in 2007, Novoselov *et al.* surprisingly found that QHE can be observed in graphene as shown in Figure 1-1, a two-dimensional ultra high mobility single sheet of graphite, even at room temperature! [14]

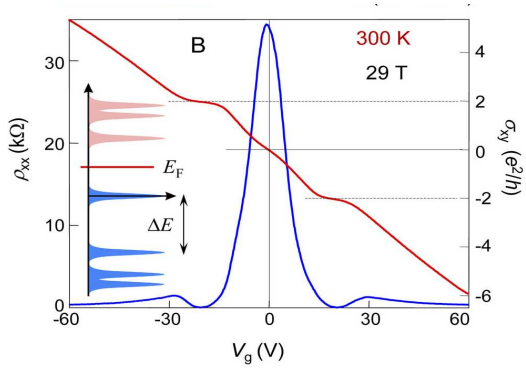

Figure 1-1. σ_{xy} (red) and ρ_{xx} (blue) as a function of gate voltages (V_g) in a magnetic field of 29 T. (Inset) The LL quantization for Dirac fermions. Adapted from Ref. 14.

It is worth to mention that the QHE phenomenon was recognized as a matter of topology by Thouless, Kohmoto, Nightingale, and den Nijs (TKNN) in 1982.[15] Consider a 2D band structure consists of a mapping from the Brillouin zone to a Hilbert space, band structures with finite energy gap separating the occupied bands and the empty bands can be

classified topologically by considering the equivalence classes in Hibert space that can be continuously deformed into one another without closing the energy gap. The TKNN invariants are also known as first Chern numbers n in mathematics, which are closely related with Berry's phase, to be explained in Section 1.2.1.

$$n=\frac{1}{2\pi}\int d^2kF \tag{1-3}$$

where the Berry's curvature $F = \nabla \times A$, and Berry's connection $A_n(\mathrm{R}) = -\mathrm{i}\left\langle n(\mathrm{R})\middle|\nabla_R n(\mathrm{R})\right\rangle$

Notice that n in Eq. (1-3) is exactly the same as υ in Eq. (1-2). The concept of topological invariance or first Chern number n can be used to classify different geometrical objects into broad classes. For instance, a sphere is topologically equivalent to an ellipsoid, since these two surfaces can be smoothly deformed into each other without creating any holes.[1] Similarly, a coffee cup is topologically equivalent to a donut, since they can be transformed from each other.[1] 2D surface can be classified by their genus number g, which counts the number of holes. So the sphere or ellipsoid has g=0, while the coffee cup has g=1.

1.2. Quantum Spin Hall Effect

The QH states belong to a topological class which breaks time-reversal symmetry by the presence of a magnetic field. In recent years, a new topological class of matter quantum spin Hall state, which preserves time-reversal symmetry, has been theoretically predicted and experimentally observed.[2, 3, 16-18] The QSH state is the cousin of the integer QH state[8,

[19], but unlike the latter, it does not require the application of a large magnetic field. The QSH insulators are essentially two copies of the quantum Hall system, and the two edge states form a time-reversed pair to recover the overall TRS. Moreover, the QSH edge states exhibit the important "spin filtered" property that the up spins propagate in one direction, while the down spins propagate in the opposite direction as shown in Figure 1-2.

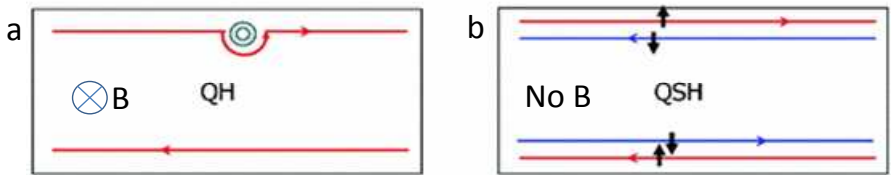

Figure 1-2. Analogy between QH and QSH effects. (a) The QH edge conduction in the presence of perpendicular magnetic field. The upper edge supports only a forward mover and the lower edge supports only a backward mover. The states are robust and go around an impurity without scattering. (b) The helical edge conduction in QSHE without any external magnetic field. The upper edge supports a forward mover with spin up and a backward mover with spin down, and conversely for the lower edge. Modified from Ref. 17.

1.2.1. Helical Edge State and Berry's Phase

In the QSHE, the TRS prevents the helical edge states from backscattering. The absence of backscattering relies on the destructive interference between all possible backscattering paths taken by the edge electrons.[1] And this brings to another important

concept for topological insulators: Berry's phase. Therefore, before further introducing QSHE, it is worth to discuss its definition and the relation with TI here. The detailed derivation can be found in ref. [20].

Imagine a quantum system whose Hamiltonian *H* describes the effects of an unchanged environment and let the system in a stationary state. Let the Hamiltonian *H* change by varying parameter *R*. Then the system between times *t*=0 to *t*=T can be pictured as transport round a closed loop *R*(t) in parameter space, with Hamiltonian *H*(*R*(t)) and such that *R*(0)=*R*(T). The closed loop is denoted as C, short for circuit. The Schrodinger equation for this system is

$$H\left[R(\mathrm{t})\right]\left|\psi(\mathrm{t})\right\rangle = E_n[\mathrm{R(t)}]\left|\psi(\mathrm{t})\right\rangle \tag{1-4}$$

Suppose that *R* changes adiabatically from *t*=0 value R_0. Also, assume the natural basis consists of the eigenstate $\left|n(R)\right\rangle$. The time evolution of the state follows

$$H\left[R(\mathrm{t})\right]\left|n(\mathrm{R})\right\rangle = i\hbar\frac{\partial}{\partial t}\left|n(\mathrm{R})\right\rangle \tag{1-5}$$

Thus $\left|\psi(\mathrm{t})\right\rangle$ can be written as

$$\left|\psi(\mathrm{t})\right\rangle = \exp\left\{\frac{-i}{\hbar}\int_0^t dt' E_n(\mathrm{R(t')})\right\}\exp(\mathrm{i}\,\gamma_n(\mathrm{t}))\left|n(\mathrm{R(t)})\right\rangle \tag{1-6}$$

The first exponential term represents the dynamic phase factor. The second exponential presents the nontrivial effect of the quantum-mechanical phase accumulated during the time evolution. The important point here is that its phase γ_n is non-integrable, and γ_n cannot be written as a function of *R*. And γ_n is not a single number under the continuation around the circuit, *i.e.*, $\gamma_n(0) \neq \gamma_n(\mathrm{T})$.

Substitution of (3) into (1) leads to $\dot{\gamma}_n(\mathrm{t}) = \mathrm{i}\left\langle n(\mathrm{R}(\mathrm{t}))\middle|\nabla_R n(\mathrm{R}(\mathrm{t}))\right\rangle \cdot \dot{\mathrm{R}}(\mathrm{t})$ (1-7)

The total phase change of $|\psi\rangle$ around the C is given by

$$|\psi(\mathrm{T})\rangle = \exp(\mathrm{i}\,\gamma_n(\mathrm{C}))\exp\left\{\frac{-i}{\hbar}\int_0^T dtE_n(\mathrm{R}(\mathrm{t}))\right\}|\psi(0)\rangle \quad (1\text{-}8)$$

where the geometrical phase change is

$$\gamma_n(\mathrm{C}) = i\oint_C \left\langle n(\mathrm{R})\middle|\nabla_R n(\mathrm{R})\right\rangle \cdot dR = -\oint_C dR \cdot An(\mathrm{R}) = -\int_S \mathrm{dS}\cdot B_n \quad (1\text{-}9)$$

The last equality comes from the Stokes' theorem. Here we define the Berry connection as

$$A_n(\mathrm{R}) = -\mathrm{i}\left\langle n(\mathrm{R})\middle|\nabla_R n(\mathrm{R})\right\rangle \quad (1\text{-}10)$$

Its curl is the Berry curvature $B_n(\mathrm{R}) = \nabla_R \times A_n(\mathrm{R})$ (1-11)

From Eqs. (1-8) and (1-9), one can see that the Berry's phase means the accumulated phase factor of a quantum-mechanical system after it completes a closed loop in a parameter space.

At the QSH helical edge, a forward-moving electron with spin up can make either a clockwise or a counterclockwise turn around the impurity as shown in Figure 1-3. Since only spin-down electrons can propagate backward, the electron spin has to adiabatically rotate by an angle either π or $-\pi$ into the opposite direction. Consequently, the two paths differ by a full $\pi - (-\pi) = 2\pi$ rotation of the electron spin. However, the wave function of a spin$-1/2$ particle picks up a negative sign under a full 2π rotation. In other words, in the spin space (spinwave function manifold), the quantum phase or Berry phase through a close loop accumulates π. Therefore, two backscattering paths interfere destructively, leading to perfect transmission. The π Berry's phase of topological insulator protects these surface states against backscattering from disorder and impurities, and leads to weak anti-localization

effect.[21]

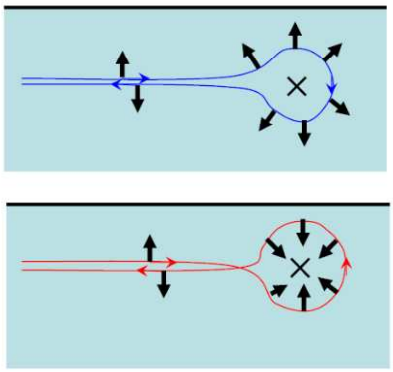

Figure 1-3. Two possible paths on a QSH edge when scattered by a nonmagnetic impurity. The electron spin rotates by 180° clockwise along the blue curve, and counterclockwise along the red curve. A geometrical phase factor in the spin wave function manifold associated with this rotation of the spin leads to destructive interference between the two paths. In other words, electron backscattering on the QSH edge is suppressed in a way similar to how the reflection of photons is suppressed by an antireflective coating. Adapted from Ref. 17.

1.2.2. QSHE in Two-Dimensional Topological Insulator

The idea about Quantum Hall effect without Landau Levels was originally proposed by Haldane in 1988 in a 2D graphite (graphene) system.[22] In 2005, Kane and Mele adapted the earlier proposal by adding spin-orbital coupling term in which a finite SOC leads to an opening of a gap at the Dirac point of graphene.[8, 23] Therefore, a time-reversed pair of

spin-polarized edge states show up with spin aligned and locked to its momentum due to the SOC, which is often called helical spin-polarized states. However, the QSH effect was not experimentally realized in graphene since the SOC in graphene is too weak.

A subsequent theoretical effort was soon made by Bernevig, Hughes, and Zhang, who predicted that a CdTe/HgTe/CdTe quantum well, which was studied as infrared photodiode in many earlier work, [24] [25] gives rise to the QSH effect.[18] The barrier material (CdTe) has a normal band structure, with the *s*-type Γ_6 band lying above the *p*-type Γ_8 band, while the well material (HgTe) having an inverted band progression where the Γ_6 band lies below the Γ_8 band. In both of these materials, the gap is smallest near the Γ point in the Brillouin zone. Figure 1-4 presents the quantum phase transition at a critical thickness d_c of the quantum well. For thickness $d < d_c$ (*i.e.*, for a thin HgTe layer), the quantum well is in the "normal" regime, where the CdTe is predominant and hence the band energies at the Γ point satisfy $E(\Gamma_6) > E(\Gamma_8)$. For $d > d_c$ (*i.e.*, for a thick HgTe layer), the well is in the inverted regime, where HgTe dominates and $E(\Gamma_6) < E(\Gamma_8)$. As the thickness of the well varies, the E_1 and H_1 bands therefore cross at certain d_c, and the energy gap at $d=d_c$ vanishes.

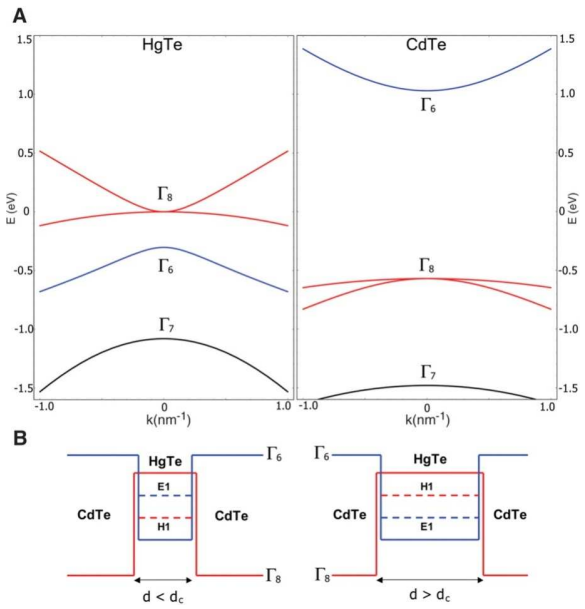

Figure 1-4. (a) Bulk energy bands of HgTe and CdTe near the Γ point. (b) The CdTe/HgTe/CdTe quantum well in the normal regime $E_1 > H_1$ with $d < d_c$, and in the inverted regime $H_1 > E_1$ with $d > d_c$. Adapted from Ref. 18. The bandstructure of HgCdTe can also been found in other earlier work about infrared photodiode/photodetector .[24 25]

In 2007, König *et al.* first provided the experimental evidence of QSHE. HgTe/(Hg,Cd)Te QW structures were fabricated with low density and high mobility in which the carrier conduction from *n*-type to *p*-type can be tuned, through an external gate voltage, passing through an insulating regime. For thin quantum wells with well width $d <$ 6.3 nm (sample I), has a large resistance in the gap at low temperature as shown in Figure 1-5.[16] Samples II–IV are thicker wells ($d >$ 6.3 nm) in the inverted regime. Samples III and IV exhibit a conductance $2e^2/h$ associated with the top and bottom edges, with same length L=1 μm but different widths w=0.5 and 1μm, indicating that transport is indeed at the edge.

Sample II (L=20 μm) showed finite temperature scattering effects. These experiments convincingly demonstrate the existence of the edge states of the quantum spin Hall insulator.[3] Note that the $h/2e^2$ plateau is not completely robust (some fluctuations are seen in the figure). This is different from quantum anomalous Hall effect, in which a precise quantization has been observed, to be discussed in section 1.3 and section 4.1.

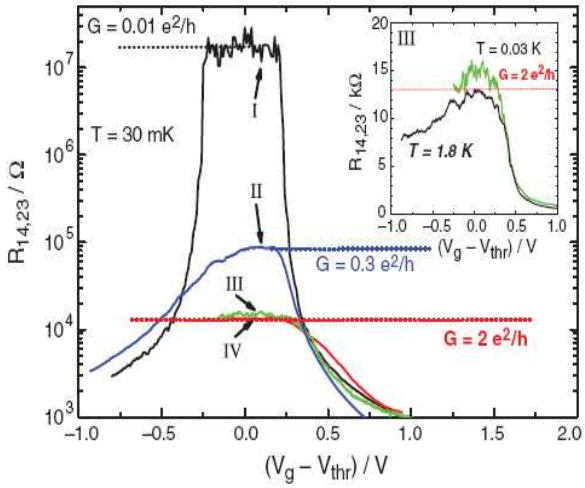

Figure 1-5. The longitudinal four terminal resistance, $R_{14,23}$, of various normal (d = 5.5 nm) (I) and inverted (d = 7.3 nm) (II, III, and IV) CdTe/HgTe/CdTe quantum well structures as a function of the gate voltage measured for B = 0 T at T = 30 mK. The device sizes are (20.0×13.3) μm^2 for devices I and II, (1.0×1.0) μm^2 for device III, and (1.0×0.5) μm^2 for device IV. The inset shows $R_{14,23}$ as a function of V_g of two samples from the same wafer, having the same device size (III) at 30 mK (green) and 1.8 K (black) on a linear scale. Note that the $h/2e^2$ plateau is not completely robust (some fluctuations are seen in the figure). Adapted from Ref. 16.

Moreover, the residual conductance $2e^2/h$ can be destroyed by a small external magnetic field perpendicular to the 2DEG plane.[16] Figure 1-6 shows that the magnetoresistance is strongly anisotropic. A very sharp conductance peak is observed for perpendicular field, with the full width at half maximum (FWHM) $B_{\perp FWHM} \approx 28$ mT. The peak broadens strongly when the magnetic field is tilted into the QW plane. For fully in-plane fields, the QSH conductance can be observed over a much wider magnetic field range ($B_{||FWHM} \approx 0.7$ T).[16] Due to the magnetic field, the time-reversal symmetry is broken and thus turns on a gap between the two helical edge states.

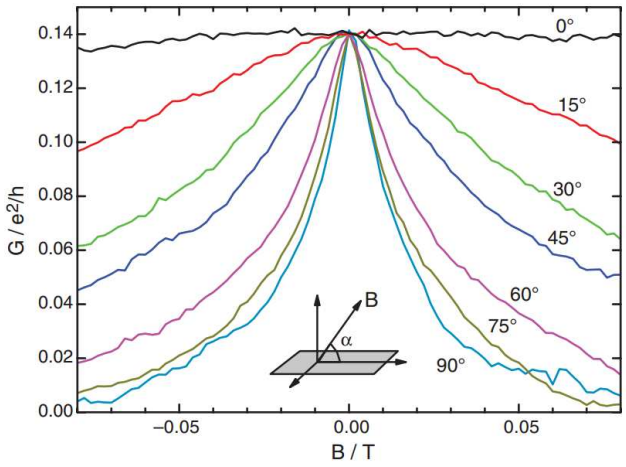

Figure 1-6. Four-terminal magnetoconductance $G_{14,23}$, in the QSH regime as a function of tilt angle between the plane of the 2DEG and magnetic field (inset) for a d = 7.3 nm HgTe/(Hg,Cd)Te QW structure measured in a vector field cryostat at 1.4 K. The residual conductance $2e^2/h$ can be destroyed by a small external magnetic field. Adapted from Ref. 16.

1.2.3. QSHE in Other Material Systems

The search for large-gap quantum spin Hall (QSH) insulators and effective approaches to tune QSH states never stops for both fundamental and practical interests. In 2013, Du group experimentally realized the QSHE in an inverted electron-hole bilayer engineered from indium arsenide-gallium antimonide (InAs/GaSb) semiconductors which retains robust helical edges up to 4 K and under a strong magnetic field.[26] Wide conductance plateaus of $2e^2/h$ value were observed by tuning front gate voltage; the plateaus persist up to 12 T applied in-plane magnetic field without evidence for transition to a trivial insulator.[26] Remarkably, the temperature used to observe QSHE in HgTe quantum well was restricted to 30 mK; however, in InAs/GaSb system, the QSH persists up to 4 K, two orders of magnitude higher than the former one.

Several months later, a theoretical work proposed by Zhang group indicating that QSHE can be achieved in another interesting 2D system.[27] Based on their first-principles calculations, it is found that the two-dimensional tin films "stanene" are QSH insulators with sizable bulk gaps of 0.3 eV. The mechanism for the QSHE in this system is the band inversion at the Γ point, similar to the case of a HgTe quantum well. [27]

1.3. Quantum Anomalous Hall Effect

Quantum anomalous Hall effect (QAHE) is a quantized version of anomalous Hall effect, which also belongs to the topological family. Since QAHE presents the realization of the QHE in the zero magnetic field, therefore the dissipationless quantum transport is expected in QAH system.[28]

To realize QAH state, one needs to break time-reversal symmetry with ferromagnetic 2D TI films. Moreover, in 2D TI, the ferromagnetically induced exchange splitting needs to be large enough to drive one set of spin subband back to the topologically trivial phase, leaving only one spin channel remaining topological protected (See Figure 1-7).[29, 30] On the boundary of a QSH insulator there are counter propagating edge states carrying opposite spin. When the spin splitting term increases, the spin-down edge states penetrate deeper into the bulk due to the decreasing gap and eventually disappear, leaving only the spin-up state bound more strongly to the edge.[1, 30] Therefore, the helical edge state in QSHE evolves into chiral edge states exhibiting QAHE. The QAHE was first predicted in a Mn doped HgTe quantum well system as long as the Mn spins are polarized.[30] However, experimentally, an external magnetic field was still required to align the Mn moment in order to observe QAHE.[31]

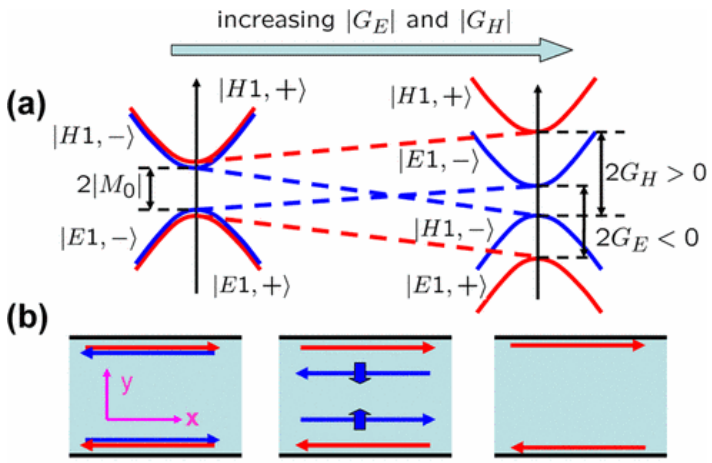

Figure 1-7. Evolution of band structure and edge states upon increasing the spin splitting. For (a) $G_E < 0$ and $G_H > 0$, the spin-down states $|E1,-\rangle$ and $|H1,-\rangle$ touch each other and then enter the normal regime. (b) The behavior of the edge states during the level crossing in the case of (a). Adapted from Ref. 30.

In 3D TI doped with 3d transition metal elements, due to the van Vleck mechanism such as Fe, Mn, Cr, a ferromagnetism can be developed with Curie temperature up to ~35 K. A detailed review of 3D TI will be given in the session 1.4. For those very thin 3D TI systems, it will induce the QAH effect if the magnetic exchange field is perpendicular to the plane and overcomes the semiconductor gap.[32] Through an optimization of sample growth parameters and measurements at ultra-low temperature, the QAHE was first experimentally observed in a 5 QL $Cr_{0.15}(Bi_{0.1}Sb_{0.9})_{1.85}Te_3$ film grown on $SrTiO_3$ (111) substrates by Xue group in 2013.[32] Figure 1-8 (a) and (c) shows the magnetic field dependence of ρ_{yx} and ρ_{xx}, respectively, at different V_gs measured at T = 30 mK. The most important observation is that the zero field

Hall resistance exhibits a distinct plateau with the quantized value h/e^2, which is centered around the gate voltage V_g = –1.5 V. Sheet conductance are transformed from $\rho_{yx}(0)$ and $\rho_{xx}(0)$ through the relations $\sigma_{xy} = \rho_{yx}/(\rho_{yx}^2 + \rho_{xx}^2)$ and $\sigma_{xx} = \rho_{xx}/(\rho_{yx}^2 + \rho_{xx}^2)$ and plot them in Figure 1-8 (d). Around V_g^0 , $\sigma_{xy}(0)$ has a notable plateau at 0.987 e^2/h, whereas $\sigma_{xx}(0)$ has a dip down to 0.096 e^2/h, similar to the behavior of the corresponding resistances.

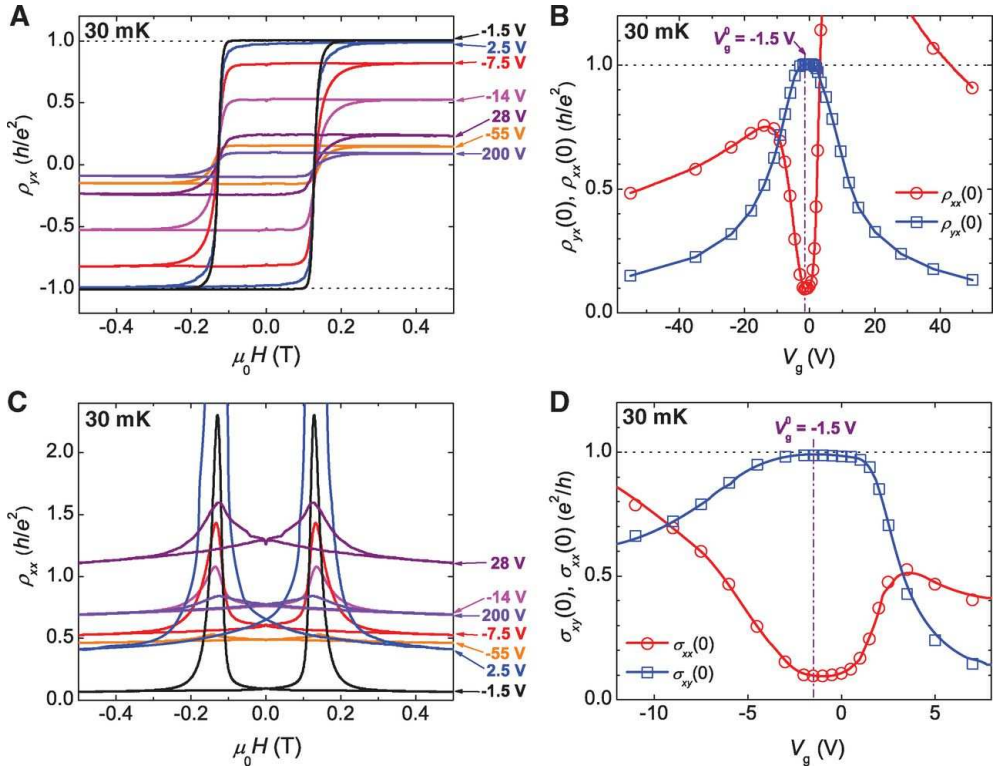

Figure 1-8. The QAH effect measured at 30 mK. (a) Magnetic field dependence of ρ_{yx} at different V_gs. (b) Dependence of $\rho_{yx}(0)$ (hollow blue squares) and $\rho_{xx}(0)$ (hollow red circles) on V_g. (c) Magnetic field dependence of ρ_{xx} at different V_gs. (d) Dependence of $\sigma_{xy}(0)$ (hollow blue squares) and $\sigma_{xx}(0)$ (hollow red circles) on V_g. The vertical purple dashed-dotted lines in (c) and (d) indicate the V_g for V_g^0. Adapted from Ref. 32.

Soon after the first experimental report of QAH, our group also successfully observed QAHE in our MBE grown $(Cr_{0.12}Bi_{0.26}Sb_{0.62})_2Te_3$ sample with a thickness of 10 QL.[33] Due to the chiral nature of the edge modes, the quantization of the Hall conductance (e^2/h) persists in the device with millimeter-scale sizes. Figure 1-9 shows the magneto-transport results of the 10 QL $(Cr_{0.12}Bi_{0.26}Sb_{0.62})_2Te_3$ film. By applying the Landauer-Büttiker formalism $I_i = \frac{e^2}{h}\sum_j (T_{ji}V_i - T_{ij}V_j)$ [34], we can quantitatively understand the chiral edge transport in our sample. When the film is magnetized along $+z$ direction (left panel of Figure 1-9(a)), the non-zero transmission matrix elements for the QAHE state are $T_{61} = T_{56} = T_{45} = 1$ [35, 36], and the corresponding voltage distributions are given by $V_6 = V_5 = V_1 = (h/e^2)I$ and $V_2 = V_3 = V_4 = 0$. On the other hand, when the magnetization reverses its direction (right panel of Figure 1-9(a)), the edge current flows through the 2nd and 3rd contacts, thus making $V_2 = V_3 = V_1 = (h/e^2)I$ and $V_5 = V_6 = V_4 = 0$. Consequently, $R_{xy} = R_{14,62} = (V_6 - V_2) / I$ is positive for the $M_Z > 0$ case, and change to negative sign if $M_Z < 0$. [33]

When the sample temperature falls below 85 mK, the 10 QL $(Cr_{0.12}Bi_{0.26}Sb_{0.62})_2Te_3$ film reaches the QAHE regime. In Figure 1-9 (b) and (c), it is observed that when the film is magnetized, the Hall resistance R_{xy} reaches the quantized value of h/e^2 (25.8 kΩ) at $B = 0$ T, while the longitudinal resistance R_{xx} is nearly vanished. Different from previous work[32], a non-zero longitudinal resistance is detected in our thick 10 QL sample and is found to be insensitive to external magnetic field, indicating the possible presence of additional non-chiral side surface propagation modes. [33]

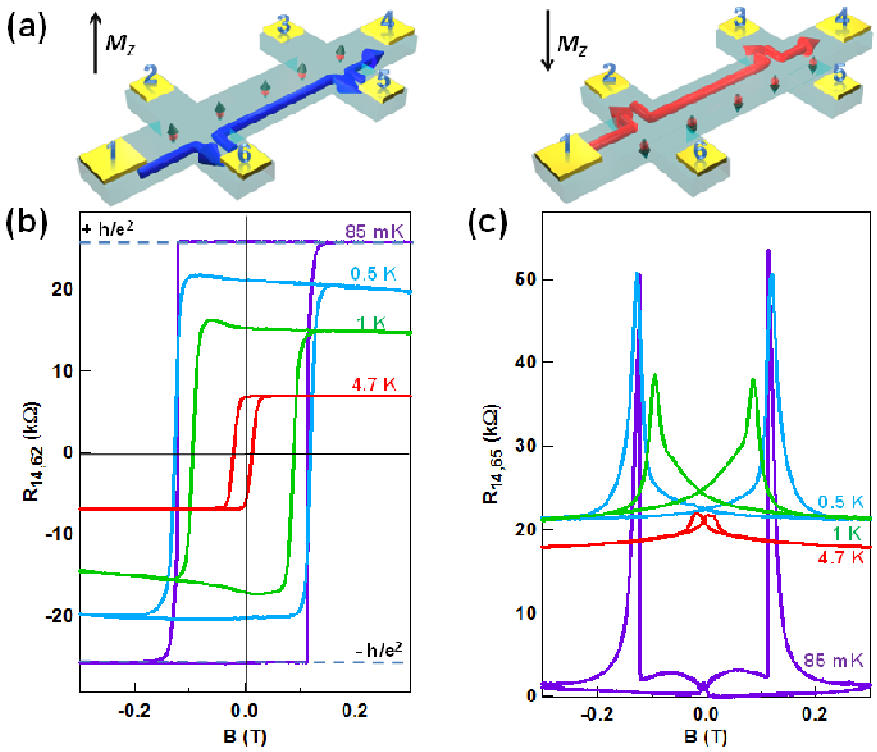

Figure 1-9. QAHE in the 10 QL $(Cr_{0.12}Bi_{0.26}Sb_{0.62})_2Te_3$ thin film. (a) Schematics of the chiral edge conduction in the QAHE regime. The current flows from the 1st contact to the 4th contact, and the magnetization of the Cr-doped TI film is along the z-direction. (b) Temperature-dependent hysteresis R_{xy} curves. When the sample temperature is below 85 mK, the sample reaches the QAHE regime, where R_{xy} becomes the quantized value of h/e^2 and insensitive to applied magnetic field. (c) Temperature-dependent magneto-resistance R_{xx} curves. As the sample approaches the QAHE state, R_{xx} dramatically decreases and nearly vanishes when the sample temperature is below 85 mK. (This also appears in one of my publications Ref. 33)

Almost at the same time, Tokura group also reported their observation of QAHE with devices based on cleaved single crystals of Mn-doped $Bi_2Te_{3-y}Se_y$. With the application of both solid-dielectric and ionic-liquid gating, the transport response of the surface states within the bulk bandgap in the presence of magnetic ions were revealed.[37]

1.4. Three-Dimensional Topological Insulators

In 2008, the first three dimensional TI bulk material $Bi_{1-x}Sb_x$, a semiconducting alloy, was experimentally identified by angle resolved photoemission spectroscopy (ARPES) experiment by Hasan group[38], following the specific prediction by Fu and Kane.[39]

Bismuth antimony alloys have long been studied for their thermoelectric properties. Pure bismuth is a semimetal with strong spin-orbit interactions[3]. As schematically shown in Figure 1-10 (a), the conduction and valence bands of pure bismuth overlap. The valence and conduction bands at the L point, derived from antisymmetric L_a and symmetric L_s orbitals, have a small energy gap Δ.[38] However, if antimony is substituted into bismuth, it changes the critical energies of the band structure (See Figure 1-10 (b)). At an Sb concentration of $x \approx 0.04$, the gap Δ between L_a and L_s closes and a truly massless 3D Dirac point is realized.[38] As further increase x, this gap re-opens with an inverted ordering. For $x > 0.07$ the top of the valence band at T moves below the bottom of the conduction band at L, therefore the material becomes an insulator. Once the band at T drops below the valence band at L (at x

> 0.09), the system is a direct-gap insulator with a Dirac-like bulk band. As *x* is increased further, the conduction and valence bands remain separated, and for *x* > 0.22, the valence band rises above the conduction band, recovering the semimetallic state. [3]

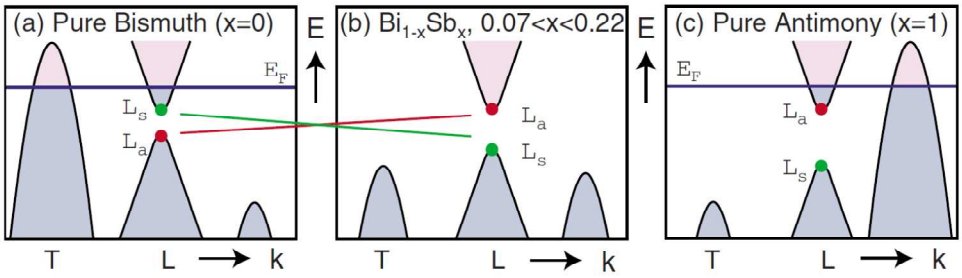

Figure 1-10. Schematic representation of the band structure of $Bi_{1-x}Sb_x$, which evolves from semimetallic behavior for x < 0.07 (a) to semiconducting behavior for 0.07 < *x* < 0.22 (b) and back to semimetallic behavior for *x* > 022 (c). The conduction and valence bands $L_{s,a}$ invert at *x* ~ 0.04. Adapted from Ref. 3.

1.4.1. Angle Resolved Photoemission Spectroscopy (ARPES) Measurement

It is well known that ARPES is an excellent tool for probing surface states of 3D TIs.[38, 40-42] ARPES uses a photon to eject an electron from a sample, and then determines the surface or bulk electronic structure by analyzing the momentum of the emitted electron. High-resolution ARPES performed with modulated photon energy can clearly isolate the surface states from that of the bulk 3D band structure, since surface states do not disperse along a direction perpendicular to the surface while the bulk states do.[3]

Figure 1-11 displays the complete ARPES spectra of $Bi_{0.9}Sb_{0.1}$ which can be interpreted as a map of the energy of the occupied electronic states as a function of momentum along a path connecting $\bar{\Gamma}$ and $\bar{M}$ in the projected surface Brillouin zone. The shaded white area in Figure 1-11 indicates the projection of the bulk bands based on ARPES data, as well as a rigid shift of the tight binding bands to sketch the unoccupied bands above the Fermi level. The yellow circles denote the Fermi crossings of the surface state, with the band near $-k_x \approx 0.5\,\text{Å}^{-1}$ counted twice owing to double degeneracy. Moreover, it is noted that there are five crossings between $\bar{\Gamma}$ and $\bar{M}$ which demonstrates that these surface states are topologically non-trivial. When the number of surface state crossing is even, the surface states are topologically trivial since the weak disorder or correlation can remove pairs of such crossing by pushing the surface states above or below the E_F. On the other hand, when the numbers of crossing is odd, at least one surface state must remain gapless, which makes it topologically non-trivial. The number of surface state crossings in a material is related to the topological Z_2 invariant.[38]

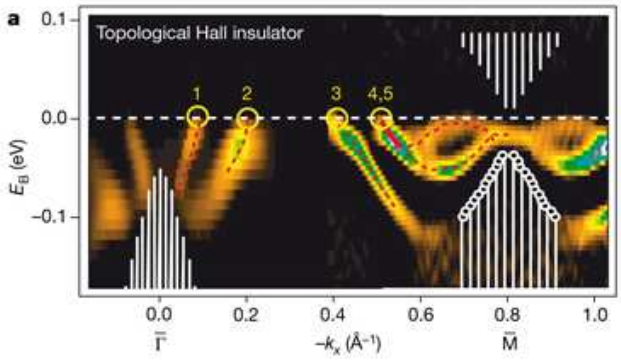

Figure 1-11. Topological surface states in $Bi_{1-x}Sb_x$. ARPES data on the (111) surface of $Bi_{0.9}Sb_{0.1}$ which probes the occupied surface states as a function of momentum on the line connecting the T invariant points $\bar{\Gamma}$ and $\bar{M}$ in the surface Brillouin zone. Adapted from Ref. 38.

Although $Bi_{1-x}Sb_x$ is the first discovered 3D TI material, the surface structure of $Bi_{1-x}Sb_x$ is rather complicated and the band gap is small, which motivated a search for topological insulators with a larger band gap and simpler surface spectrum. Soon after, Zhang *et al.* performed first-principles electronic structure calculation and came up with a concrete prediction that Bi_2Se_3, Bi_2Te_3, and Sb_2Te_3 are 3D TIs, but Sb_2Se_3 is not.[7] Experimentally, Bi_2Se_3[4, 43-45], Bi_2Te_3[40, 44, 46, 47] and Sb_2Te_3[47] were soon confirmed by detailed and systematic surface investigations, such as ARPES and STM.

1.4.2. Bi_2Se_3 Crystal Structure and Band Structure

Among various TI materials found till now, Bi_2Se_3 has the simplest Dirac cone surface spectrum and the largest band gap (0.3 eV), which is larger than the energy scale of room temperature.[7] This indicates that in its high-purity form Bi_2Se_3 can exhibit topological insulator behavior at room temperature and greatly increases the potential for future spintronics applications; nevertheless, till now, the defects as well as the undesired bulk

component in this material still prevents it from practical applications. In 2009, Xia *et al.*[46] used ARPES and first-principles calculations to study the surface band structure of Bi_2Se_3 and observe the characteristic signature of TI in the form of a single Dirac cone, as shown in Figure 1-12, in which (a) and (b) are measurement along the $\bar{\Gamma}-\bar{M}$ and $\bar{\Gamma}-\bar{K}$ momentum-space cuts, respectively. [46]

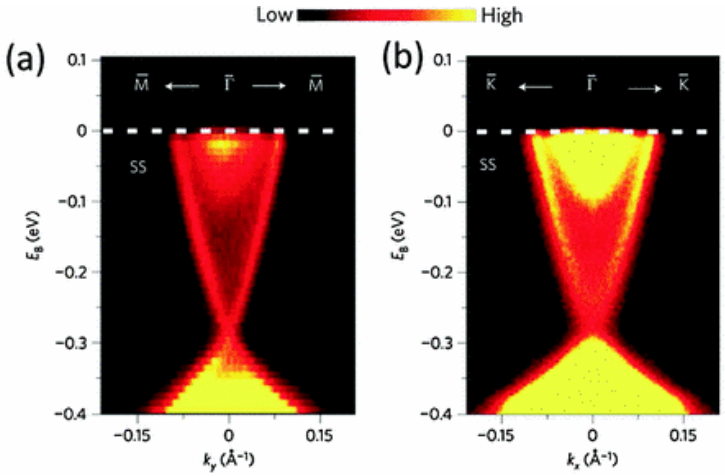

Figure 1-12. (a),(b) High-resolution ARPES measurements of surface electronic band dispersion on Bi_2Se_3 (111). Electron dispersion data measured with an incident photon energy of 22 eV near the Γ-point along the $\bar{\Gamma}-\bar{M}$ and $\bar{\Gamma}-\bar{K}$ momentum-space cuts. Adapted from Ref. 46.

The Bi_2Se_3 has rhombohedral crystal structure with five atoms per unit cell. The crystal structure of Bi_2Se_3 is shown in Figure 1-13 (a), and consists of layered structure where individual layers form a triangular lattice. The important symmetry axes are a trigonal axis (three-fold rotation symmetry) defined as the z axis, a binary axis (two-fold rotation

symmetry) defined as the x axis and a bisectrix axis (in the reflection plane) defined as the y axis.[7] Bi_2Se_3 consists of five-atom layers stacked along the z direction, known as quintuple layers (QLs). Each QL is about 1 nm thick and it consists of five atoms per unit cell with two equivalent Se atoms denoted by Se1 and Se1′ in Figure 1-13 (b), two equivalent Bi atoms denoted by Bi1 and Bi1′ in Figure 1-13 (b), and a third Se atom denoted by Se2 in Figure 1-13 (b). The covalent bonding between two atomic layers within a quintuple layer is strong, while that between quintuple layers is much weaker with van der Waals force.

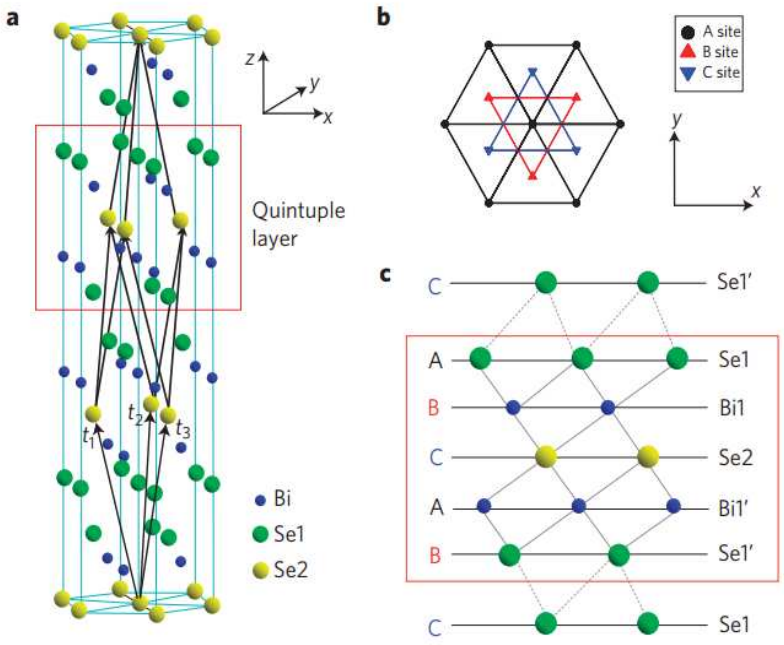

Figure 1-13. (a) Crystal structure of Bi_2Se_3 with three primitive lattice vectors denoted as $t_{1,2,3}$. A quintuple layer with Se1–Bi1–Se2–Bi1'–Se1' is indicated by the red square. (b) Top view along the *z*-direction. The triangle lattice in one quintuple layer has three different positions, denoted as A, B and C. (c) Side view of the quintuple layer structure. Along the *z*-direction, the stacking order of Se and Bi atomic layers is …

–C(Se1')–A(Se1)–B(Bi1)–C(Se2)–A(Bi1')–B(Se1')–C(Se1)–…. The Se1 (Bi1) layer can be related to the Se1' (Bi1') layer by an inversion operation in which the Se2 atoms have the role of inversion centers. Adapted from Ref. 7.

To better understand the band structure of Bi_2Se_3, the evolution from the atomic $p_{x,y,z}$ orbitals of Bi and Se into the conduction and valence bands of Bi_2Se_3 is schematically shown in Figure1-14 . Since the states near the Fermi level are primarily from *p*-orbitals, the *s*-orbitals are neglected and we start from the atomic *p*-orbitals of Bi ($6s^2 6p^3$) and Se ($4s^2 4p^4$). [7] In stage (I), chemical bonding between Bi and Se atoms within a QL is considered, which corresponds to the largest energy scale in this problem.[7] First, the orbitals in a single unit cell are recombined according to their parity, which leads to three states from each Se *p*-orbital and two states from each Bi *p*-orbital as illustrated in stage (I).[7] The formation of chemical bonds hybridizes the states on the Bi and Se atoms, and pushes down all the Se states and lifts all the Bi states.[7] In stage (I), these five hybridized states are labeled as $\left|P1^{\pm}_{x,y,z}\right\rangle$, $\left|P2^{\pm}_{x,y,z}\right\rangle$ and $\left|P0^{-}_{x,y,z}\right\rangle$ where the superscripts +, − represent the parity of the corresponding states. In stage (II), the effect of crystal field splitting between different *p*-orbitals is added on. Based on the point group symmetry, the p_z orbital is split from the p_x and p_y orbitals while the latter two remain degenerate.[7] After this splitting, the energy levels closest to the Fermi energy turn out to be the p_z levels $\left|P1^{+}_{z}\right\rangle$ and $\left|P2^{-}_{z}\right\rangle$.[1, 7] In stage (III), the effect of SOC is added on. The atomic SOC Hamiltonian is given by $H_{SO} = \lambda L \cdot S$, with *L*, *S* the orbital and spin angular

momentum, respectively, and λ the strength of SOC. The SOC Hamiltonian mixes spin and orbital angular momenta while preserving the total angular momentum. As a result, the energy of the $\left|P1_z^+,\uparrow(\downarrow)\right\rangle$ state is pushed down by the effect of SOC, and the energy of the $\left|P2_z^-,\uparrow(\downarrow)\right\rangle$ state is pushed up. If SOC is larger than a critical value $\lambda > \lambda_c$, the order of these two energy levels is reversed.[1] Since these $\left|P1_z^+,\uparrow(\downarrow)\right\rangle$ and $\left|P2_z^-,\uparrow(\downarrow)\right\rangle$ levels have opposite parity, the inversion between them drives the system into a topological insulator phase, similar to the case of HgTe QWs [19].

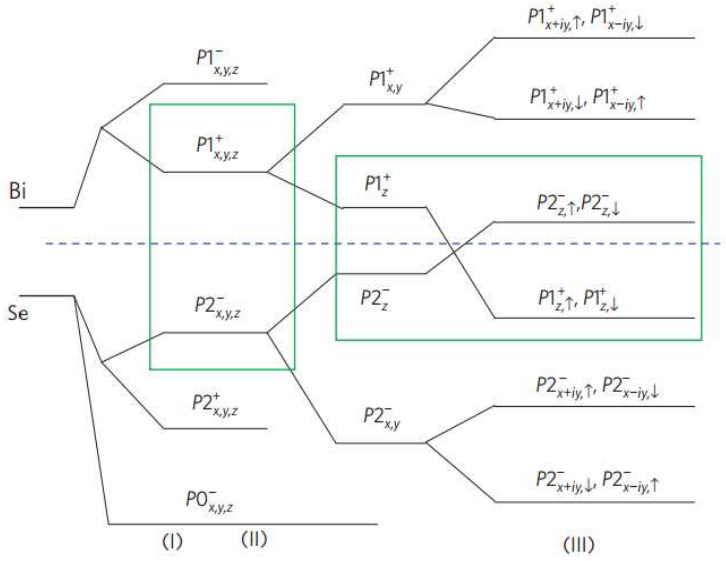

Figure 1-14. (a) Schematic picture of the evolution from the atomic $p_{x,y,z}$ orbitals of Bi and Se into the conduction and valence bands of Bi_2Se_3 at the Γ point. The three different stages (I), (II) and (III) represent the effect of adding on chemical bonding, crystal field splitting, and SOCconsecutively. The blue dashed line represents the Fermi energy. Adapted from Ref. 7.

The Bi_2Se_3 thin films were grown by molecular beam epitaxy (MBE) to study the crossover behavior of surface states from a 3D TI to its 2D limit.[4] The energy gap opening was clearly observed from ARPES when the thickness is below six quintuple layers. Figure 1-15 (a) to (e) show a series of ARPES band maps of Bi_2Se_3 films from 1 to 6 QL measured at room temperature.[4] The gap size between the upper and lower surface states decreases as thickness increases from 1 to 5 QL . and the gap completely disappears at 6 QL.. Interestingly, at 3 QL, the upper surface states are split into two branches. The splitting is prominent at larger wave vectors but disappears at the $\bar{\Gamma}$ point. This is a Rashba-type splitting, in which the two sub-bands with different spins shift along the $k_{//}$ axis in opposite directions and degenerate at $\bar{\Gamma}$ point. For thicker films at 5 and 6 QL (Figure 1-15 (d),(e)), the outer two branches of the split upper surface state fade out gradually[4]

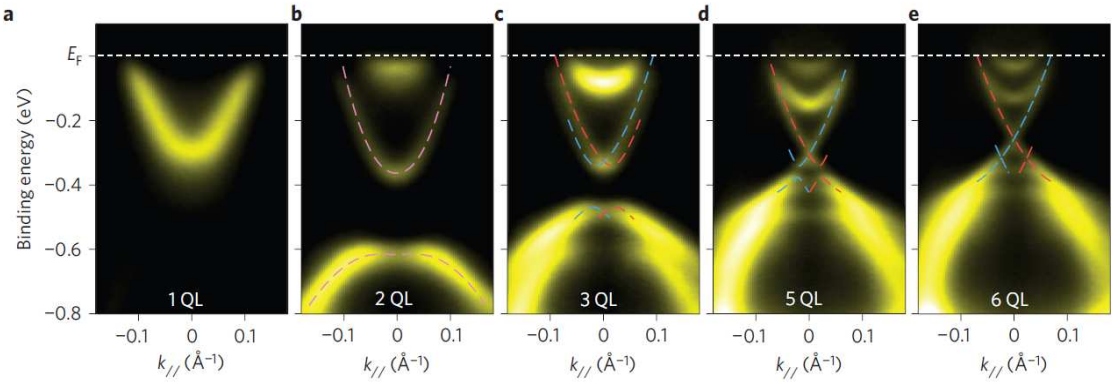

Figure 1-15. ARPES spectra of thickness dependent Bi_2Se_3 films at room temperature. (a) to (e), ARPES spectra of 1, 2, 3, 5 and 6 QL along the $\bar{\Gamma}-\bar{K}$ direction measured at 300 K. Adapted from Ref. 4.

1.4.3. Scanning Tunneling Microscopy (STM) Measurements

Bi_2Te_3 has also been predicted to be a 3D TI with robust and unique surface states consisting of a single Dirac cone at the Γ point.[7] ARPES and scanning tunneling microscopy (STM) experiments have confirmed that the surface states of Bi_2Te_3 have a single non-degenerate Dirac cone with a linear dispersion in momentum space.[40, 44, 46, 47] However, unlike Bi_2Se_3, the surface state of Bi_2Te_3 is a bit more complicated and the Dirac point is embedded underneath the top of the valence band. Therefore it is difficult to probe the surface state near the Dirac point without being disturbed by the bulk carriers. Another difference between these two materials is that the constant energy contour of the Dirac cone is almost spherical in Bi_2Se_3, while it presents significant hexagonal warping in Bi_2Te_3 as shown in Figure 1-16(a)[48]. Starting from the Dirac point, the contour changes from a circle to a hexagon, and becoming warped above about $E \approx -100meV$, which exhibits the deviations from a simple Dirac cone due to a combination of smaller band gap (0.15 eV) and a strong trigonal potential.[3, 40] In addition the ARPES characterization of 3D TI, STM and scanning tunneling spectroscopy (STS) also provide surface-sensitive technique to probe the surface states. The comparison between STM or STS and ARPES was carried out by Alpichshev *et al*. in Bi_2Te_3 sample. It is found that the integrated density of stats obtained from ARPES (Figure 1-16 (b)) agrees well with the differential conductance dI/dV obtained from STS measurements (Figure 1-16 (c).[48] From such comparison, the energy levels (E_F, E_A, E_B, E_C and E_D) can be accurately identified.

In addition, STS/STM work about compound material $(BiSb)_2Te_3$ carried out by our collaborator Yeh's group will be detailed shown in chapter 3.

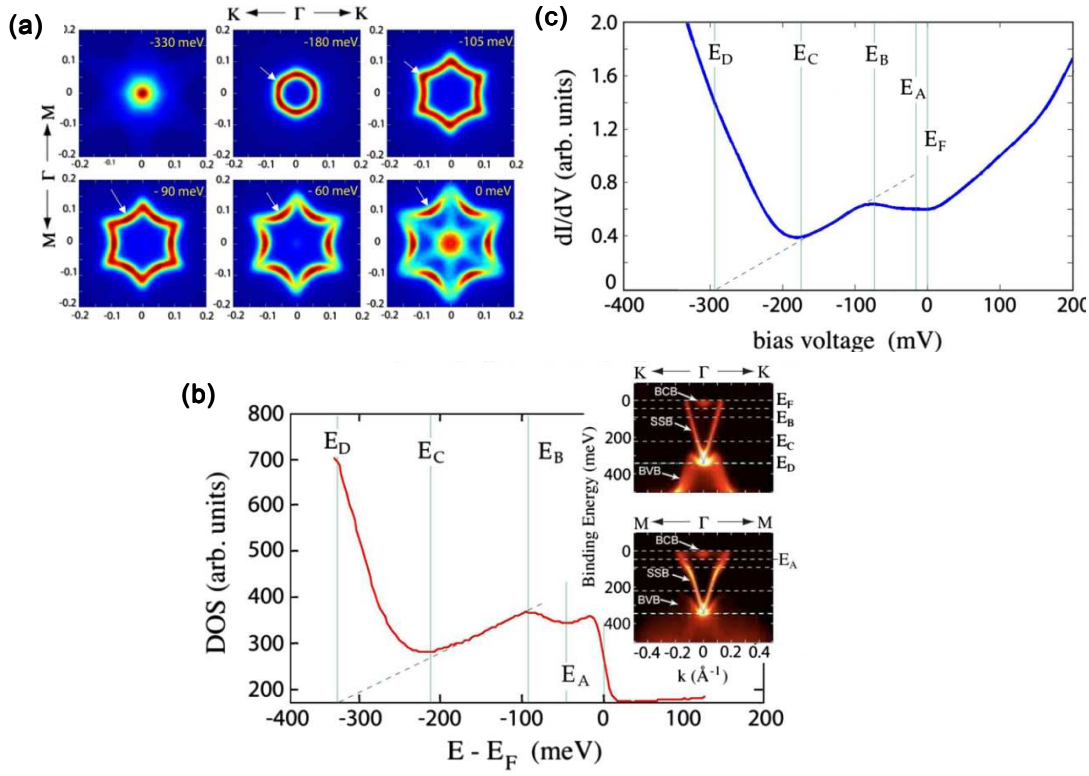

Figure 1-16. DOS of Sn-doped Bi_2Te_3. (a) ARPES-measured constant-energy contours of the SSB. Strength of DOS grows from blue (no DOS) to dark red (strong contribution to DOS). Arrows point to the position of maximum in DOS (note sixfold symmetry). (b) Integrated DOS from ARPES. Here: E_F is the Fermi level; E_A is the bottom of the BCB; E_B is the point of the ‘‘opening up’’ of the SSB; E_C is the top of the BVB; and E_D is the Dirac point. (c) Typical STS spectrum of a 0.27% Sn-doped Bi_2Te_3 sample similar to (b). Note the shift of all energies by 40 meV as a result of doping. of Bi_2Te_3 reveal a hexagonal deformation of surface states. Adapted from Ref. 48.

1.5. Topological Insulator Material Synthesis Methods

1.5.1. MBE grown thin films

For the growth of high-quality epitaxial thin films of TI materials, MBE technique is usually employed. So far, our group has successfully grown single crystalline Bi_2Se_3,[49-51] Bi_2Te_3,[52] $(Bi_xSb_{1-x})_2Te_3$,[53, 54] $(Bi_xSb_{1-x})_2(Se_yTe_{1-y})_3$, Cr-$Bi_2Se_3$, Cr-$Bi_2Te_3$[55] and Cr-$(Bi_xSb_{1-x})_2Te_3$[56, 57]. For epitaxial growth, the lattice matching between the substrate and the grown material is usually very important. However, due to the van der Waals gap between the QLs, the lattice matching with the substrate is not crucial since the substrate and the films are only weakly bonded with the van der Waals force. Till now, we have grown high quality TI thin films on various substrates, such as Si,[49, 50] sapphire, GaAs,[52-54, 56, 57] CdS,[51, 58] InP, $Y_3Fe_5O_{12}$,[59] $SrTiO_3$, as well as mica. Tremendous MBE efforts were also made by other groups, for example, Xue group,[4, 5, 60-62] Samarth group, [63-65] Ando group[66, 67] and others[68-71].

1.5.2. Bulk Single Crystals

Bridgman methods were also widely used to grow bulk 3D TI materials. In this method, the temperature of the melt is gradually reduced while keeping a temperature gradient in the

tube, hence the crystallization starts at the cold end and the crystal grows as the solidification proceeds from this end. Cava group used this method to produce high quality TI materials including Bi_xSb_{1-x} alloy, Bi_2Se_3, Bi_2Te_3, Sb_2Te_3 crystals in the early stage of 3D TI discoveries. [38, 46, 47] The mechanical exfoliation method, also called scotch tape method, was also applied to cleave the TI thin flake from the bulk by the adhesive tape. [72, 73]

1.5.3. Nanoribbons and nanoplates

TI nanoribbons are usually synthesized by gold-catalyzed vapor liquid solid (VLS) technique. Typically, Bi_2Se_3 powder is placed in the hot center of a tube furnace through which Ar gas flows and transport evaporated Bi_2Se_3, while the Si substrates coated with Au nanoparticle are placed in the downstream side of the furnace. The growth of nanoribbons proceeds along with the Au nanoparticles absorb Bi_2Se_3 vapor and leave crystallized Bi_2Se_3 nanoribbons underneath them.[74, 75] When there are no Au nanoparticles serving as catalyst, nanoplates can be obtained instead of nanoribbons. Cui group has been utilized this VLS method to grow high quality TI nanostructures and fabricated them to nanodevices.[75-78]

1.6. Topological Surface State Properties

1.6.1. Dirac Fermion Physics

The Dirac fermions nature of topological insulator have been confirmed by the above mentioned ARPES and STS experiments. Similarly, magneto-transport measurement is another prominent method to detect the existence of surface state through Landau level quantization of energy states by large magnetic fields. The quantization occurs follows[79]

$$E_{\pm}(\mathrm{N}) = \pm\sqrt{(2\,\mathrm{e}\hbar v_F^2\,\mathrm{B})\,\mathrm{N}} \qquad (1\text{-}12)$$

where N = 0, 1, 2, ... This means that in Dirac fermions systems, the LL spacing is not a constant but changes as $\sqrt{N}$, as opposed to ordinary metals in which the LL spacing is simply $\hbar\omega_c$ ($\omega_c = eB/m$) and is independent of the Fermi level (as shown in Eq. 1-1). Also, Eq. (1-12) indicates that there is the 0th LL with N = 0, which is located at the Dirac point. Therefore, the Landau quantization of massless Dirac fermions is characterized by the occurrence of the zero-energy and the symmetrical appearance of $\sqrt{N}$ states on both the positive and negative energy sides of the Dirac point. [80]

When the Landau quantization takes place, the associated quantum Hall effect becomes unusual, and the Hall plateau between the Nth and (N+1)th LLs is quantized to

$$\sigma_{xy} = -\frac{e^2}{h}(\mathrm{N}+\frac{1}{2}) \qquad (1\text{-}13)$$

which is called half-integer quantization,[14] which can also be understood as a result of the π Berry phase, in the Z_2 spinwave function manifold. This indicates that the first Hall plateaus

on the positive and negative energy sides must appear anti-symmetrically, because σ_{xy} is an odd function of energy.

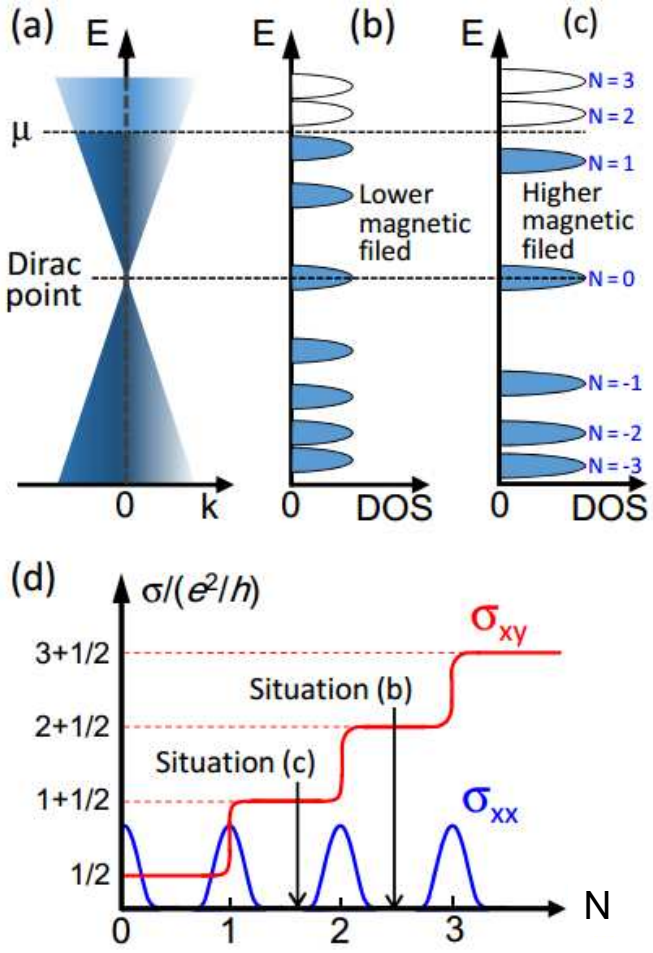

Figure 1-17. (a) 2D Dirac cone; μ is the Fermi level. (b) Landau quantization of the Dirac cone. LLs below μ are filled with electrons. Note that the spacing between LLs change as $\sqrt{N}$ and the N = 0th LL is pinned to the Dirac point. (c) In a larger magnetic field, the spacing between LLs increases as $\sqrt{B}$. (d) Schematic behavior of σ_{xx} and σ_{xy} in the quantum Hall regime of 2D Dirac fermions. the situations depicted in panels (b) and (c) are marked by arrows. Notice that the minima in σ_{xx} indicates a complete filling of up to Nth LLs. Modified

from Ref. 80.

1.6.2. Onsager Relation

We have accounted of the quantization of the electron motion, which restricts the permissible states and is the basic cause for the occurrence of Shubnikov-de Hass (SdH) oscillations. Following the semiclassical approach of Onsager and Lifshitz,[81] we assume that the orbits in a magnetic field are quantized by the Bohr-Sommerfeld relation. The quantization rule for a periodic motion is

$$\oint \boldsymbol{p}\cdot d\mathbf{r}=(N+\gamma)2\pi\hbar \qquad (1\text{-}14)$$

where $\boldsymbol{p}$ and $\boldsymbol{r}$ are the canonically conjugate momentum and position variables, N is an integer and the integration is to be taken round a complete cycle; the phase γ is related to Berry phase. For an electron in a magnetic field, the appropriate meanings of p is

$$\boldsymbol{p} = \hbar\,\mathbf{k}\text{-}e\mathbf{A} \qquad (1\text{-}15)$$

where A is the vector potential of B.

Hence $\oint(\hbar\,\mathbf{k}\text{-}\,e\mathbf{A})dr=(N+\gamma)2\pi\hbar$ (1-16)

Transform the first term in the integral

$$\oint \hbar\,\mathbf{k}\cdot d\mathbf{r}=q\oint \mathbf{r}\times\mathbf{B}\cdot d\mathbf{r}=-qB\oint \mathbf{r}\times d\mathbf{r}=-2q\emptyset \qquad (1\text{-}17)$$

and Stokes' theorem to transform the second, we find

$$q\oint \mathbf{A}\cdot d\mathbf{r}=q\int \mathrm{curl}\,\mathbf{A}\cdot d\boldsymbol{\sigma}=q\int \mathbf{B}\cdot d\boldsymbol{\sigma}=q\emptyset \qquad (1\text{-}18)$$

Add (1-17) and (1-18)

$\oint p \cdot d\mathbf{r} = -\frac{q}{c}\emptyset = (N+\gamma)\, 2\pi\hbar$ (1-19)

Therefore, the quantized magnetic flux is

$\emptyset_n = (N+\gamma)\, 2\pi\hbar / e$ (1-20)

From $\hbar \frac{dk}{dt} = q\frac{dr}{dt} \times B$ (1-21)

$dr = \frac{\hbar}{qB} dk$ (1-22)

The real space of cross section is thus related with k-space cross section

$A_n = (\frac{\hbar}{qB})^2 S_n$ (1-23)

Hence, the quantized magnetic flux is

$\emptyset_n = (\frac{\hbar}{qB})^2 \frac{1}{B} S_n = (N+\gamma)\, 2\pi\hbar / e$ (1-24)

The quantized Fermi area is

$S_n = (N+\gamma)\, \frac{2\pi e}{\hbar} B$ (1-25)

which is also known as Onsager relation.[81]

The increment ΔB for two successive orbits, N and N+1, gives the same area in k space on the Fermi surface. Hence Eq. (1-25) can be deduced as

$S\left(\frac{1}{B_{n+1}} - \frac{1}{B_n}\right) = \frac{2\pi e}{\hbar}$ (1-26)

where S is the Fermi area, therefore $\Delta\frac{1}{B} = \frac{2\pi e}{\hbar}\frac{1}{S}$ (1-27)

Particularly, for TI material $S = \pi k_F^2$, therefore

$\frac{1}{B} = \frac{2e}{\hbar}\frac{1}{k_F^2} = \frac{4\pi e}{h}\frac{1}{k_F^2}$ (1-28)

where k_F is the Fermi vector.

1.6.3. Quantum Oscillations

When the Landau quantization of energy states occurs with large magnetic fields, the DOS become periodically modulated as a function of magnetic field, which leads to quantum oscillations. In particular, the oscillations occurring in conductivity are called SdH oscillations and the oscillation follows

$$\Delta(1/B) = e/(hn_{2D}) \quad (1\text{-}29)$$

$$\Delta(1/B) = 4\pi e/k_F^2 h \quad (1\text{-}30) \text{ (same as Eq. (1-28))}$$

where B is magnetic flux density, n_{2D} is the 2-D carrier density, k_F is the Fermi vector, e is the electron charge, and h is the plank constant. In 3D TI magneto-transport studies, the SdH oscillations are often used to selectively characterize the 2D metallic surface states which coexists with 3D bulk states. By analyzing the oscillations data with Eqs. (1-29) and (1-30), various surface states parameters can be extracted, such as, Fermi Level position (E_F), Berry phase (γ), surface state 2D carrier concentration (n_{2D}).

To date, numerous effort has been devoted to magneto-transport measurements, especially through SdH oscillations to probe the surface states properties.[4, 38, 40, 44, 46, 51, 70, 78, 82-90] However, the real TI materials always have impurities and defects such as vacancies and antisites. [78, 91, 92] Therefore, the as-grown materials are not truly insulating but with a bulk carrier density, which makes difficulties to the transport methods. To reach the

intrinsic TI surface state, various efforts have been made to reduce the bulk carrier density, such as gating effect to deplete the bulk carriers, surface passivation to protect TI surface from doping and oxidation, and counter doping to compensate the additional carriers, which will be further discussed in chapters 2 and 3.

Gate controlled SdH oscillation has been observed in Bi_2Te_3 nanowires by Xiu *et al.* as shown in Figure 1-18 (a);[88] correspondingly, the fast Fourier transform (FFT) spectra show dominant oscillation frequencies (f_{SdH}(T), Figure 1-18 (b)), in accordance with the SdH periodicities (Figure 1-18 (a)). The SdH amplitudes as a function of temperature were analyzed to obtain more information about the surface states under constant voltages of +80 V (Figure 1-18 (c)). Oscillation amplitudes at both voltages decrease rapidly with a temperature increase from 1.4 to 8 K. [88]

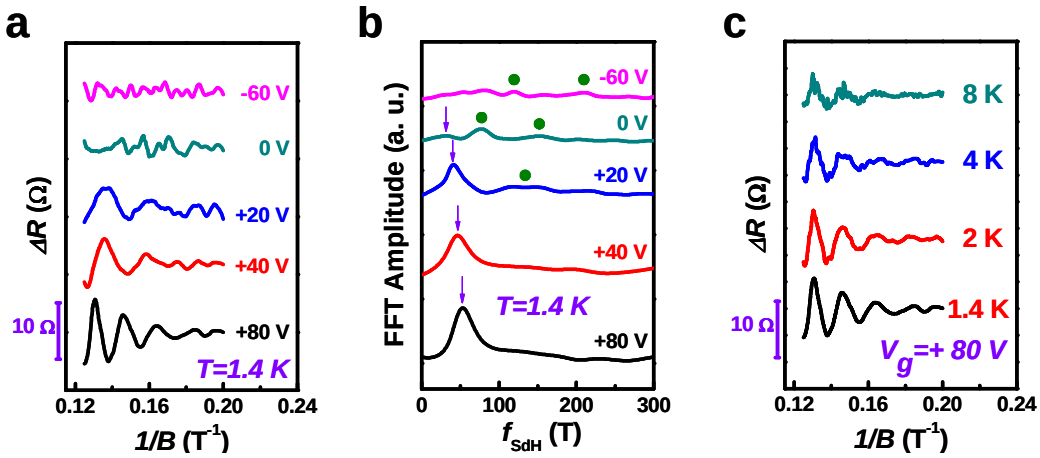

Figure 1-18. Shubnikov-de Hass (SdH) oscillations in a nanoribbon FET. (a) The oscillations become more pronounced as the gate voltage increased from -60 V to +80 V at *T*=1.4 K. (b) The purple arrows in the corresponding FFT spectra indicate the frequency of

the SdH oscillations which represent the surface states. The green solid dots indicates the possible presence of other oscillation frequencies, which are developed when the bulk carrier concentration increases under negative gate voltages. (c) The oscillations also become more pronounced as the temperature is decreased from 8 K to 1.4 K at gate voltages of + 80V. (This also appears in one of my publications Ref. 88)

1.6.4.Weak antilocalization and weak localization

As mentioned in session 1.2.1, the π Berry phase associated with the TI surface carriers leads to the Weak antilocalization (WAL) effect. WAL is always related to strong spin-orbit scattering or coupling , and was first derived by Hikami, Larkin and Nagaoka.[93] In the quantum diffusion regime (mean free path $\ll$ system size ~ phase coherent length), an electron maintains its phase coherence after being scattered by static centers for many times.[94] As a result, the destructive quantum interference can give an enhancement to the classical electronic conductivity, leading to WAL[95]. Applying a magnetic field tends to break the destructive interference, giving rise to a negative magnetoconductivity (MC), a key signature of WAL.

In the limit of strong spin-orbit interaction in 2D electron systems, the standard Hikami-Larkin-Nagaoka (HLN) theory is often applied for weak-field conductivity variation:[93]

$$\Delta\sigma = \frac{\alpha e^2}{2\pi^2\hbar}\left[\ln(\frac{\hbar}{4eBl_\phi^2}) - \psi(\frac{1}{2}+\frac{\hbar}{4eBl_\phi^2})\right] \quad (1\text{-}31)$$

where ψ is the digamma function, and the prefactor α should be equal to -1, 0, 1/2 for the orthogonal, unitary and sympletic cases, respectively. One topological surface that carriers a π Berry phase should give an $\alpha = 1/2$. In the weak interband coupling limit, multiple independent bands with WAL should add up to give bigger α, *e.g.*, α = 1 (2 surface states), α =1.5 (2 surface states + decoupled bulk).

On the other hand, weak localization (WL) arises as a result of the gap opening at the Dirac point. Either the hybridized gap or the magnetic scattering can drive MC of the system from WAL to a parabolic dependence on the magnetic field (B^2). Further increasing the gap (Δ)/Fermi energy (E_F) ratio may drive the system to WL regime. A crossover from WAL to WL is expected tunable by the TRS-breaking gap or the position of Fermi level. The relation of the Berry phase with the gap Δ and E_F is determined by

$$\phi = \pi\left(1 - \frac{\Delta}{2E_F}\right) \quad (1\text{-}32)$$

It gives π for WAL when $\Delta/2E_F$=0, and 0 for WL when Δ=2E_F.

1.7. Organization

The contents of this dissertation are arranged as follows. Chapter 1 provides a historical background of the discovery of TIs starting from QHE, QSHE to QAHE. We also discuss

the basic physical properties related to 2D and 3D TIs as well as their characterization methods. In chapter 2, we show that *in situ* Al passivation inside a MBE chamber could reduce the environmental doping and surface degradation process, in order to reveal the pristine topological surface states. In contrast, we show the degradation of surface states for the unpassivated control samples, in which the 2D carrier density is increased 39.2% due to ambient *n*-doping, the SdH oscillations are completely absent, and a large deviation from WAL is observed. Chapter 3 presents the evidence of a surface gap opening in TI thin films of $(B_{i0.57}Sb_{0.43})_2Te_3$ below six quintuple layers through transport and scanning tunneling spectroscopy measurements. By effective tuning the Fermi level via gate-voltage control, we unveil a striking competition between WL and WAL at low magnetic fields in nonmagnetic ultrathin films. Chapter 4 focuses on the study of magnetic properties of Bi_2Se_3 surface states in the proximity of a high T_c ferrimagnetic insulator YIG. A magnetic signal from the Bi_2Se_3 up to 130 K is clearly observed by magneto-optical Kerr effect measurements. The conclusion of this dissertation is given in Chapter 5.

Chapter 2

Revelation of Topological Surface States by *in-situ* Al Passivation

2.1. Motivation of Surface Passivation in TIs

Among all reported 3D TI materials, Bi_2Se_3 offers a large bulk band gap of 300 meV and a simple Dirac cone surface spectrum, and therefore serves as a good candidate to investigate 3D TIs.[3] To date, extensive magnetotransport experiments in Bi_2Se_3 reveal its novel surface states by angle-dependent SdH oscillations in single crystals[96] and Aharonov-Bohm interference in nanoribbons[92]. Nevertheless, the degradation of surface states continuously presents as a critical challenge for the further development of topological physics and practical devices. For example, Analytis *et al.*[83] reported the absence of pronounced SdH oscillations after ~1 hour's atmosphere exposure. They also claimed that air exposure cause n-type doping in Bi_2Se_3 on the surface. Taskin *et al.*[97] measured SdH oscillations in the sample 5 hours after cleavage as *p* type, and changed to *n* type 725 hours later in air exposure at 300 K.

X-ray photoelectron spectroscopy (XPS) demonstrates that the rapid formation of native oxide (BiO_x) served as the physical origin of surface degradation and environmental doping on Bi_2Se_3[98]. In order to examine the physical origin of the environmental doping on Bi_2Se_3, surface chemistry probe XPS was used to characterize the composition at the surface of Bi_2Se_3 nanoribbons and bulk single crystals. For as-grown nanoribbons (Figures

2-1 (a) and (b)), a bismuth oxide (BiO_x) peak was observed. The BiO_x peak kept growing as the air exposure time increases, corresponding to the increase of BiO_x thickness. Selenium oxide (SeO_x) was also observed (Figure 2-1 (b)) in the nanoribbons exposed in air for 5 days, an XPS study was performed on bulk single crystals of Bi_2Se_3 with low carrier concentrations. The Bi_2Se_3 crystal was loaded into the XPS sample chamber right after cleaving (within 10 s) and pumped down to vacuum with high-purity N_2 gas flux. The BiO_x signal was clearly observed in the final spectra (Figures 2-1 (c) and (d)), indicating the formation of the "native" oxide is really fast.[98] Therefore surface passivation of TI material is of great importance for surface related transport study, which brings to the theme of this chapter.

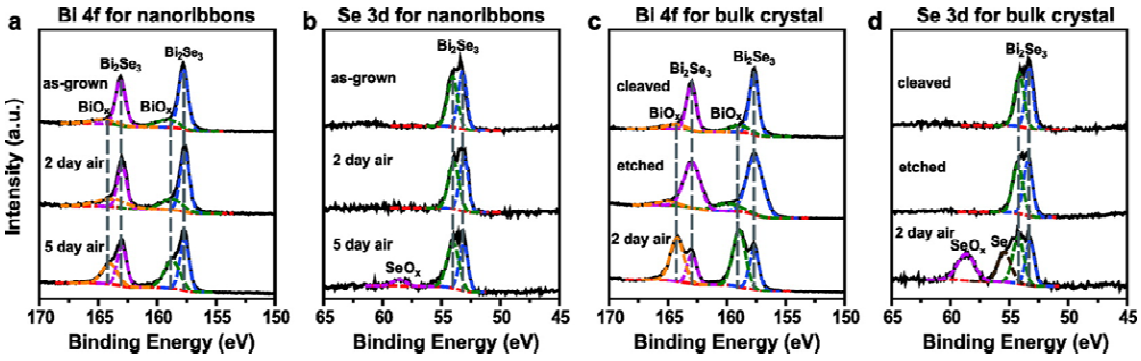

Figure 2-1. XPS studies on Bi_2Se_3 nanoribbons with Bi 4f (a) and Se 3d (b) spectra, including samples after synthesis, aged in air for 2 days, and aged for 5 days. XPS studies on a Bi_2Se_3 single crystal with Bi 4f (c) and Se 3d (d) spectra, including samples right after cleaving (< 10 s air exposure), etched with Ar plasma for 5 min, and aged in air for 2 days. Adapted from Ref. 98.

In addition, hydroxyl groups were also reported as surface impurities under humid ambient conditions.[83] Therefore, the passivation of topological surface states is of great importance for TI study.

In this chapter, we will present an effective approach to passivate the Bi_2Se_3 surface with 2 nm aluminum (Al) deposition, immediately after the growth of Bi_2Se_3 thin films in MBE chamber (without breaking the ultra high vacuum). In order to understand the role of the Al passivation, control samples (without Al deposition) were grown under the same condition for comparison. Dual evidences from both SdH oscillations and weak antilocalization (WAL) suggest that non-trivial surface states are better revealed by *in situ* Al passivation, as it prevents native oxide (BiO_x) formation and isolates the film from ambient charges/impurities or contaminations in the subsequent fabrication process.[83, 91, 97] Our results hence demonstrate that surface passivation is critical in TI surface states related transport studies, which could pave the way for the future practical applications, *i.e.*, thermoelectric, low-noise interconnects, with possibility of extending into the low-dissipation electronics. [72, 73, 99-101]

2.2. Material Growth and Sample characterization

2.2.1 MBE Growth of Bi_2Se_3 on Si with and without Al Passivation

High-quality single crystalline Bi_2Se_3 thin film was conducted in a PerkinElmer MBE system; MBE is a proven powerful and reliable technique to produce ultrathin TI films down to a few quintuple layers[49, 84]. The highly resistive Si (111) substrate with a resistivity $>10^4 \Omega \cdot cm$ was cleaned by the well established RCA procedure before loading into the MBE chamber. High-purity Bi (99.9999%) was evaporated by conventional effusion cells at 480 °C, while the Se (99.99%) sources was evaporated by a cracker cell from SVTA at 230 °C, and Si (111) substrate was kept at 250 °C during the growth. The atomically flat layer-by-layer growth of Bi_2Se_3 was monitored by real-time reflection high energy electron diffraction (RHEED). After growing 8 QLs (~8 nm) of Bi_2Se_3, a post-annealing was carried out at 400 °C. The thickness of 8 nm was chosen to preserve the topological surface states[4] while minimizing the contribution from the heavily doped bulk by increasing the surface-to-volume ratio. After the Bi_2Se_3 growth, a 2 nm Al was *in situ* evaporated to passivate the surface at room temperature. Al film was later naturally oxidized to form Al_2O_3 after the sample was taken out of the chamber and exposed in air, which also further served as a part of the high-κ dielectric oxide in the atomic layer deposition (ALD) process. Control samples without *in situ* Al evaporation were grown under the same condition. All the samples were exposed in air for 1 day before fabrication process.

2.2.2. Atomic Force Microscope Characterization

Atomic force microscopy (AFM) was performed to investigate the Al passivated and un-passivated Bi_2Se_3 thin film surface morphology. Figure 2-2 (a) shows a typical AFM image of the *in situ* Al capped 8 quintuple layers (QLs) Bi_2Se_3 film with ~400 nm large-scale triangle-shape terrace. Due to the naturally formed Al_2O_3 coverage, the terrace edge is not as sharp as that in the un-capped thin film, as shown in Figure 2-2 (c). Figures 2-2 (b) and (d) display the height profile of the red and blue lines marked in Figure 2-2 (a) and (c), respectively. The uniform formation of the Al_2O_3 layer is confirmed by the sub-nanometer roughness of the height profile in Figure 2-2 (b). For both films with and without Al capping, the height of each step is ~0.95 nm, which is consistent with the reported thickness of one Bi_2Se_3 QL.[49, 58, 102]

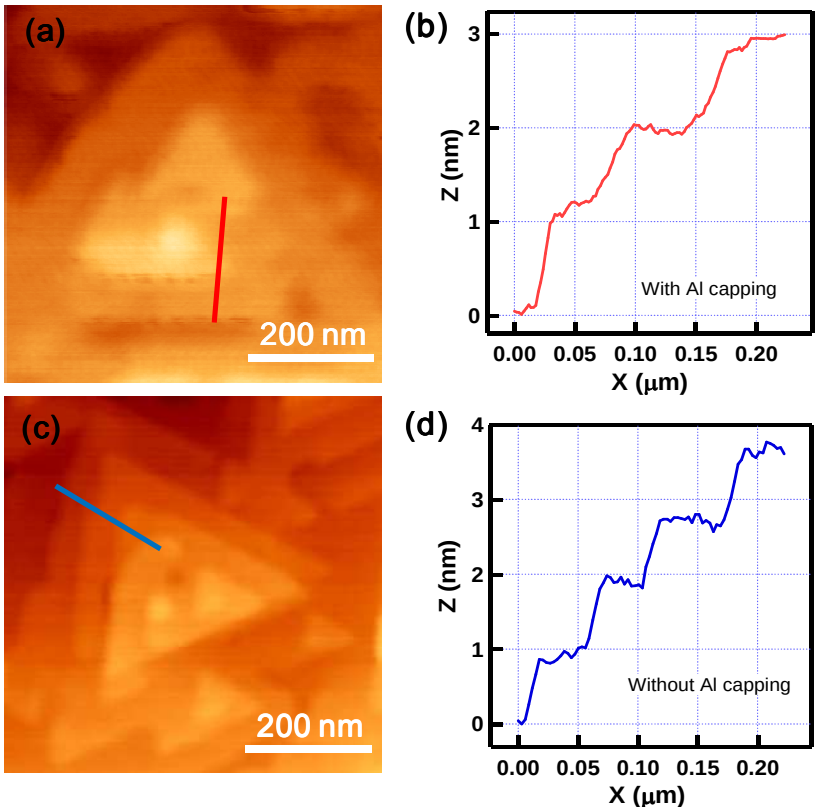

Figure 2-2. (a) AFM image of the in-situ Al passivated 8 QLs Bi_2Se_3, with ~400 nm large-scale triangle-shape terraces. Due to the coverage of the thin Al_2O_3 layer, the terrace edge is rounded. (b) The height profile along the solid red line marked in (a). The sub-nanometer roughness of the profile demonstrates the uniform formation of the thin Al_2O_3 layer. (c) AFM image of 8 QLs Bi_2Se_3 without Al passivation, which shows sharp and clear terrace edge. (d) The height profile along the blue line marked in (c), showing a step size of ~0.95 nm. (This also appears in one of my publications Ref. 86.)

2.2.3. Device Fabrication Methods

To investigate the transport properties and explore the surface states in the passivated and un-passivated Bi_2Se_3 thin film, top-gate field effect transistor (FET) devices with a six-terminal Hall-bar geometry were fabricated, as schematically shown in Figure 2-3 (a).

The MBE grown 8QLs Bi_2Se_3 thin film was patterned into a micron-scale Hall bar geometry using conventional optical photolithography and a subsequent dry etching (20 s CHF_3 etching). The 18 nm Al_2O_3 dielectric layer was conformally deposited by ALD at 150°C to serve as the high-κ gate dielectric. Six Hall channel contacts (10 nm Titanium (Ti) and 90 nm gold (Au)) were defined by e-beam evaporation after dry etching the Al_2O_3 in the contact areas. The top-gate metal was defined by another step of photolithography, followed by metal deposition (Ti/Au 10nm/90m) to finalize a top-gate FET fabrication process.

2.2.4. Device Measurement Setup and Methods

Standard four-point Hall measurement was carried out to eliminate the contact resistance with a constant AC current flow of 1 μA at 11.58 Hz. The measurements were conducted in a Quantum Design Physical Properties Measurement System (PPMS) with the application of tilted magnetic fields. The temperature range was varied from 1.9 to 300 K, and the magnetic field was up to ± 9 T. Figure 2-3 (b) presents an optical image of the

device structure. The diagonal two electrodes were top-gate electrodes, while the rest electrodes were connected to the Hall bar. A zoom-in view of the Hall bar (10 μm (*L*) × 20 μm (*W*)) is shown in the inset, with a 10 μm scale bar.

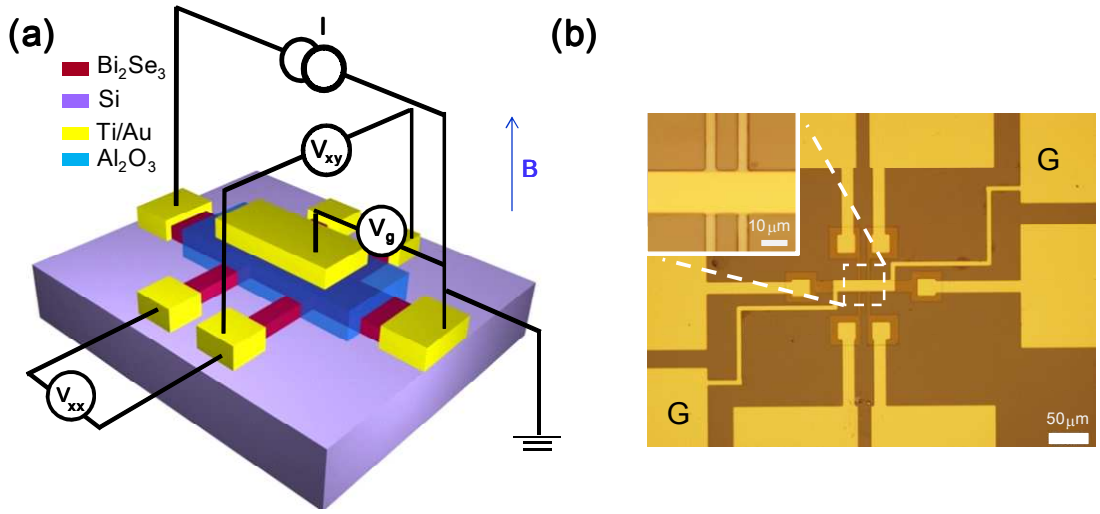

Figure 2-3. Top-gate FET structure and measurement setup. (a) Schematic diagram of a top-gate Hall bar device structure with 8 QL Bi_2Se_3 sample (red) on highly resistive Si (111) (purple) with measurement setup. The total thickness of Al_2O_3 (blue) is ~23 nm. The Al_2O_3 covers the whole substrate except the six Hall bar contact area. Here, the Al_2O_3 coverage is purposely reduced for clarity. A standard four-point measurement was carried out with constant AC current flow of 1μA. (b) Optical image of the device structure with the 50 μm scale bar. Inset: A zoom-in view of optical image of the Hall bar with the size of 10 μm (*L*) × 20 μm (*W*). (This also appears in one of my publications Ref. 86.)

2.3. Transport Comparison Between Samples with and without Al Passivation

2.3.1. Temperature Dependence of Resistances

Figure 2-4 (a) and (b) present the temperature dependent sheet resistances (R_s–T) of Bi_2Se_3 thin films with and without Al passivation. These two curves exhibit common features in the high temperature range (between 250 K and 35 K). First, the sheet resistances of both samples exponentially increase as temperature decreases in the temperature range from 250 K to 180 K, which is similar with the R_s-T curves of low bulk carrier densities ranging from 10^{16} cm^{-3} to 10^{17} cm^{-3} that Analytis *et al.*[83] reported. Second, between about 35 K and 180 K, the sheet resistances decrease with the reduced temperature, implying a typical metallic behavior, in which the phonon scattering mechanism dominates.[91, 96, 103] However, below 35K, the R_s-T manifests a dramatic difference between these two samples: the device with *in situ* Al passivation displays more resistive behavior, revealing that the bulk carriers further freeze out, and therefore surface conduction is enhanced at this temperature range. But the associated activation energy E_a cannot simply be extracted by $R \sim e^{E_a/k_BT}$ owing to the presence of multiple-channel conduction,[88] where R is the channel resistance, k_B is the Boltzmann constant. In contrast, the sheet resistance of the un-passivated sample continuously decreases and shows a shallow local minimum at 10 K. This behavior was also observed in higher doping concentration ($n \sim 10^{19}$ cm^{-3}) Bi_2Se_3

crystals by others.[82, 83] It is noted that un-passivated devices shows a dramatic reduction in sheet resistivity compared with the sample with Al passivation, which is believed to be associated with the increase of the carrier density to be discussed later.

2.3.2. Gate Voltage Dependence of Resistances

The gate dependence of Hall carrier densities n_H in both samples at 1.9 K are extracted from $n_H = (R_H e)^{-1}$, where R_H is the Hall slope, e is the electron charge. In Figure 2-4 (c), the bulk carrier density is reduced as the gate voltage decreases, indicative of *n*-type bulk Bi_2Se_3 which has been believed to be associated with Se vacancies.[78, 91, 92] For the device with Al passivation, the 2D carrier density can be tuned from $5.45\times10^{13} cm^{-2}$ to $7.58\times10^{13} cm^{-2}$ (with a carrier density change of 39.1%), by sweeping gate voltage (V_g) from -10 to +10 V. In comparison, the un-capped device shows a 39.2% higher carrier concentration at zero gate bias with a relatively low gate modulation of 13.2%. This implies that the difference of the carrier concentrations arises from the unintentionally environmental *n*-type doping which contributes to the transport.[83, 91] As aforementioned, other surface impurities/oxides such as hydroxyl groups,[83] surface native oxide (BiO_x),[98] trapped charges and impurities from ambient as well as contaminations in the fabrication process may all contribute to *n*-type doping. Hence, the original surface properties cannot be easily revealed if the surface is directly exposed to air or chemicals during the device

fabrication. Figure 2-4 (d) presents the R_s vs. V_g at various temperatures for the Al capped device. The inset of Figure 2-4 (d) shows the slope of the sheet resistance as a function of the gate voltage at 1.9 K, indicating a sharper increase in resistance beyond -4 V. This enhancement of the gating effects strongly suggests that the Fermi level is approaching the edge of the conduction band at a gate voltage of -4 V. Beyond -4 V, a large portion of bulk electrons are depleted as the Fermi level is moved into the bulk bandgap.[78]

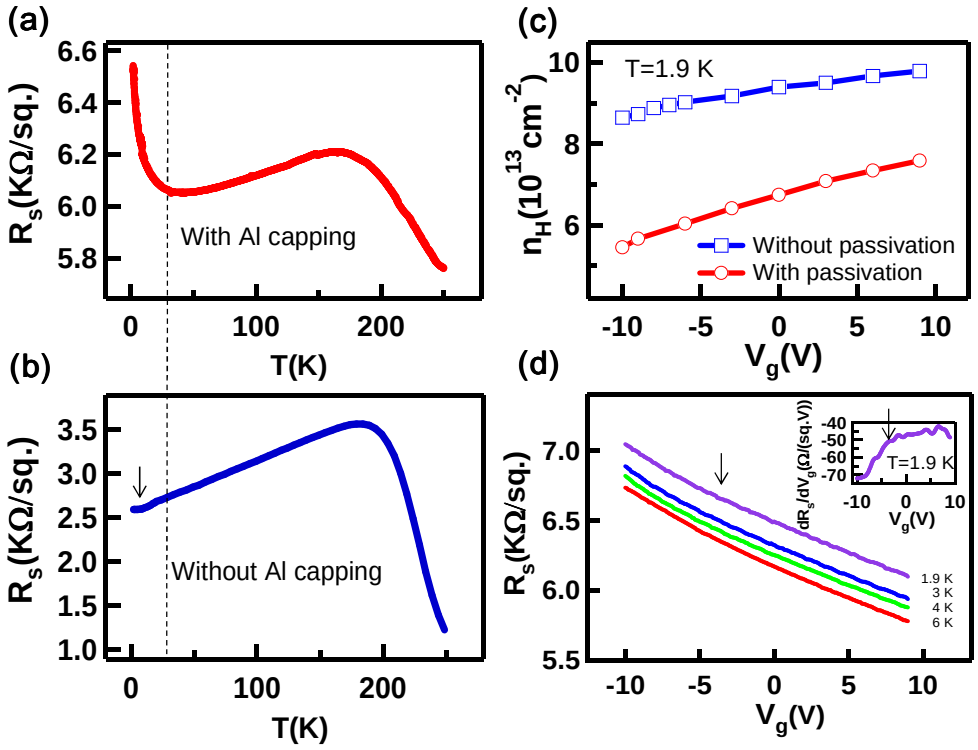

Figure 2-4. Transport properties in passivated and un-passivated devices. (a)(b) Sheet resistances as functions of temperature, for the device with (a) and without (b) surface passivation. Two R_S-T curves ((a) and (b)) show similar behavior at high temperature, but present a dramatic difference below 35 K, as indicated by the dashed line. The sheet resistance of the passivated device increases as temperature reduces; while for the

un-passivated sample, the R_s continuously decrease and shows a shallow local minimum at 10 K. (c) Gate-voltage dependence of 2D Hall carrier density for devices with (circles) and without (squares) Al passivation. The Hall carrier density n_H increases 39.2% at zero bias for un-passivated sample over the passivated one. (d) Sheet resistance vs. gate voltage at 1.9 K, 3 K, 4 K and 6 K. Arrows were used to guide the eyes, showing the sharper increase of resistance with V_g < -4 V. Differential resistance vs. gate voltage is shown in the inset to highlight the enhancement of gating response. (This also appears in one of my publications Ref. 86.)

2.3.3 Shubnikov-de Hass Oscillations in Al passivated Bi_2Se_3 samples

Aiming to probe the surface electronic states for both devices, magnetotransport measurements with an out-of-plane magnetic field were conducted at low temperatures. Both gate voltage and magnetic field (B) dependences of longitudinal and transverse resistances R_{xx} and R_{xy}, were recorded at various temperatures. Here, R_{xy} has a positive value at positive B field. Interestingly, in the sample with *in situ* Al capping, the magnetoresistance (MR) exhibits significantly enhanced SdH oscillations with the decrease of gate voltage (-9 ~ -12 V). However, SdH oscillations are completely absent in the control samples without Al capping. One possible reason is that a higher carrier concentration of the un-passivation sample suppresses the contribution from the surface state in the total

conductivity, and thereby the surface property is masked.[88, 98] Another possibility could be the surface oxidation of Bi_2Se_3 in air which obscures the surface state properties due to interfacial defects or trapped charges.[98]

Figure 2-5(a) presents the derivative of the transverse magnetoresistance (dR_{xy}/dB) as a function of *1/B* for the *in situ* Al capped device. The amplitudes of the SdH oscillations are gradually enhanced with the gate bias changing from -9 to -12 V, suggesting that the bulk contribution is reduced by the external gate bias. The periodicity of such oscillations at 1.9 K are monotonically reduced by a decreasing gate voltage from -9 to -12 V, which corresponds to the shrinking cross sectional area of Fermi surface (S_F) in the momentum space as the Fermi level (E_F) approaches the Dirac point. The gate-voltage dependent Fermi wave number k_F can be extracted through $\Delta(1/B) = 2e/k_F^2\hbar$ [81] for Dirac electrons, yielding the k_F values from 0.067 Å^{-1} to 0.055 Å^{-1} as gate voltage is swept from -9 to -12 V, where $\hbar$ is the normalized Planck's constant *h* divided by 2π.

Landau Level (LL) fan diagram is usually examined to study the Berry phase in graphene[104, 105] and surface states of TIs[83, 89, 103]. Here, we assign Landau level number *n* (*n*+1/2) to the minima (maxima) in the oscillations of dR_{xy}/dB shown in Figure 2-5 (a), in which n indicates *N*+1/2-th LL, when E_F is precisely between adjacent LLs[103]. Based on the Onsager equation: $2\pi(n+\gamma) = S_F \frac{\hbar}{eB}$ [81] (see Eq. 1-25 in session 1.6.2), we linearly fit the SdH oscillation data in the LL fan diagram to obtain γ, where the *n* is the *n*-th Landau level, and the S_F is the cross sectional area of Fermi surface. γ is directly related to the

Berry phase. For a parabolic energy-momentum (E-K) band structure, γ equals 0, corresponding to a zero Berry phase; for the linear E-K relationship of Dirac fermions, γ equals $\frac{1}{2}$, corresponding to a π Berry phase.[106, 107] Particularly, for TI surface states, the linear fitting of LL fan diagram should theoretically extrapolate to 1/2 on the n-axis. Experimentally, in Figure 2-5 (b), the LL fan diagram represents the values of *1/B* at the minima (maxima) in dR_{xy}/dB as a function of n (n+1/2) at V_g = -12 ~ -9 V at T = 1.9 K. The frequencies of gate dependent SdH oscillations, given by the slopes of the linear fitting, are extracted as 98, 112, 135, 148 T, under gate voltage V_g = -12, -11, -10 and -9 V, respectively. The inset shows the gate bias dependence of the intercept γ, which yields a finite Berry phase. γ is close to 1/2 at V_g = -12, -11 V, while it deviates away from 1/2 as the gate voltages increases, implying that the Fermi levels are moved from Dirac-like E-K dispersion (π Berry phase) towards quadratic E-K dispersion (zero Berry phase).[106] This intercept deviation was also discussed in other literatures.[83, 89, 106]

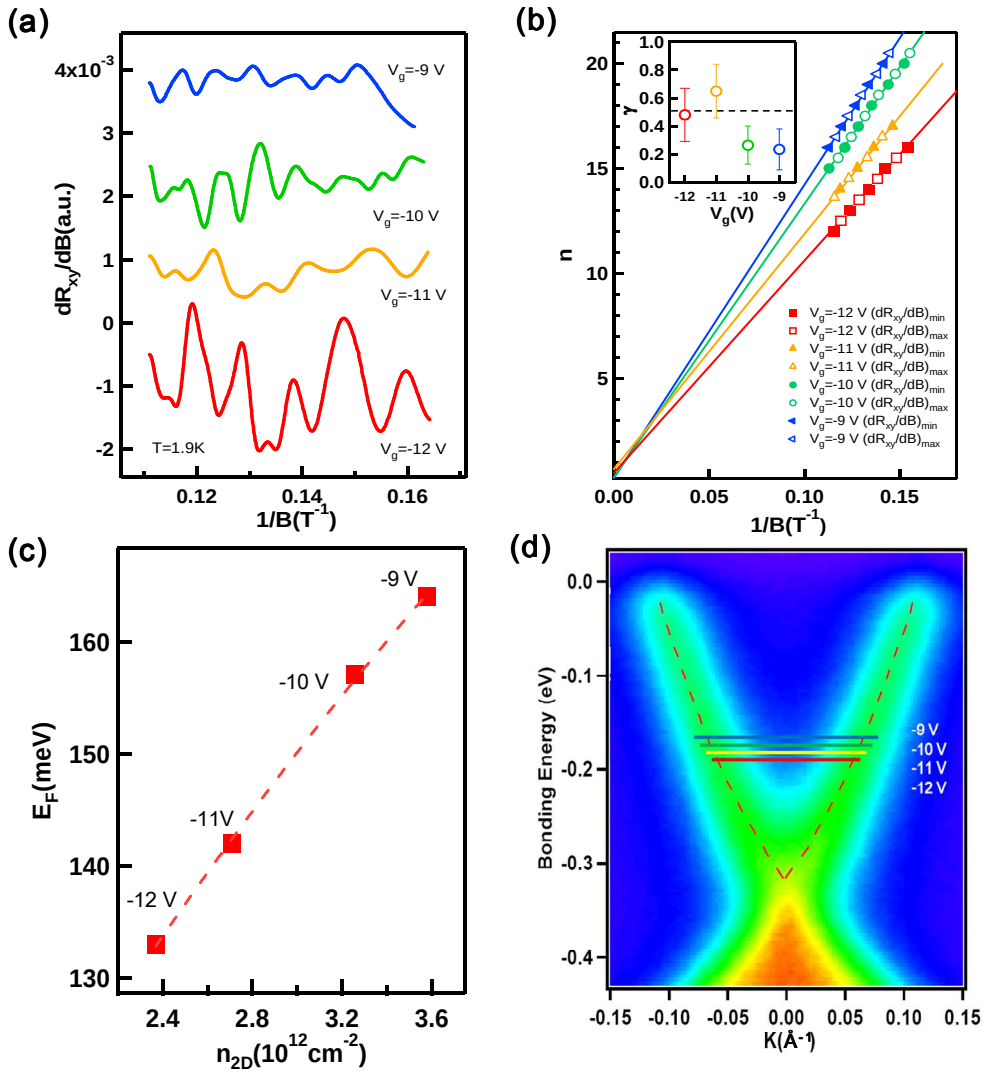

Figure 2-5. Gate-modulated SdH oscillations for the Al passivated sample. (a) dR_{xy}/dB vs. $1/B$ under gate voltage V_g = -12 ~ -9 V at 1.9 K, where all curves are vertically shifted for clarity. Strongly enhanced oscillations are observed when the gate bias is at -12 V. (b) Landau level fan diagram for oscillations in dR_{xy}/dB at V_g= -12 ~ -9 V. The minima (solid symbols) in dR_{xy}/dB are assigned to their indices n, while maxima (open symbols) are assigned to n+1/2. The lines correspond to a linear fit to the solid and open symbols. Inset: n-axis intercept γ as a function of gate voltage. The black dashed line indicate γ =1/2. (c)

Fermi energy E_F as a function of Surface 2D carrier density n_{2D} extracted from corresponding SdH oscillations. (d) ARPES intensity map of the surface states of Bi_2Se_3 thin film near the Γ point with an incident photon energy of 52 eV. The Fermi level E_F for transport measurement (horizontal lines) shifts towards the Dirac point as the gate voltage is decreased from −9 to -12 V. (This also appears in one of my publications Ref. 86.)

Figure 2-5 (c) displays 2D surface carrier density n_{2D} as a function of Fermi energy E_F. n_{2D} is effectively tuned from $3.58\times10^{12} cm^{-2}$ down to $2.37\times10^{12} cm^{-2}$ by sweeping the gate voltage from -9 to -12 V, providing a picture for the evolution of the carrier depletion by the gating effect. Here, n_{2D} is deduced *via* $f = 2\pi\hbar n_{2D}/e$ (also see Eq. 1-29 in session 1.6.2), where *f* is the above-mentioned SdH oscillation frequency obtained from the slope of the linear fitting in Figure 2-5 (b). The Fermi energy E_F corresponding to each gate voltage is given by $E_F = V_F \hbar k_F$, which can be swept from the conduction band down to 133 meV above the Dirac point under gate bias from 0 V to -12 V. Here, the Fermi velocity V_F is estimated as $3.7\times10^5 m/s$, at E_F ~140 meV above the Dirac point, *via* $V_F = \frac{1}{\hbar}\frac{dE_F}{dk_F}$ from ARPES data shown in Figure 2-5 (d), which is consistent with literatures reported data[4, 46, 83, 91], as summarized in Table 1. The Fermi level at gate voltage V_g = -9, -10, -11 and -12 V are sketched (horizontal lines) in Figure 2-5 (d), which are shifted towards the Dirac point as V_g decreases.

Table 1. Fermi velocity V_F of Bi_2Se_3 surface states from ARPES.

Reference	V_F(×10^5 m/s)	Remark
Ref. [46]	3.4 ± 0.3	Calculated*
Ref. [4]	4.5	Reported
Ref. [83, 91]	4.2	Reported
Ref. [58]	3.5 ± 0.2	Calculated*
Our sample	3.7 ± 0.1	Calculated*

*Note: calculated local V_F at ~140meV above the Dirac point.

2.3.4. Angle Dependence of Magnetoconductivity

We next explore the WAL effect for Al capped sample, which has also been observed in other materials systems with a strong spin-orbit coupling [93, 95, 108-110]. The occurrence of WAL in TIs reflects the nontrivial topology of the surface states, in which backscattering is minimized owing to the destructive interference between two time-reversed loops, arising from the π Berry phase. When a magnetic field is applied perpendicular to the film, the time reversal symmetry is broken while the possibility of backscattering increases and the WAL is suppressed.[70, 84] However, the experimentally observed magnetoresistance may be a collective result from both surfaces and bulk channels.[111] The bulk channels do not necessarily contribute to the WAL effect. The tilted magnetic field measurements allows us to distinguish the 2D WAL effect associated with the topological surface states from the 3D bulk effect.[112] The normalized low field MC $\Delta\sigma(B) = \sigma(B) - \sigma(0)$ conducted in tilted magnetic fields at 1.9 K is shown in Figure 2-6 (a), where WAL effect strongly depends on

the tilting angle. When *B* field applied in the film plane, *i.e.* $\theta = 0^{\circ}$, the magnetoconductivity (MC) sharp cusp feature disappears completely and the MC shows a parabolic *B* field dependence. By subtracting the in-plane background from the MC obtained at perpendicular magnetic field, the WAL effect from the 3D bulk can be excluded. Moreover, the 2D TI bulk channels may result in the unitary behavior (MC proportional to the square of the magnetic field) or even weak localization (WL) effect due to the relatively large gap, which has been theoretically demonstrated by Lu *et al.*[111] This unitary behavior or even WL effect of bulk channels may explain why the bulk channels contribute small MC although they actually dominate the transport.[111]

Therefore, we conclude that the α close to 0.5 (Figure 2-6 (b)) at V_g = -11 V, obtained by numerical fitting is mainly due to the top surface conduction. This is in agreement with recently experimental studies on the WAL in Bi_2Se_3[70] and Bi_2Te_3[112].

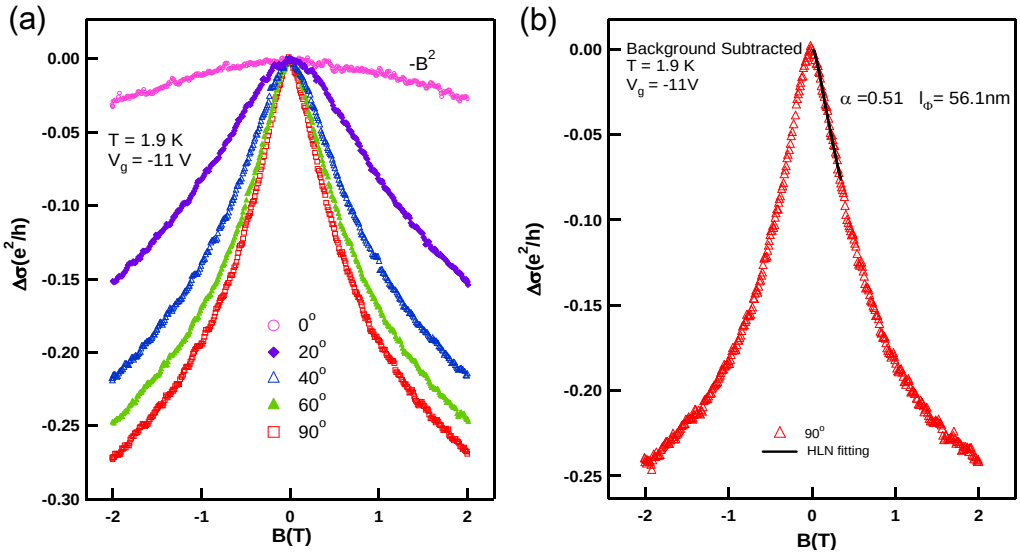

Figure 2-6. (a) Normalized magnetoconductivity ($\Delta\sigma(B) = \sigma(B) - \sigma(0)$) as a function of

tilted magnetic field at T = 1.9 K, V_g = -11 V. When $\theta = 90^\circ$ (out of plane magnetic field), the MC shows sharp cusp (WAL effect) around $B=0$, while when $\theta = 0^\circ$ (in plane magnetic field), MC shows a parabolic B field dependence. (b) In-plane background subtracted MC ($\Delta\sigma(B) = \sigma(\theta = 90^\circ, B) - \sigma(\theta = 0^\circ, B)$) as a function of perpendicular magnetic field at T = 1.9 K, V_g = -11 V. Black curve is the low field numerical fitting result based on Hikami-Larkin-Nagaoka (HLN) theory.

2.3.5. Gate Dependence of Weak Antilocalization

As shown in the inset of Figure 2-7 (a), the gate dependence of MC under low magnetic field was measured for the *in situ* Al passivated device. Through in-plane MC background subtraction, the low field MC ($\Delta\sigma(B) = \sigma(\theta = 90^\circ, B) - \sigma(0^\circ, B)$) conducted at 1.9 K was shown in Figure 2-7 (a), to exclude the 3D bulk WAL contribution, where θ is the angle between B field and the film plane. The $\Delta\sigma(B)$ vs. B curves are surprisingly identical for all different gate biases except below -9 V, even though there are more than 30% changes in the Hall carrier concentration n_H (See Figure 2-7 (c)). This can be attributed to the surface conduction significantly enhanced when the bulk carrier density is sufficient low (V_g < -9 V), *i.e.*, the Fermi level approaches the Dirac point.[70, 113]

The HLN equation (1-31) gives a perfect fit to all the MC curves with various gate biases at 1.9 K shown in Figure 2-7(a), where the phase coherence length l_ϕ and the

prefactor α are two fitting parameters.[93] The numerical fitted values α and l_ϕ as functions of gate voltages are plotted in Figure 2-7 (b), respectively. The phase coherence length l_ϕ of 58 nm and the prefactor α of 0.49 are obtained at -12 V and 1.9 K, indicating that there is only one surface contribution to the 2D WAL effect. This is in agreement with the recent studies on the WAL in Bi_2Se_3[70] and Bi_2Te_3[112]. The contribution to the WAL effect from the bottom surface seems negligible since the l_ϕ of the bottom surface is reduced possibly due to defeats caused by the lattice mismatch between Bi_2Se_3 and Si substrate.[70, 87, 112] One may also notice that the l_ϕ slightly decays and α deviates from 0.5 with increasing gate voltage, which is probably due to the fact that the 2D bulk carriers contribute more to the overall conductivity of the system, with increasing gate voltage. The estimated gate dependences of the surface states parameters obtained from both SdH oscillation and WAL at T = 1.9 K for the Al passivated device are summarized in Table 2.

Table 2. Estimated parameters of surface states from the SdH oscillations and WAL for the *in situ* Al passivated sample at T = 1.9 K. The cyclotron mass is obtained from $m_c = \frac{\hbar k_F}{V_F}$, while other parameters are calculated as shown in the text. (This also appears in one of my publications Ref. [86].)

V_g	f_{SdH}	N_{2D}	m_c	k_F	E_F	V_F	l_ϕ	α
(V)	**(T)**	**(10^{12}cm^{-2}**	**(m_0)**	**(Å^{-1})**	**(meV)**	**(10^5m/s)**	**(nm)**	

-12	98	2.37	0.170	0.055	133	3.7	57.7	0.49
-11	112	2.71	0.182	0.058	142	3.7	56.1	0.51
-10	135	3.26	0.199	0.064	157	3.7	55.8	0.52
-9	148	3.58	0.209	0.067	164	3.7	55.5	0.54

2.3.6. Temperature Dependence of Magnetoconductivity

Next, we investigate the temperature dependence of MC under a fixed gate voltage of -11 V. From the systematic trend of the MC curves in Figure 2-7(c), it is noticed that the MC cusp at low magnetic field is broadened as temperature increases, might due to bulk carriers are increasingly dominant at higher temperature; hence, the WAL effect arises from the nontrivial surface states is weakened. This trend can also be seen in the phase coherence length l_ϕ, which monotonically decreases from 56.1 nm to 31.9 nm as temperature increases from 1.9 K to 8 K. This similar behavior was also reported in literature.[112] The prefactor α changes from 0.51 to 0.67 as temperature increases, as presented in Figure 2-7(d). α larger than 0.5 at higher temperature is possibly due to the increasing bulk carrier contribution.

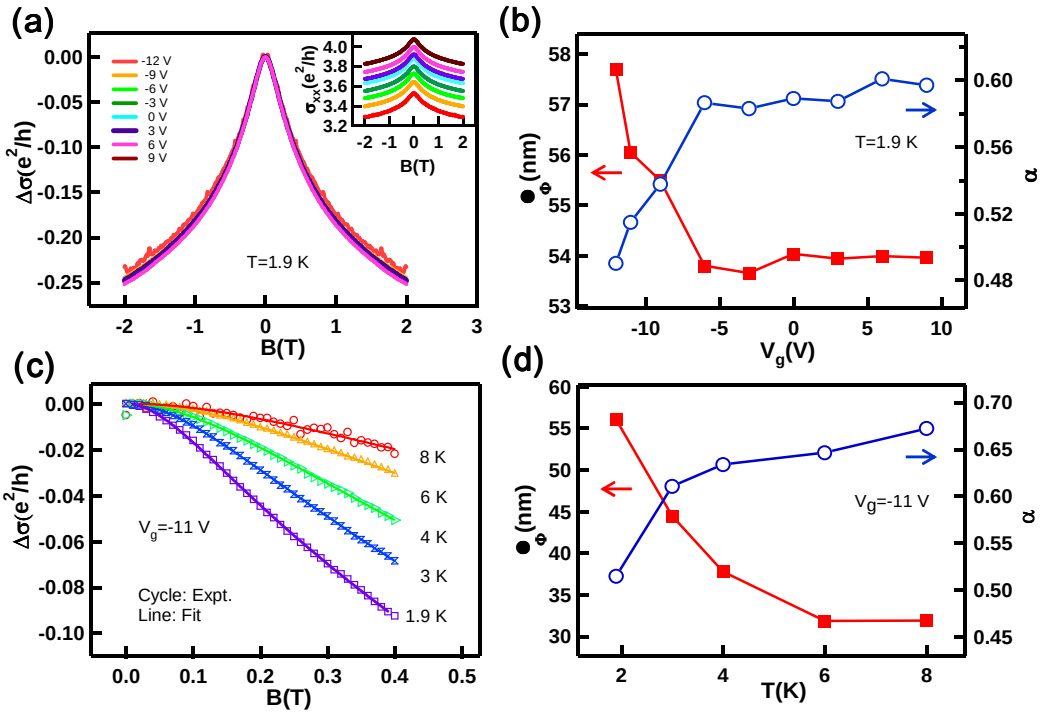

Figure 2-7. Gate voltage and temperature dependences of WAL for the *in-situ* Al passivated sample. (a) In-plane background subtracted magnetoconductivity ($\Delta\sigma(B)=\sigma(\theta=90^{\circ},B)-\sigma(0^{\circ},B)$) at 1.9 K under a set of gate biases, from -12 V to 9 V with 3 V a step, showing nearly identical $\Delta\sigma(B)$ vs. B curves for gate biases V_g > -9 V. Inset: conductivity vs. magnetic field, from V_g = -12 V (bottom curve) to V_g = 9 V (top curve). (b) Fitted phase coherence length l_ϕ (solid red squares) and coefficient α (open blue circles) from Eq. (1-31) as functions of gate voltage at 1.9 K. α larger than 0.5 at higher temperature is possibly due to the increasing bulk carrier contribution. (c) Background subtracted magnetoconductivity at a fixed voltage V_g = -11 V measured at different temperatures (open cycles). Lines are fitted curves by the HLN theory. (d) Fitted l_ϕ (solid red squares) and α (open blue circles) as a function of temperature at V_g = -11 V,

showing the WAL effect is weakened as bulk carriers make more contributions at higher temperatures. (This also appears in one of my publications Ref. 86.)

The fitted coefficient α agree very well with the theoretical value at 1.9 K under V_g = -12, -11 V, re-confirming the existence of surface states for the Al passivated sample. On the other hand, the device without Al passivation exhibits a large fitting deviation from the HLN theory at 1.9 K with various gate voltages applied. Therefore, it may further verify our claim that it is more challenging to probe and reveal the topological surface states in the un-passivated TI material.

2.4. Summary

In summary, we present the differences of transport results in MBE-grown Bi_2Se_3 samples with and without *in situ* Al passivation. Passivated 2D metallic topological surface states are better revealed with dual evidences from the SdH oscillation and WAL effects. Un-passivated samples exhibit higher carrier density, absence of quantum oscillations as well as large deviation from WAL, suggesting that Al passivation is an effective way to preserve the topological surface states from environmental degradation. Hence our observation provides an important step towards the realization of future nanoelectronics and

dissipationless spintronics devices, which may be able to take advantages of the exotic surface states in TIs.

Chapter 3

Competing Weak Localization and Weak Antilocalization in Ultrathin Topological Insulators

3.1. Motivation

Massless topological surface states have been experimentally identified and extensively studied in binary and ternary TI materials.[4, 38, 40, 44, 46, 51, 70, 78, 82-90] More recently, the exotic and interesting physics associated with the coupling between the top and bottom surface states in the two-dimensional (2D) limit of these 3D TIs has attracted new attention.[4, 66, 69, 114-116] However, only a few experiments have been carried out on ultrathin TI films, and most of them focus on angle-resolved photoemission spectroscopy[4] and STS[116]. On the contrary, magneto-transport measurement, as an important approach to establish the low-dimensional electronic characteristics, remains lacking.

In this chapter, we demonstrate the opening of an energy gap in the surface states due to the hybridization of top and bottom surfaces in the ultrathin $(Bi_xSb_{1-x})_2Te_3$ films with thicknesses below 6 quintuple layers (QLs). Thanks to the nearly bulk insulating state of $(Bi_xSb_{1-x})_2Te_3$ system,[77, 117] the surface Fermi level (E_F) can be electrically tuned through the surface bandgap and consequently the transport properties of intriguing gapped surface can be investigated. When E_F is located inside the surface gap of ultrathin samples, the overall unitary behaviors are revealed at high magnetic field, in contrast to the pure weak

antilocalization (WAL) signals obtained in thicker ones. More importantly, manipulated *via* electric gating, a competition between WAL and weak localization (WL) is strikingly revealed in ultrathin films at lower magnetic field due to the change of the Berry phase, presenting a unique way to study the surface states of the ultrathin TI with a gap opening at the Dirac point in the quantum diffusive regime.

3.2. Material Growth and Sample Preparation

3.2.1. MBE Growth of $(Bi_{0.57}Sb_{0.43})_2Te_3$.

High-quality single crystalline $(Bi_{0.57}Sb_{0.43})_2Te_3$ thin films were conducted in a PerkinElmer MBE system under an ultra-high vacuum environment; MBE is proven to be a powerful and reliable technique to produce ultrathin TI films with accurate thickness control to a few quintuple layers.[49, 66, 84] Intrinsic GaAs (111) wafers ($\rho > 10^6$ Ω·cm) were cleaned by a standard Radio Corporation of America (RCA) procedure before being transferred into the growth chamber. Then GaAs substrates were annealed in the chamber under Se-protective environment at ~580 ˚C to remove the native oxide on the surface. After removing the native oxides, the GaAs substrate has shown clear 2D pattern with a bright specular spot (Figure 3-1(a)), indicating the epi-ready surface for subsequent growth. During growth, Bi, Sb and Te cells were kept at 470, 395 and 320°C respectively, while GaAs (111) substrate was set at 200°C (growth temperature). Figure 3-1(b) shows a

large-scale atomic force microscope (AFM) image of an as-grown $(Bi_{0.57}Sb_{0.43})_2Te_3$ film with a thickness of 9 QL, exhibiting terraces over 500 nm in size. The surface consists of triangle-shaped terraces and steps, indicative of a hexagonal crystal structure inside (0001) planes.

In-situ growth dynamics are monitored by reflection high energy electron diffraction (RHEED) measurements. Digital images of the RHEED were captured using a KSA400 system made by K-space Associate, Inc. Growth rate can be estimated as 1 QL/min from the periodic RHEED oscillations which started from the first layer of the growth (Figure 3-1(c)).D-spacing of surface lattice change during growth after 1^{st} $(Bi_{0.57}Sb_{0.43})_2Te_3$ layer growth as indicated in Figure 3-1(d). 2 nm Aluminum (Al) was subsequently deposited *in-situ* at 20 ˚C to protect the epi-layer from unintentional doping induced by ambient environment.[50] Al film was later naturally oxidized to form Al_2O_3 after the sample was taken out of the chamber and exposed in air, which also further serves as a good seeding layer of the high-k dielectric oxide stack grown by the atomic layer deposition (ALD) process.

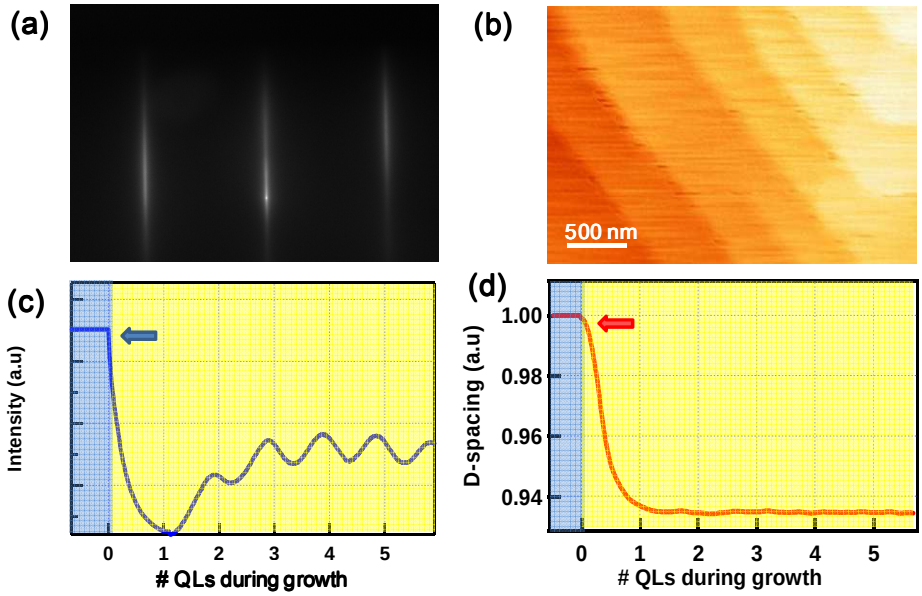

Figure 3-1. $(Bi_{0.57}Sb_{0.43})_2Te_3$ compound growth characterization. a, RHEED pattern along $[11\bar{2}0]$direction of an as-grown surface of $(Bi_{0.57}Sb_{0.43})_2Te_3$ with a thickness of 9 QLs. **b**, An AFM image of the TI thin film with terrace size exceeding 500 nm. **c**, RHEED oscillations of intensity of the specular beam. The oscillation period is found to be 60 s, corresponding to a growth rate of ~ 1 QL/min. **d**, D-spacing of surface lattice change during growth. The arrow indicates that the surface morphology has converted from GaAs to after 1^{st} $(Bi_{0.57}Sb_{0.43})_2Te_3$ layer growth.

3.2.2. Cross-section TEM, EDX and Device Structure.

To investigate the quality of the thin film, high-resolution scanning transmission electron microscope (STEM) experiments were performed on a FEI TITAN Cs corrected STEM operating at 200 kV. Figure 3-2(a) (left) shows a high angle annular dark field (HAADF) image of the single crystalline $(Bi_{0.53}Bi_{0.47})_2Te_3$ film and the GaAs substrate,

where the sharp interface without any amorphous layer is clearly revealed. The QLs of this ternary TI system is further manifested in the magnified TEM image (Figure 3-2(a), right), demonstrating the same tetradymite structure as their parent compounds of Bi_2Te_3 and Sb_2Te_3.[77] The thickness of each QL is estimated to be ~1.02 nm, as indicated by two parallel white lines. Additionally, the energy dispersive X-ray spectroscopy (EDX) was performed to examine the film composition. Prominent Bi, Sb and Te peaks are revealed in Figure 3-2(**b**). Quantitative analysis shows that the precise atomic ratio of Bi/Sb/Te is 1.35:1:3.4.

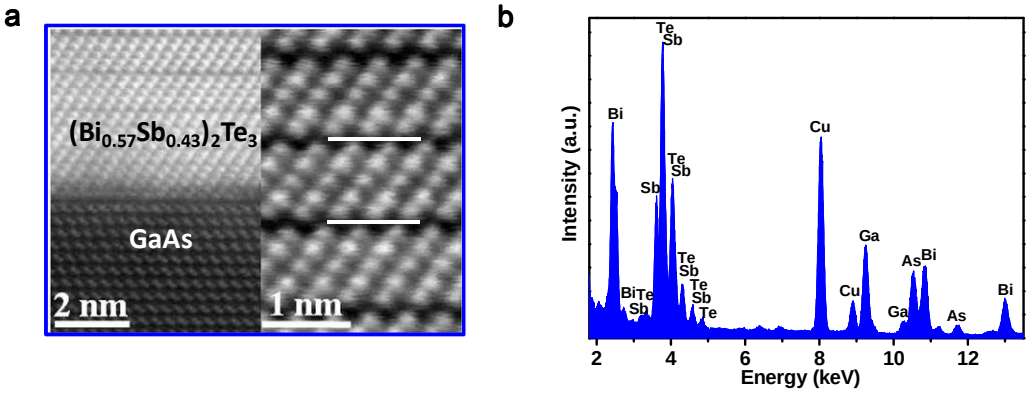

Figure 3-2. Cross-section TEM, EDX and device structure. a, Left: A high-resolution TEM picture for the $(Bi_{0.57}Sb_{0.43})_2Te_3$ film and GaAs (111)B substrate. An atomically sharp interface is also observed. Right: A magnified TEM image showing the quintuple structure with ~1.02 nm lattice spacing between (0003) planes. **b**, Energy dispersive X-ray spectroscopy of the film composition, which is mainly composed of Bi, Sb and Te.

3.2.3. Device Fabrication.

The MBE-grown $(Bi_{0.57}Sb_{0.43})_2Te_3$ thin film was first patterned into a micron-scale Hall bar geometry using conventional optical photolithography and a subsequent CHF_3 dry-etching of 15 s. Hall bar contacts were defined by photolithography and followed by *e*-beam evaporation of 10 nm chromium (Cr) and 100 nm gold (Au). A 25 nm-thick Al_2O_3 dielectric layer was conformally deposited by ALD at 250°C to serve as the high-k gate dielectric. Another step of photolithography was needed to open window, and dry etching was carried out to etch the Al_2O_3 in the contact area with subsequent dip in 5% diluted HF. Finally, the top-gate electrode and Hall channel contacts were defined and followed by metal deposition of Cr/Au (10 nm/100 nm).

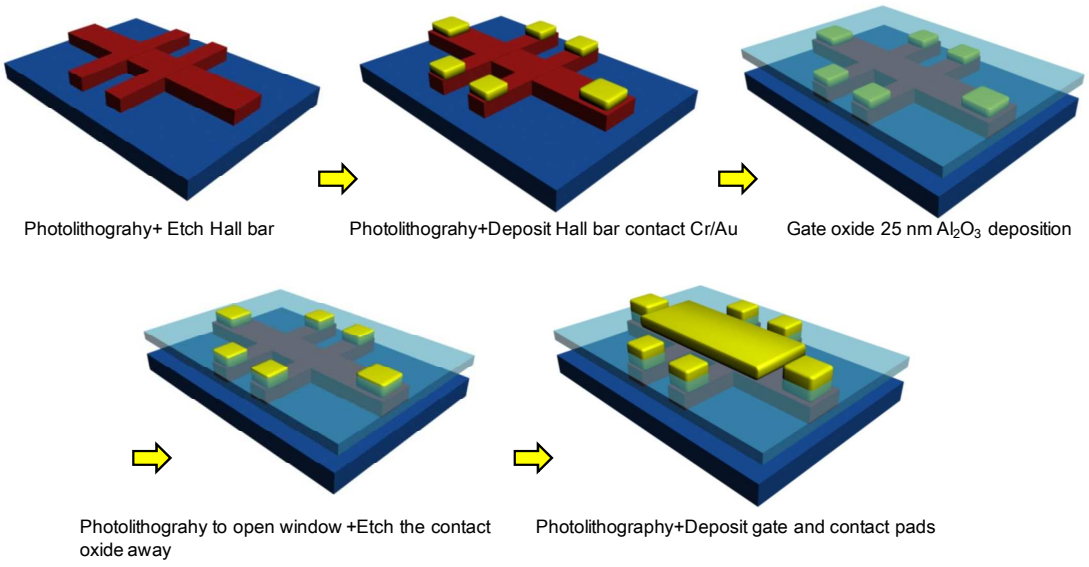

Figure 3-3. Fabrication processes of TI based high-*k* FET by photolithography.

3.2.4. Device Characterization Methods

High magnetic field and low temperature measurements were conducted at Tallahassee National High Magnetic Field Laboratory with the application of DC magnetic field up to ± 18 T. The temperature range is from 0.3 to 60 K. Standard four-probe measurements were carried out with an ac current sourced from a Keithley 6221. Multiple lock-in-amplifiers were used to measure the longitudinal and transverse resistance.

To explore the transport properties of this material, the device measurement setup is schematically shown in Figure 3-4(a). Figure 3-4(b) (left) shows an optical microscope image of the typical device structure. The diagonal two electrodes are top-gate electrodes, whereas the rest electrodes are connected to the Hall bar. A zoom-in view of the eight-terminal Hall bar (5 μm (shorter longitudinal length between two Hall terminals) or 15 μm (longer longitudinal length) × 5 μm (width)) is shown in the right panel.

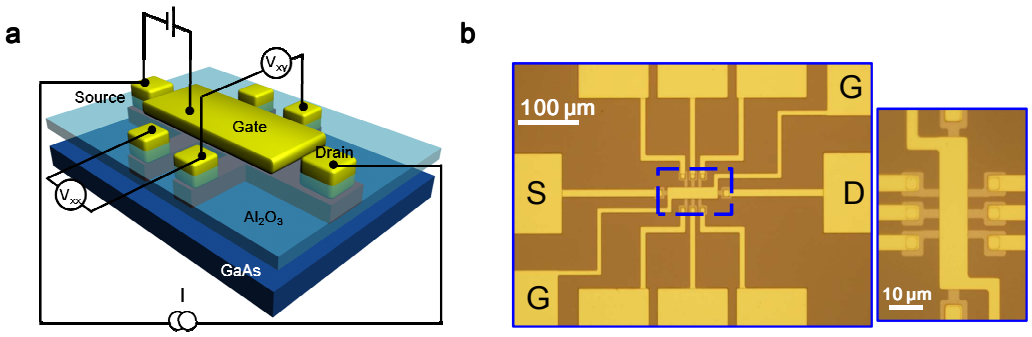

Figure 3-4. a, Schematic diagram of $(Bi_{0.57}Sb_{0.43})_2Te_3$ (red) on highly resistive GaAs (111) (dark blue) top-gate Hall bar device structure with measurement setup. The total thickness of Al_2O_3 (light blue) is ~25 nm. A standard four-point measurement was carried out with

constant AC current flow of 1μA. **b**, Left: An optical image of the device structure with 100 μm scale bar. Right: A zoom-in view of the Hall bar with the size of 5 μm (L) × 5 μm (W), with 10 μm scale bar. Note: the Hall bar channel cannot be clearly seen in the figure since it is underneath with top gate area.

3.3. Ambipolar Effect

3.3.1 Thickness Dependent $(Bi_{0.57}Sb_{0.43})_2Te_3$ Thin Films

A characteristic ambipolar field effect is observed in thin films with thickness ranging from 4 to 9 QL as displayed in Figures 3-5(a)-(f). By applying a top gate bias V_g, E_F can be effectively tuned across the surface Dirac point, and both the carrier type as well as the carrier density can be easily controlled. Remarkably, a giant gate modulation of ~1500% with a sharp peak resistance (R_{max}) of ~70 kΩ is observed in the ultrathin 4 QL film (Figures 3-5(a), upper panel). Compared with the gate modulations in the thicker samples shown in Figures 3-5(c)-(f) (upper panels), this high on/off ratio can be attributed to the extreme low density of states in the 4 QL sample as a result of surface gap opening. Furthermore, the Hall coefficient (R_H) (open squares) extracted from the Hall slope reverses its sign when R_{xx} approaches its maximum, corresponding to the lowest net carrier density achieved. Alternatively, the 2D carrier density $n_H = -1/(eR_H)$ (where e is the elementary charge) is calculated to further illustrate this ambipolar effect, as indicated in Figure 3-5(a)

(lower panel). Here, the unipolar conduction (only one type of dominant carrier) is manifested in the linear *p*-type ($V_g < -3$ V) and *n*-type region ($V_g > 5$ V); whereas in the ambipolar region (-3 V $< V_g < 5$ V), R_H crosses zero and n_H changes sign from *p* to *n*-type, suggesting the coexistence of two competing carriers (electron and hole).[76, 77]

For the 5 QL sample (Figure 3-5(b)), the resistance peak broadens and R_{max} decreases to ~14 kΩ due to a smaller gap opening. Moreover, $R(V_g)$ shows a much reduced modulation signature of only ~250%. As the film thickness further increases (Figures 3-5(c)-(f), upper panel), $R(V_g)$ exhibits a much weaker tunability and R_{max} decreases its magnitude, indicating the disappearance of the surface hybridized gap and an increased bulk denisties. In particular, R_{max} of the 9 QL film is suppressed by one order of magnitude relative to that of the 4 QL film, accompanied by an increase of minimum carrier density n_{min} from ~ 8×10^{11} cm^{-2} (4 QL) to 1×10^{13} cm^{-2} (9 QL). Remarkably, a sudden rise of n_{min} at thickness $t > 7$ QL may be attributed to the appearance of bulk conduction, which could no longer be fully depleted by gating due to the relatively short depletion width in TI materials.[66, 77]

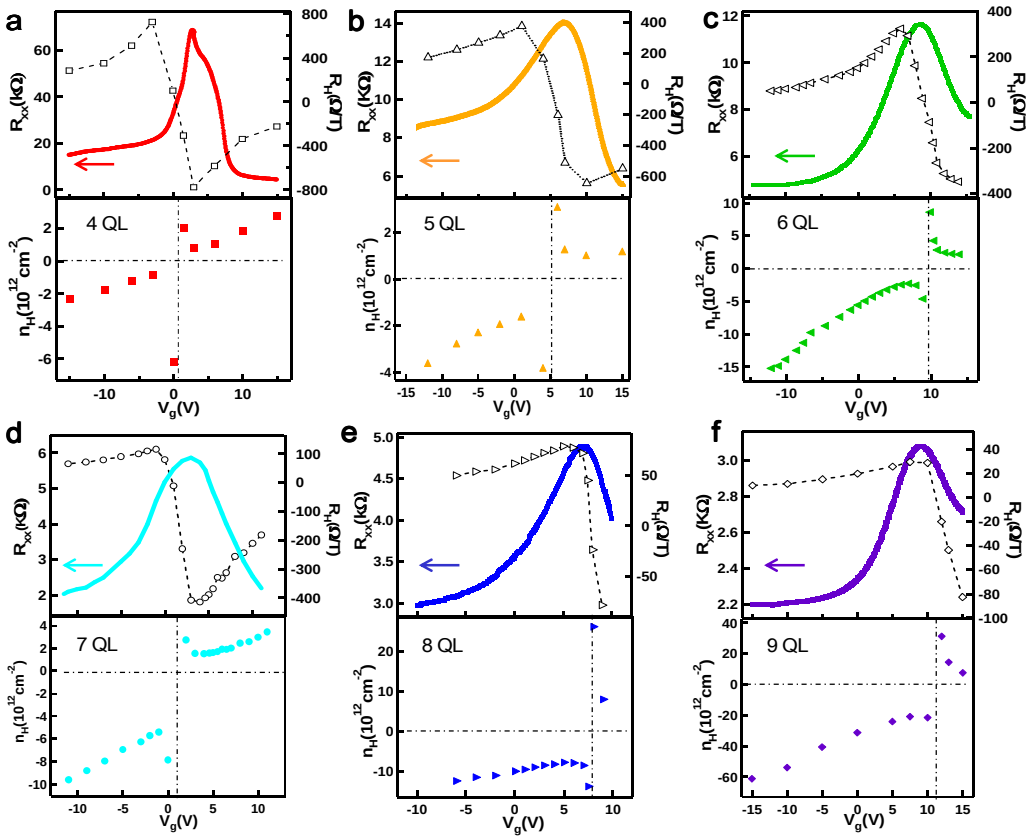

Figure 3-5. Transport properties of thickness dependent $(Bi_{0.57}Sb_{0.43})_2Te_3$ at 0.3 K. a-f, Upper: Longitudinal resistance R_{xx} (lines) and Hall coefficient R_H (open symbols) as functions of gate voltage V_g corresponding to different thicknesses from 4 to 9 QLs. The largest peak of R_{xx} vs. V_g and giant gate modulation of ~1500% are observed in the 4 QL sample. As film thickness increases, the peak broadens and R_{max} decreases greatly. Each R_H is extracted from the Hall traces at ±4 T for a certain V_g. Lower: Unipolar conduction (only one type of dominant carrier) is manifested in the linear regions of n_H vs. V_g. While in the ambipolar region, n_H starts to diverge at the bias (changing sign from p to n), where the net carrier density is significantly reduced, indicating the ambipolar behavior. In short, the ambipolar effect presented above reveals a giant gate modulation and an ultralow carrier

density in 4 QL film when E_F is tuned through the hybridization induced surface gap. (This also appears in one of my publications Ref. 53.)

3.3.2. Peak Resistance and Carrier Density vs. Thickness

The thickness dependent maximum resistant R_{max} obtained from Figure 3-5 presents an abrupt change at 4 QL, as indicated in Figure 3-6. At 4 QL, R_{max} reaches ~ 70 kΩ, owing to the surface bandgap opening (~180 meV) at the Dirac point. As film thickness increases, R_{max} decreases monotonically as the surface gap vanishing and continuously increased bulk contribution.

At the same time, the 2D carrier concentration n_H remains low value < 2.5×10^{12} cm^{-2} for thickness below 8 QL, where bulk contribution is greatly suppressed. However, it is noted that the n_H suddenly jumps to 7.5×10^{12} cm^{-2} at $t \geq 8$ QL, above which gate may not effectively modulate the charge carrier density of the entire film any more. Hence, in order to suppress bulk contribution and achieve low density TI sample, film thickness should be kept below ~8 QL. This is consistent with the literature that by solving Poisson equation, the first order estimated maximum depletion width D is ~ 11 nm, beyond which a portion of carriers cannot be fully depleted by gating effect.[77]

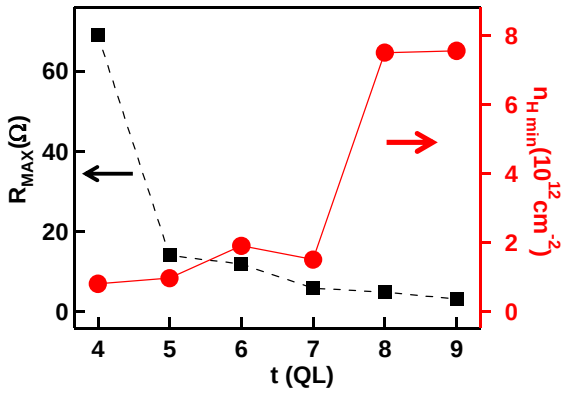

Figure 3-6. R_{max} and n_H as functions of film thickness. The largest R_{max} is obtained at 4 QL and it rapidly decreases as thickness increases. n_H remains < 2.5×10^{12} cm^{-2} for 4 to 7 QLs, and suddenly increases to 7.5×10^{12} cm^{-2} at $t \geq 8$ QL.

3.4. Quantum Oscillations from Top and Bottom Surface States

At 0.3 K, quantum oscillations can also be seen in the 10 QL $(Bi_{0.57}Sb_{0.43})_2Te_3$ sample. To emphasize the gate dependent oscillations and to eliminate the MR background, we have used the second derivative of R_{xx} (d^2R_{xx}/dB^2) in Figure 3-7. The first thing to notice is that there are gate voltage dependent peaks as accentuated by the white dashed lines. These peaks (valleys) originate from the formation of Landau levels of Dirac fermions on the top surface states; the gate dependent shift is due to the decreasing of the top surface carrier density as the Fermi level approaches the Dirac point. At the same time, there are other gate independent peaks at high magnetic field, as indicated by the black dashed lines. These peaks are attributed to those from the Landau levels of the bottom surface states. The strong

screening effect arises from the high dielectric constant of TI materials prevents the bottom surface states from being affected by the gate bias[118], resulting in little or almost no change of carrier density and correspondingly constant oscillation frequencies. It is also interesting to notice that the top and bottom surface states have different oscillation frequencies (and carrier densities). This may be explained by the different band bending at the interface [118]. These two independent quantum oscillation frequencies arising from the top and bottom surface states have been very rare to be seen in the literature[118, 119], because it requires very high quality for both two surface states.[54]

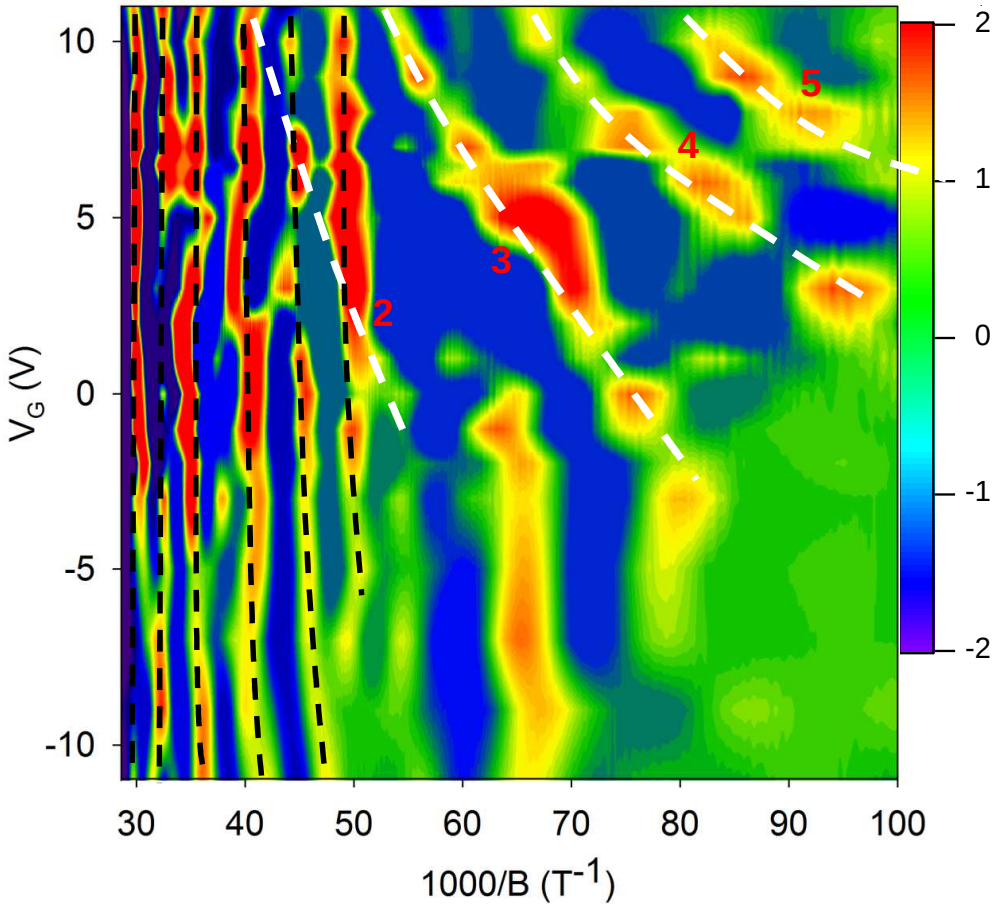

Figure 3-7. Shubinkov-de Haas oscillations from the top and bottom surface states. d^2R_{xx}/dB^2 as functions of $1/B$ and V_g. Both gate dependent and independent peaks are observed. The features which change with V_g originate from the formation of the Landau levels of Dirac fermions on the top surface states (white dashed lines, the Landau levels 2 to 5 are marked). The V_g-independent features come from the Landau levels of the bottom surface states (black dashed lines). The color bar presents the value of d^2R_{xx}/dB^2 for each gate voltage and magnetic field. (This also appears in one of my publications Ref. 54.)

The Landau fan diagram for various gate voltage values is plotted in Figure 3-8(a), in which the 1/B values corresponding to the maximum in Figure 3-8(a) is plotted as a function of Landau level index n[83, 103, 120, 121]. Please refer session 2.3.3 for Landau fan diagram. The solid symbols represent the data for the top surface states, demonstrating a systematic shift depending on gate biases. The open symbols represent those for the bottom surface states, which show no dependence on gate bias. Figure 3-8(b) displays the top surface carrier density n as a function of Fermi energy E_F. The n_{top} is effectively tuned from 1.61×10^{12} down to 1.07×10^{12} cm^{-2} by sweeping the gate voltage from 11 V to 2 V. A quadratic relationship of $E_F \propto n^{1/2}$ can be observed, as indicated by the red line, confirming the linear E-K relationship of the Dirac-cone.

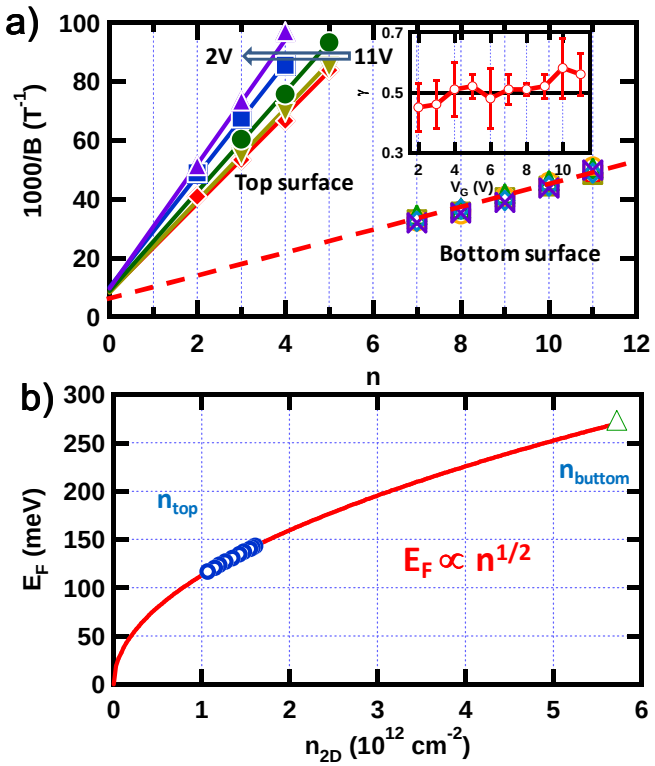

Figure 3-8. (a) Landau fan diagram of the peaks. The peaks of magnetoresistance of the top surface states (solid symbols) show systematic changes depending on the gate voltages, while those of the bottom surface states are almost constant. Inset: The intercept γ as a function of gate voltages. The black line indicates γ = 0.5. (b) The carrier density of the top (circles) and bottom (triangle) surface states as a function of Fermi energy E_F extracted from the corresponding SdH oscillations for various gate voltages. A quadratic relationship is shown. (This also appears in one of my publications Ref. 54.)

3.5. Quantum Interference in Ultrathin Topological Insulator Films

3.5.1 Crossover from WAL to WL in 4 QL by Gating Effect

Next, we present the striking influence of the surface gap on the magneto-transport properties of the ultrathin TI films in the quantum diffusive region. Figure 3-9 displays the dramatic contrast of normalized magnetoconductivity (MC) $\Delta\sigma(B)=\sigma_{xx}(B)-\sigma_{xx}(0)$ between thick (6, 7, 9, 10 QL) and thin (4 and 5 QL) films at their V_{dirac} (the V_{g} corresponding to $R_{\max}$) as a function of perpendicular external magnetic field applied at T = 0.3 K. On one hand, for $t \geq 6$ QL, all the MC curves display a sharp negative cusp characteristic of WAL, consistent with the nontrivial topology of the surface states carrying a Berry phase of π.[69, 70, 84, 87, 112] The data can be analyzed *via* the HLN formula (also see Eq. 1-31)[93]

$$\Delta\sigma=\frac{\alpha e^2}{2\pi^2\hbar}\left[\ln\left(\frac{\hbar}{4eBl_\phi^2}\right)-\psi\left(\frac{1}{2}+\frac{\hbar}{4eBl_\phi^2}\right)\right] \tag{3-1}$$

As indicated in the inset of Figure 3-9, the fitting results yield $|\alpha|\approx 1$ for the thicker films, suggesting the coexistence of two fully decoupled channels in this system, contributing |α| = 1/2 each.[111, 122] The slight increase of |α| as the film gets thicker, is possibly owing to the additional bulk channel partially coupled with the surfaces.[111, 122] On the other hand, consistent with Ref. [66], when the film thickness is reduced to the 2D limit (4 and 5 QLs), the MC curves at their V_{dirac} change drastically from the sharp WAL behavior to a unitary behavior ($\alpha \approx 0$), suggesting the opening of a surface gap in 2D limit TIs. It

should be emphasized that for the gap-opened 2D limit of TIs Eq. (3-1) is no longer valid and additional correction to MC can acquire both WAL and WL contributions, which, for the case of weak surface and bulk coupling, acquires a modified HLN equation given in Eq. (3-2), to be discussed later. We further note that in contrast to the study in Ref. [66] that was limited to a fixed Fermi level, our current approach of controlling the Fermi level *via* gating provides further confirmation and a more complete picture of the combined WAL and WL contributions to MC for massive Dirac fermions, which we elaborate below.

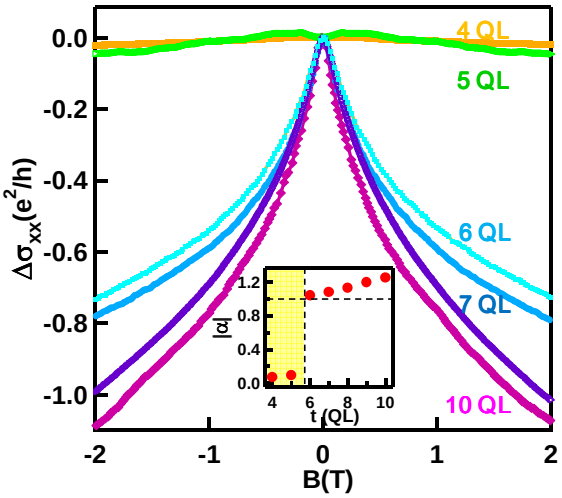

Figure 3-9. Quantum interference competition in 4 QL $(Bi_{0.57}Sb_{0.43})_2Te_3$ at 0.3 K. Normalized magnetoconductance (MC) $\Delta\sigma(B)=\sigma_{xx}(B)-\sigma_{xx}(0)$ for 4 ~ 10 QL measured at their V_{dirac}. The conductivity is significantly suppressed when the thickness is reduced to 4 and 5 QLs. Inset: the thickness dependent α fitted from one component HLN theory shows an abrupt change as t < 6 QL, which suggests the opening of a surface gap in 2D limit TIs. (This also appears in one of my publications Ref. 53.)

The gate voltage dependence of resistance in 4 QL sample is shown again here in Figure 3-10 (same as Figure 3-5a). The band structure for the gapped surface state with respect to their E_F, is schematically shown in the inset in three different gate voltage regimes. The dots on the curve represent the specific gate biases applied for each corresponding magneto resistance measurements in Figure 3-11(a). Strikingly, at low magnetic field (B < 0.4 T), we observe an intriguing electric field controlled quantum interferences competition between WAL and WL effect as shown in Figure 3-11(a) for the 4 QL film and Figure 3-12(a) for the 5 QL one, both of which exhibit great differences from thicker ones. For the 4 QL film, in the ambipolar region ($-6\ \text{V} \leq V_g \leq 3\ \text{V}$), when E_F is inside/close to the surface gap, the MC first exhibits a WL-like behavior at low field (B < 0.2 T), and then bends over to WAL at higher field. We also note that at $V_g = 3$ V, where R_{max} is obtained, the weakest magnetic field dependence of MC (unitary-like behavior) is achieved, implying the absence of interference because of an insulating state. However, as E_F is moved deep into the unipolar regions ($V_g = 10$ and -10 V), the WL signal vanishes completely, and the MC curves recover the WAL with negative cusps, similar to pure Dirac-like surface states.

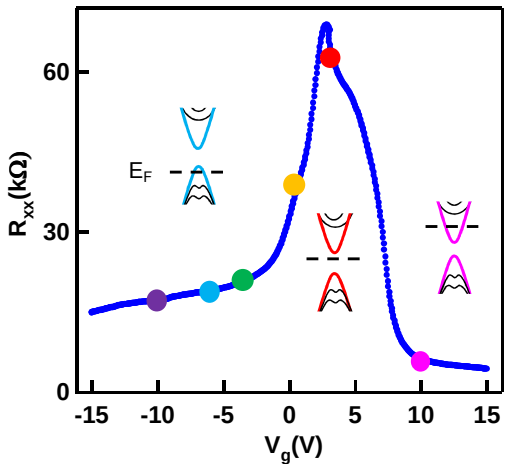

Figure 3-10. Gate voltage dependence of resistance of the 4 QL sample. The dots on the curve represent the specific gate biases applied for each corresponding magnetoresistance measurements in Figure 3-11(a). The insets show schematics of E_F positions relative to the gapped surface states. (This also appears in one of my publications Ref. 53.)

In particular, we extract the relative strength of WAL and WL contributions as a function of gate voltage by fitting the measured MC curves to the two-component HLN theory:[111]

$$\Delta\sigma(B) = \sum_{i=0,1} \frac{\alpha_i e^2}{\pi h}\left[\psi\left(\frac{l_B^2}{l_{\phi i}^2}+\frac{1}{2}\right)-\ln\left(\frac{l_B^2}{l_{\phi i}^2}\right)\right] \qquad (3\text{-}2)$$

Here, the coefficients α_0 and α_1 in Eq. (3-2) stand for the weights of WAL and WL contributions from the two surfaces (top + bottom), respectively, and $l_{\phi i}$ is the corresponding phase coherence length. The WAL dominated MC ideally has prefactors $\alpha_0 = -1/2$ and $\alpha_1 = 0$, while the WL dominated MC leads to $\alpha_0 = 0$ and $\alpha_1 = 1/2$. Equation (2-2) gives excellent fit to all the gate voltage dependent MC curves in Figure 3-11(a) as shown

by solid lines. Figure 3-11(b) summarizes the evolution of α_0 and α_1 of the 4 QL sample as functions of applied gate voltage. When V_g moves positively or negatively away from V_{Dirac}, $|\alpha_0|$ increases while α_1 decrease, indicating the WL contribution is greatly suppressed whereas the WAL contribution becomes more pronounced. Specifically, at V_g = 10 V, as E_F lies high into the upper branch of surface state where a π Berry phase is recovered, WAL dominates the MC curve with negligible WL component (α_0 = –0.582 ± 0.015, and α_1 =0.0412 ± 0.025), and a similar scenario can also be seen in the other end of the bias (V_g = –10 V). On the contrary, WL contribution is maximized while WAL is minimized (α_0 = –0.383 ± 0.039 and α_1 = 0.365 ± 0.095) as V_g approaches V_{Dirac} = 3 V.

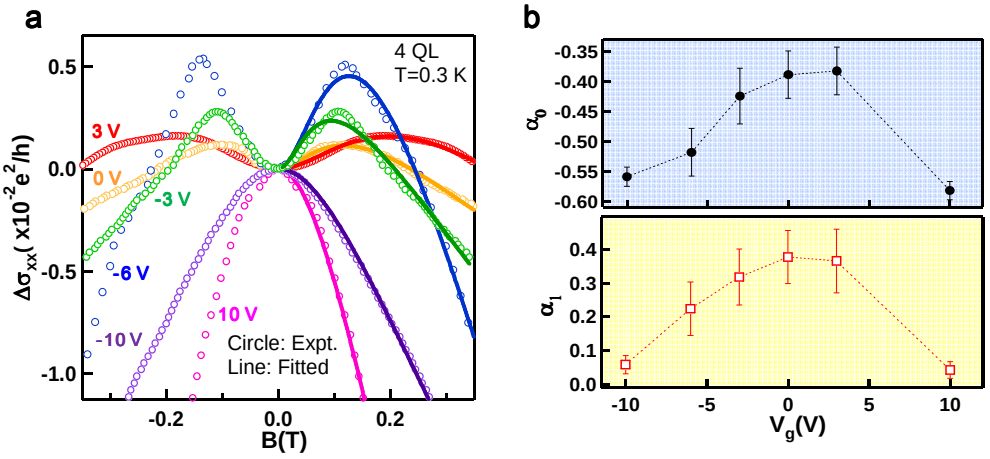

Figure 3-11. a, Evolution of low field MC as a function of gate voltage for the 4 QL film. In the ambipolar region (V_g = –6, –3, 0, 3 V), the MC curves first show WL-like behavior at low field (B < 0.2 T), and then bend over to WAL at higher field. The MC recovers their WAL characteristics again when E_F is high or low enough to be in the unipolar regions (V_g = –10 and 10 V). **b,** The evolution of WAL coefficient α_0 (upper

panel) and WL coefficient α_1 (lower panel) as functions of gate voltage obtained by fitting using Eq. (3-2). The two competing WAL and WL behaviors coexist and compete with each other in the ambipolar region. The WAL contribution $|\alpha_0|$ enhances when V_g moves from the ambipolar to the unipolar region, whereas the $|\alpha_1|$ representing WL contribution monotonically decreases. (This also appears in one of my publications Ref. 53.)

The observation of WL in the ultrathin films is surprising. In fact, for an ideal TI film without bulk conduction in the diffusive regime (mean free path $\ll$ system size ~ phase coherent length), WAL is obtained in a numerical simulation.[123, 124] It has been suggested that a WL contribution can be obtained from the bulk if it is weakly doped and decoupled from the surface.[122] However, our result does not seem to be consistent with a bulk contribution because the bulk contribution is greatly suppressed in ultrathin films when E_F is near the surface bandgap. Alternatively, this observed behavior can be understood in terms of Berry phase (ϕ) acquired by electrons over closed trajectories, which is dependent on gate voltage for gapped Dirac fermions, in the form of $\phi = \pi\left(1 - \frac{\Delta}{2E_F}\right)$, where Δ is the surface gap and E_F is the measured Fermi level position relative to the Dirac point.[94] When E_F is close to the Dirac point, ϕ approaches 0 and therefore resulting in the dominance of WL. Tuning E_F from V_{Dirac} deeper into the surface band takes ϕ from 0 to π, which one might expect to correspond with the transition from WL to WAL.[94, 111, 125]

3.5.2. Quantum Interferences Competition in a 5 QL Sample

Moreover, we also observe the electric field controlled WAL/WL quantum interference competition in the 5 QL film as manifested in Figure 3-12(a). We further remark that the WAL behaviors reported in the literature for samples $t \leq 5$ QL is consistent with the condition $E_F^{\,2} >> \Delta^2$, suggesting that the chemical potential of those samples typically lies far outside the surface state.[66, 69] On the contrary, for thicker films ($\geq$ 6 QL), WAL clearly manifests itself in various gate voltages, consistent with the absence of surface gap, as shown in Figure 3-13.

The inset of Figure 3-12(b) presents the gate voltage dependence of resistance, in which we roughly define the ambipolar region (-12 V < V_g < 4 V) and *n*-type region ($V_g \geq$ 4 V). In Figure 3-12(a), in the ambipolar region, the MC curves firstly display WL-like behavior at low field, and then bend over to WAL at higher field, similarly as 4 QL case. The WAL characteristics prevail at the unipolar region, possibly because now E_F moves into the upper surface state branch. The evolution of both α_0 (upper panel) and α_1 (lower panel) fitted by Eq. 3-2 as a function of gate voltage is present in Figure 3-12(b). The WAL contribution $|\alpha_0|$ enhances when V_g moves from the ambipolar to the unipolar region, whereas the $|\alpha_1|$ representing WL contribution monotonically decreases.

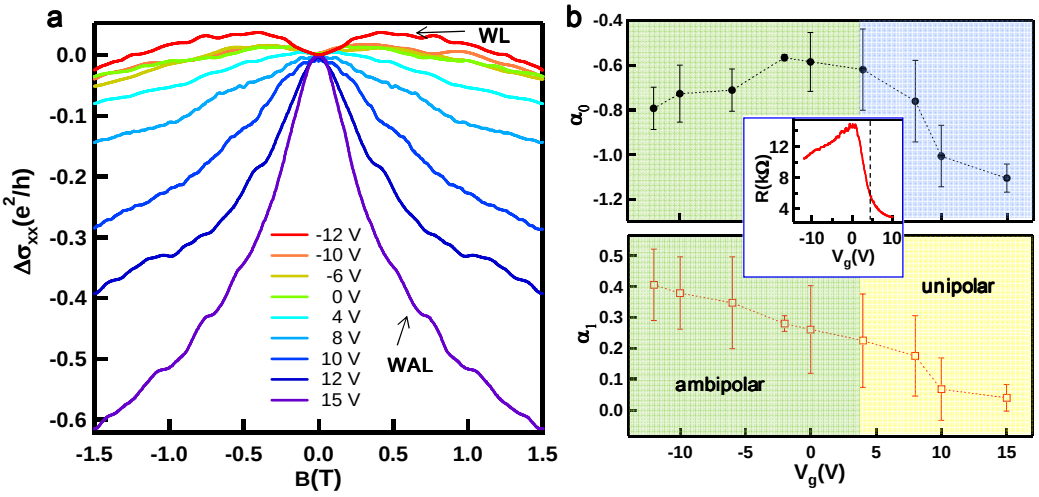

Figure 3-12. Quantum interference competition in 5 QL $(Bi_{0.57}Sb_{0.43})_2Te_3$ at 0.3 K. a, Evolution of normalized low field MC as a function of gate voltage. In the ambipolar region (-12 V < V_g < 4 V), where E_F is close to the surface band gap, the MC curves firstly show WL-like behavior at low magnetic field, and then bend over to WAL at higher field. The WAL characteristics prevail in the unipolar region ($V_g \geq$ 4 V) when E_F moves into the surface state upper branch. **b**, The evolution of α_0 (upper panel) and α_1 (lower panel) fitted by Eq. 2 as functions of gate voltage. The WAL contribution $|\alpha_0|$ enhances when V_g moves from the ambipolar into the unipolar region, whereas WL contribution $|\alpha_1|$ decreases. Inset: gate voltage dependence of resistance for the 5 QL sample. (This also appears in one of my publications Ref. 53.)

3.5.3. Theoretical Calculation of Two Parameters α_0 and α_1.

In the two-component HLN thoery, the two parameters α_0 and α_1 present the weight of WAL and WL, respectively, and both of which depend on the position of E_F respective to the surface Dirac point. According to the Ref. [94, 111], α_0 and α_1 are derived as following forms. Here we obtained these simplified formula by assuming that the magnetic scattering length $l_m \to \infty$, since magnetic impurity is absent in our samples.

$$\alpha_0 = -\frac{a^4 b^4}{(a^4+b^4)(a^4+b^4-a^2b^2)} \quad \alpha_1 = \frac{(a^4+b^4)(a^2-b^2)^2}{2(a^4+b^4-a^2b^2)^2}$$

where $a \equiv \cos\frac{\Theta}{2}$, $b \equiv \sin\frac{\Theta}{2}$. Here, Θ is defined as $\cos\Theta = \frac{\Delta/2 - Bk_F^2}{E_F - Dk_F^2}$, where Δ is the surface band gap and E_F is measured in reference to the Dirac point. *B* and *D* are the parameters in the model Hamiltonian in Ref. [111], in which B represents the 2nd order correction to the gap size at non-zero momentum and D corresponds to the bulk kinetic energy dispersion coefficient. At the Dirac point, the relation can be simplified as $\cos\Theta \approx \frac{\Delta/2}{E_F}$. The corresponding Berry phase as shown in Ref. 7 is given by $\phi = \pi(1-\cos(\Theta))$.

As discussed in Ref. 8, the quantum interference behavior (WAL/WL) is mainly controlled by $\cos\Theta$. In the limit when E_F is far into the upper surface state (conduction) branch or the lower (valence) branch, *i.e.*, $\cos\Theta \to 0$, corresponding to $\alpha_0 = -1/2$, $\alpha_1 = 0$, one has only WAL with a negative MC cusp. However, as E_F is moved toward the surface gap controlled by applying the gate voltage, $\cos\Theta$ increases and consequently drive the

system first into the unitary regime; and eventually reach the WL regime with a positive MC cusp when $\cos\Theta \to 1$ ($\alpha_0 = 0$, $\alpha_1 = 1/2$).

3.5.4. Weak Antilocalization in 6 ~10 QLs Thin Films

Figures 3-13(a)-(d) demonstrate detailed gated voltage dependence of the normalized magnetoconductivity (MC) $\Delta\sigma(B) = \sigma_{xx}(B) - \sigma_{xx}(0)$ of 6, 7, 9, 10 QLs films at T = 0.3 K. All samples present clear weak antilocalization (WAL) signature, in which $\Delta\sigma(B)$ has a cusp-like maximum at B = 0. The 6 QL sample shows more dramatic gate dependence of $\Delta\sigma(B)$ than thicker ones owing to its lower carrier density.[70] One component Hikami-Larkin-Nagaoka theory (Eq. 1 in the main text) is applied to fit the prefactor α and phase coherent length l_ϕ. $|\alpha|$ in Figures 3-13 (e)-(h) show their maxima ($|\alpha|$~1) as E_F is tuned close to the Dirac point, implying the topological properties is clearly revealed at charge neutrality point. As E_F moves far away, it corresponds to the case of coherently coupled bulk and surface electron states since more bulk carriers are accumulated, hence $|\alpha|$ and l_ϕ reduces. Furthermore, as film thickness increases, the gate-dependent $|\alpha|$ increases from 0.57~1.04 for 6 QL to 1.01~1.19 for 10 QL, suggesting increased channel separation with the thickness of the films.

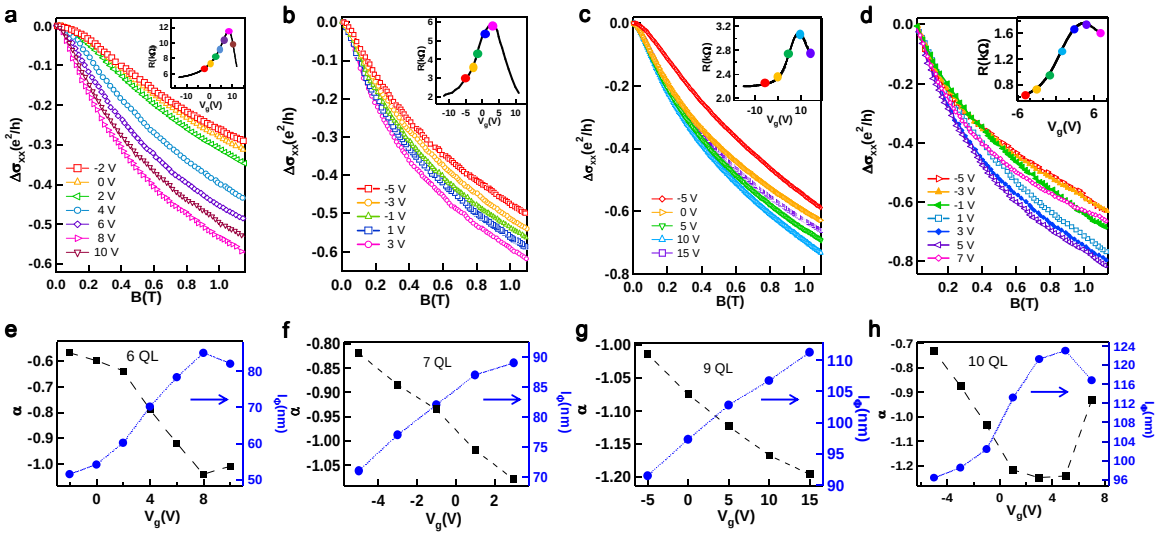

Figure 3-13. Gate voltage dependence of α and l_ϕ in 6, 7, 9, 10 QLs samples at 0.3 K. a-d, The gate voltage dependence of normalized magnetoconductance of 6 QL(**a**), 7 QL(**b**), 9 QL(**c**), 10 QL (**b**). Inset: The gate voltage dependence of resistance for the corresponding thin film, where the solid circles present the corresponding gate voltages applied. **e-h,** Fitted phase coherence length l_ϕ (squares) and coefficient α (circles) from one component HLN theory (Eq. (1)) as functions of gate voltage for 6 QL(**a**), 7 QL(**b**), 9 QL(**c**), 10 QL(**b**).

3.6. Scanning Tunneling Spectroscopy Measurements

To determine the Dirac energy and surface bandgap opening in the ultra-thin 4 QL $(Bi_{0.57}Sb_{0.43})_2Te_3$ sample, low-temperature spatially resolved STS under high vacuum was carried out. The sample with 2 nm passivated Al_2O_3 was first etched in 5% HF solution for

10 seconds and immediatly transferred to the cryogenic probe of a homemade STM sample holder in argon environment. The STM is then pumped down to 8×10^{-5} Torr vacuum and then cooled down to 77K.

A detailed survey of the tunneling conductance spectra was acquired over a 10 nm × 10 nm area with 64× 64 pixels at 77 K. The Dirac energy (E_D) estimated from the mid-gap energy is E_D = –0.17 ± 0.07 eV throughout the areas of our investigation as shown by the histogram in Figure 3-14(a). Figure 3-14(b) presents a typical tunneling conductance (dI/dV) spectrum that manifests a surface hybridization bandgap ~180 meV in the 4 QL sample.

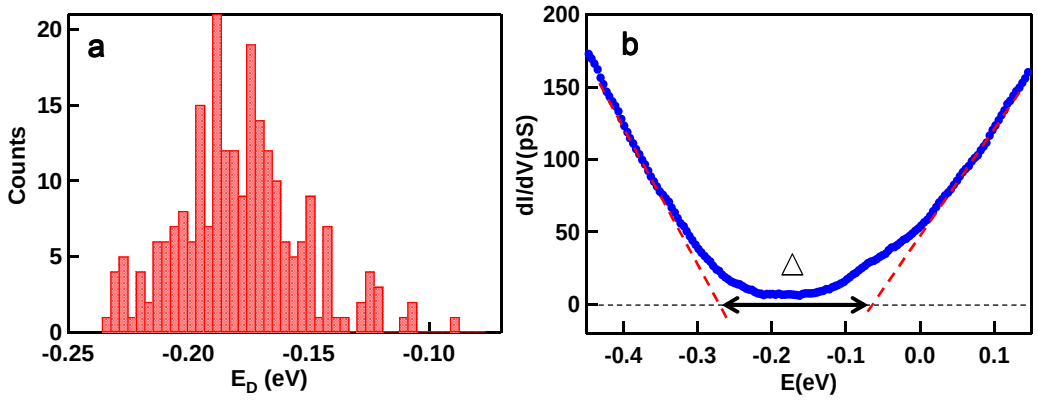

Figure 3-14. Scanning tunneling spectroscopy of 4 QL $(Bi_{0.57}Sb_{0.43})_2Te_3$。a, The histogram of Dirac energy (E_D) estimated from the mid-gap energy to be $E_D = -0.17 \pm 0.07$ eV throughout the areas of our investigation, and the relative large variation is probably due to the surface terraces. **b**, A typical tunneling conductance (dI/dV) spectrum taken at 77 K, showing a surface bandgap opening in the 4 QL thin film. Here the

small tunneling conductance in the gap region may be attributed to the thermal smearing effect. (This also appears in one of my publications Ref. 53.)

3.7. Summary

In conclusion, we have demonstrated the ambipolar field effect of electrically surface manipulation in high quality and low carrier density MBE-grown $(Bi_{0.57}Sb_{0.43})_2Te_3$ thin films. Due to the hybridization-induced surface gap, the MC of 4 and 5 QL ultrathin films are greatly suppressed, exhibiting overall unitary-like behavior when E_F is located inside the surface bandgap. By tuning E_F position relative to the gap, the striking crossover between WL and WAL is observed in nonmagnetic ultrathin films at low field region, a characteristic feature of quantum interferences competition. Hence, our observation is of great importance for further understanding the role of surface state hybridization in ultrathin TIs, and these hybridized surface states can be promising for the realization of edge states for demonstrating the quantum spin Hall effect and dissipationless spintronics in 3D TIs.

Chapter 4

Topological Insulator/YIG Heterostructure

4.1. Magnetic Topological Insulator

Breaking TRS introduces axion electrodynamics physics manifested by a gapped Dirac spectrum as well as the topological magnetoelectric effect, which gives rise to the direct coupling of electric and magnetic fields. Various exotic phenomena, such as the quantum anomalous Hall effect,[28, 30, 32] giant magneto-optical Kerr effect,[126] chiral mode conduction channels,[6, 127] and magnetic monopole effect[128] have been experimentally discovered or theoretically predicted. As an effective way to break the TRS in TIs, substantial efforts have been made to introduce ferromagnetic order in a TI by doping 3*d* transition metal elements such as Cr, Fe, and Mn.[56, 57, 61, 62, 129, 130]

It has been proposed that in magnetically doped TI systems, ferromagnetic moments can be developed through two major mechanisms: the van Vleck mechanism from the TI's valence electrons[131] and the RKKY interaction between neighboring magnetic impurities, which is mediated by itinerant carriers[132, 133]. In the former case, due to the large spin susceptibility of the valence electrons in the TI materials, the magnetic impurities in the bulk can be directly coupled through local valence electrons without assistance from itinerant electrons, and thus exhibit a prominent ferromagnetic moment. Consequently, this

"bulk ferromagnetism" is independent of the carrier density[131]. On the other hand, neighboring magnetic ions can also be coupled together through the mediation of conduction carriers and is coined as the carrier-mediated RKKY interaction[134-136].

From the gate-modulated magneto-transport measurements, we have demonstrated the presence of both the hole-mediated RKKY coupling and the carrier-independent bulk van Vleck magnetism in magnetic TI systems. Importantly, it is possible to separate and operate each interaction mode through the alteration of Cr doping levels and electrical gating. By controlling the Cr doping levels during MBE growth, we prepare $Cr_y(Bi_xSb_x)_2Te_3$ samples with same $x = (1-y/2)/2$, film thickness d = 6 QL, but different Cr doping levels.

Figures 4-1(a)-(d) summarize the electric-field-controlled AHE results of additional four samples with Cr% = 5%, 10%, 15%, and 20%, respectively. [56] Although increasing the Cr doping concentration introduces more impurities (*i.e.*, the 2D Hall density n_{2D} varies from 1.2×10^{12} cm^{-2} to 2.2×10^{13} cm^{-2} at 1.9 K), such range is acceptable to maintain the Fermi level inside the bulk band gap and effective gate modulations in all these four samples are obtained (Figures 4-1(e)-(h))[137-140]. From the extracted $H_c - V_g$ curves, in the moderate doping region (5%, 10%, and 15%), the Cr-doped $(Bi_{0.5}Sb_{0.5})_2Te_3$ thin films all exhibit hole-mediated RKKY magneto-electric response in the sense that the anomalous Hall resistance R_{xy} loop reduces its coercivity field (H_c) when the holes are depleted. When

the samples are further gated deep into the *n*-type region (i.e. E_F>50 meV above the Dirac point), H_c gradually saturates at finite values of 150 Oe (Cr=5%), 375 Oe (Cr=10%), and 685 Oe (Cr=15%), 1000 Oe (Cr=20%) respectively. For the chromium doping concentration of 20% in Figure 4-1(d), even though the gate modulation reaches 50% and the surface Fermi level has been effectively tuned by 50 meV (Inset of Figure 4-1(h)), the hysteresis window (H_c) remains a constant of 1000 Oe and does not show any change with respective to the gate bias any more (Figure 4-1(h)).[56]

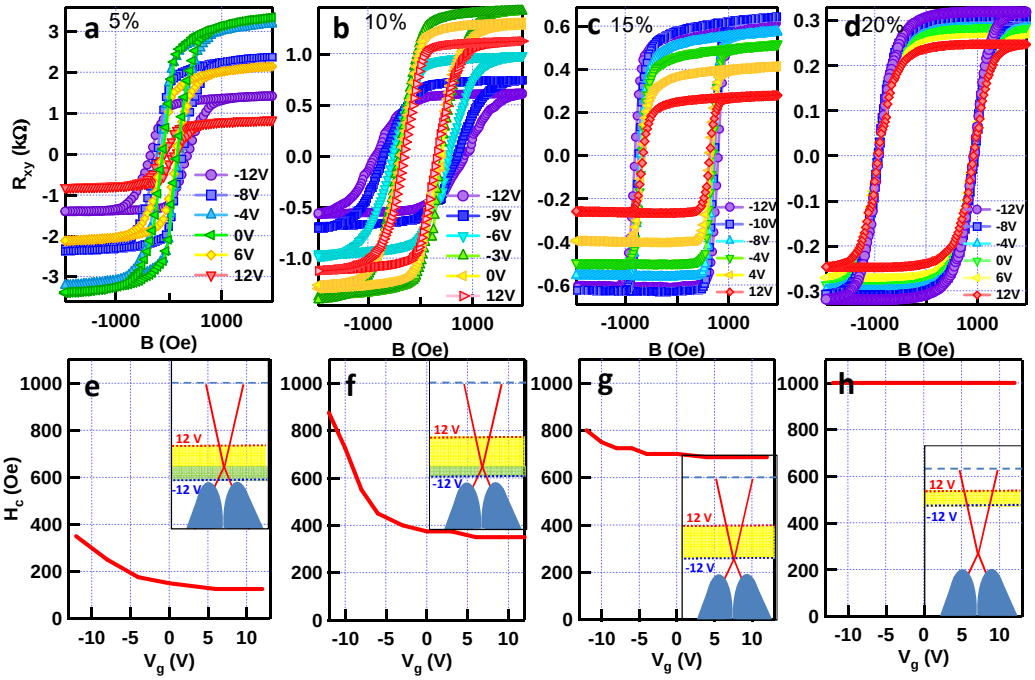

Figure 4-1. Gate-dependent AHE resutls for 6 QL Cr-doped $(Bi_{1-x}Sb_x)_2Te_3$ thin films with different Cr doping concentrations (a) Cr = 5%, **(b)** Cr = 10%, **(c)** Cr = 15%, and **(d)** Cr = 20%. **(e)-(h)** Gate-modulated coercivity field changes in these four samples. Inset:

Indication of Fermi level position controlled by the top-gate voltages ranging from -12V to 12V. (This also appears in one of my publications Ref. 56)

Even though the ferromagnetism of TIs can be well controlled by the electric field, to date, the Curie temperature (T_c) of magnetically TIs has only reached ~35 K, which is significantly lower than required for practical room temperature applications.[55, 62, 63, 130] Figure 4-2 shows the T_c as a function of Cr doping concentration, in which T_c monotonically increases with Cr concentration. However, on one hand, too much Cr doping concentration may drive the TI system from topological nontrivial to trivial state; on the other hand, it also greatly affects the TI film crystallinity, and leads to Cr segregation. Hence, the realization of magnetic order in TIs at higher temperatures remains one of the major challenges in the field.

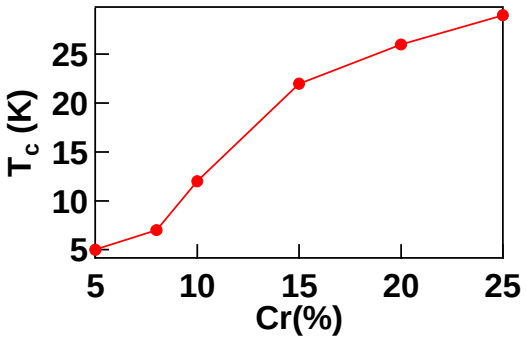

Figure 4-2. The Curie temperature of Cr doped TI sample increases monotonically as Cr doping concentration increases. However, the Cr doping concentration cannot exceed 30% to avoid segregation or tuning the TI material into topological trivial.

4.2. Magnetic Proximity Effect

One promising approach to achieve the breaking of TRS in TI at higher temperature is to utilize a magnetic proximity effect at the interface of the TI and a topologically trivial magnetic material. While theoretical work suggests the legitimacy of this approach,[141, 142] limited experimental work has been reported in the literature.[57, 143-145] Recent efforts on EuS/TI heterostructure strongly suggest the presence of magnetic proximity effects at the interface. However, the effect is limited to low temperatures (< 20 K) due to the low Curie temperature of EuS layer.[144, 145] In this chapter, high-temperature (~130 K) proximity-induced magnetic order at the interface between Bi_2Se_3 and a high T_c ferrimagnetic insulator (FMI), yttrium iron garnet (YIG, $Y_3Fe_5O_{12}$) is demonstrated. This is a significant step towards realizing TI-based spintronics at room temperature. By a combination of temperature dependent magneto-transport measurements and magneto-optical Kerr effect (MOKE) magnetometry, we provide direct evidence of the correlation between the magnetization of the YIG layer and the transport properties of Bi_2Se_3. A butterfly shape or a square shape hysteretic magnetoresistance (MR) is observed for the external field perpendicular or parallel to the sample plane, respectively, which is correlated with the magnetization reversal of the YIG. Furthermore, the MOKE data suggest that a magnetic order develops in the TI at the interface with its spin presumed to be anti

parallel to the magnetization of the YIG up to at least 130 K. Consistent with numerical simulations, while the YIG substrate shows in-plane anisotropy at room temperature, a canting of magnetization toward out-of-plane direction is clearly observed at lower temperatures by Polar MOKE, most likely due to magnetocrystalline anisotropy. The magnetic configuration of YIG is expected to be useful to control the TRS of Bi_2Se_3 surface states, due to the coupling of magnetic order between the YIG and the Bi_2Se_3 at the interface.

4.2.1. Material Growth and Characterization

The YIG was a 50 nm-thick single crystal film grown epitaxially by pulsed-laser deposition on a paramagnetic Gallium Gadolinium Garnet (GGG) (111) substrate at 650 °C. YIG is a well-known ferromagnetic insulator (FMI) with T_c well above the room temperature (T_c ~ 550 K) and has been extensively studied as a prototype magnetic insulator for spin waves and magnonic physics including spin-Seebeck and spin-Hall effects.[146-149]

Before pulsed laser deposition of YIG films, stoichiometric YIG targets were prepared by mixing Y_2O_3 and iron oxide, ball milling, calcination and sintering at 1400 °C. 50 nm-thick YIG films were pulsed-laser deposited on 10mm x 10 mm Gallium Gadolinium Garnet (GGG) (111) substrates (Supplier: MTI Crystals Inc.) under 5 mTorr oxygen pressure (3 μTorr base pressure) using a KrF Coherent excimer laser with 400 mJ pulses at

2 Hz pulse rate at 650°C with 18,000 laser shots. After growth, the chamber was cooled in oxygen ambient. Low deposition rate (< 1nm/min) and similar lattice parameters of YIG and GGG (mismatch < 0.2%) allow epitaxial and low surface-roughness (< 0.3 nm rms) growth of YIG films on substrates.[150]

Atomic force microscopy showed that the YIG layer had a surface root mean square roughness less than 0.3 nm over the scanned area of $1\ \mu\text{m} \times 1\ \mu\text{m}$, as shown in Figure 4-3(a). X-ray diffraction, Figure 4-3(b), showed YIG with a (111) orientation,[151] and no other phases were observed. Figure 4-3(c) displays the room temperature magnetic hysteresis loops measured by a vibrating sample magnetometer (VSM), showing the YIG films are magnetically soft and isotropic in the film plane. An in-plane saturation moment (M_S) of 142 emu/cm^3 and coercivity less than 5 Oe were measured at room temperature.

To form a TI/FMI heterostructure, 8 quintuple layers (QLs) of single crystal Bi_2Se_3 were grown on the YIG/GGG substrate in a PerkinElmer molecular beam epitaxy (MBE) system under an ultra-high vacuum environment.[50, 53, 69] High-purity Bi (99.9999%) was evaporated from conventional effusion cells at 470 ℃, while Se (99.99%)was formed from a cracker cell from SVTA at 240℃, and the YIG/GGG (111) substrate was kept at 200℃ during the growth. The pseudomorphic growth of Bi_2Se_3 was monitored by real-time reflection high energy electron diffraction (RHEED). A 2 nm Al was *in-situ* evaporated to immediately after the growth of TI film in MBE chamber to protect the film for oxidation

and environmental doping.[50, 98] For comparison with the Bi_2Se_3/YIG sample, 8 QLs of Bi_2Se_3 films were also prepared on highly resistive Si (111) using the same technique.

Figure 4-3(d) shows the high angle annular dark field (HAADF) images of YIG/GGG and Bi_2Se_3/YIG interfaces, acquired by a Fischione HAADF detector. The atomically sharp interface indicated by the dashed line in the left panel of Figure 4-3(d) demonstrates the high-quality epitaxial growth of YIG on the GGG substrate. The right panel shows magnified quintuple layers of Bi_2Se_3 grown on YIG, in which the sharp interface between the Bi_2Se_3 and YIG is indicated by the red dashed line. Inter-diffusion of materials at the interface is not expected due to the high stability of YIG and the large difference in the growth temperatures.

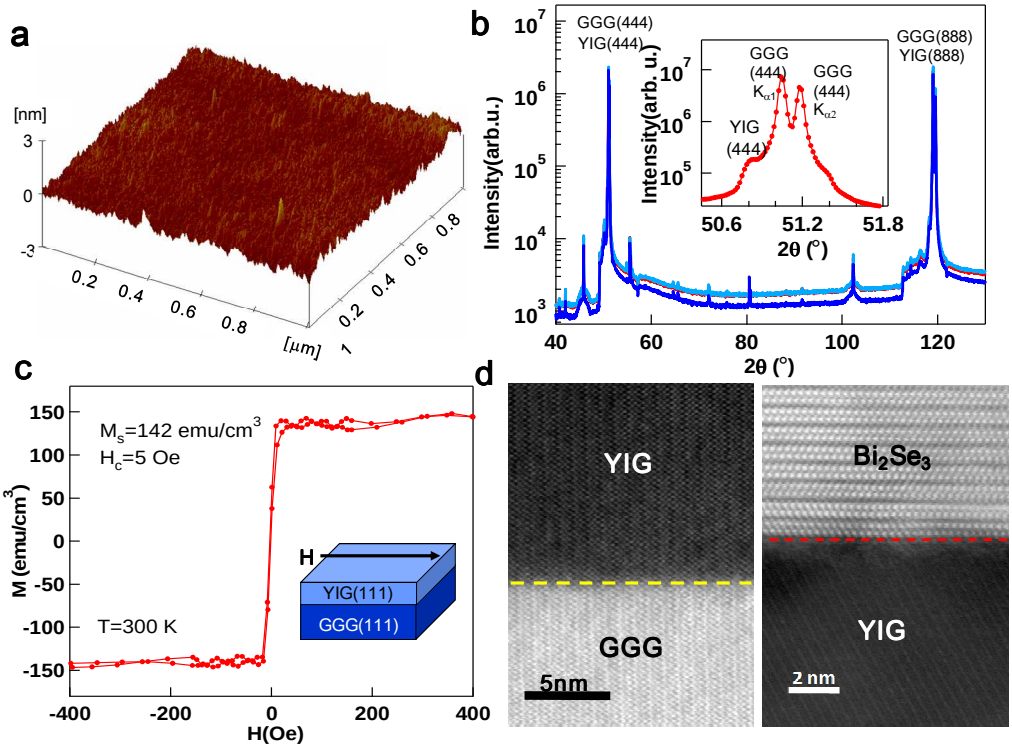

Figure 4-3. AFM, XRD, VSM characterizations of YIG/GGG and STEM of Bi_2Se_3/YIG/GGG. a, A typical AFM image of 50 nm YIG thin film grown on GGG (111) substrate. The YIG layers have a surface rms roughness less than 0.3 nm over the scanned areas of 1 μm× 1 μm. **b,** XRD spectrum of YIG grown on GGG in ω-2θ scans between 2θ = 40° to 130°. The peaks of the film and substrate were aligned in most cases because of epitaxial growth. Inset: a spectrum with an expanded angle scale, which indicates that the YIG film has a (111) orientation. **c,** Magnetic hysteresis loop for 50 nm in-plane magnetized YIG measured by VSM at 300 K. The in-plane saturation moment is 142 emu/cm^3 and the coercivity is less than 5 Oe. **d,** A typical STEM-HAADF image of Bi_2Se_3/YIG/GGG heterostructure, showing atomically sharp interfaces of YIG/GGG (yellow dashed lines, left panel) and Bi_2Se_3/YIG (red dashed lines, right panel). (This also appears in one of my publications Ref. 59.)

The Bi_2Se_3/YIG/GGG interface and crystalline structure were characterized by high-resolution STEM and EDX mapping experiments, carried out on a FEI Probe Cs corrected Titan operating at 200 kV. The high angle annular dark field (HAADF) images were acquired by a Fischione HAADF detector and the EDX maps were acquired by ChemiSTEM Technology with four windowless SDD detectors. The typical STEM-HAADF image of Bi_2Se_3/YIG grown on GGG is shown in Figure 4-4(a). Specifically, the colored distribution maps of each individual element are shown in Figures

4-4(b)-(h). All the elements display a distinct distribution pattern: Bi, Se locate at the top of the map; Y and Fe locates at the middle; Gd and Ga locate at the bottom; O locates at the middle and bottom parts of the map. The distribution of every element is uniform and there is no inter diffusion between two layers.

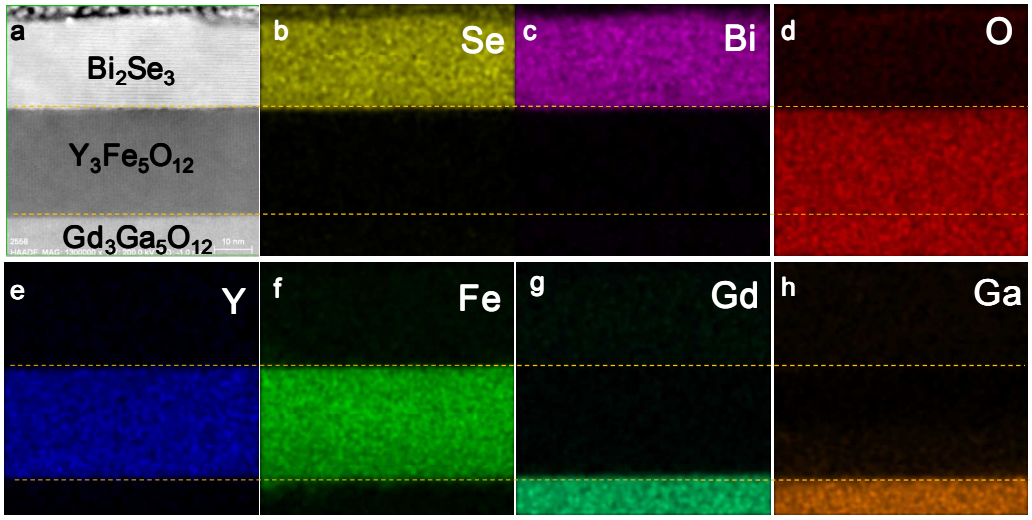

Figure 4-4. a, STEM-HAADF image of Bi_2Se_3/YIG grown on GGG. **b-h**, EDX maps of individual element Bi **(b)**, Se **(c)**, O **(d**), Y **(e**), Fe **(f)**, Gd **(g)** and Ga **(h)**, corresponding to the area of **(a)**. The distribution of every element is uniform and there is no inter diffusion between two layers.

Quantitative maps (QMaps) showing the atomic concentration of elements based on the quantification result of each pixel, indicating there is no intermixing at the interface as shown in Figure 4-5. [152] Multiple linescans have been acquired to verify the interface.

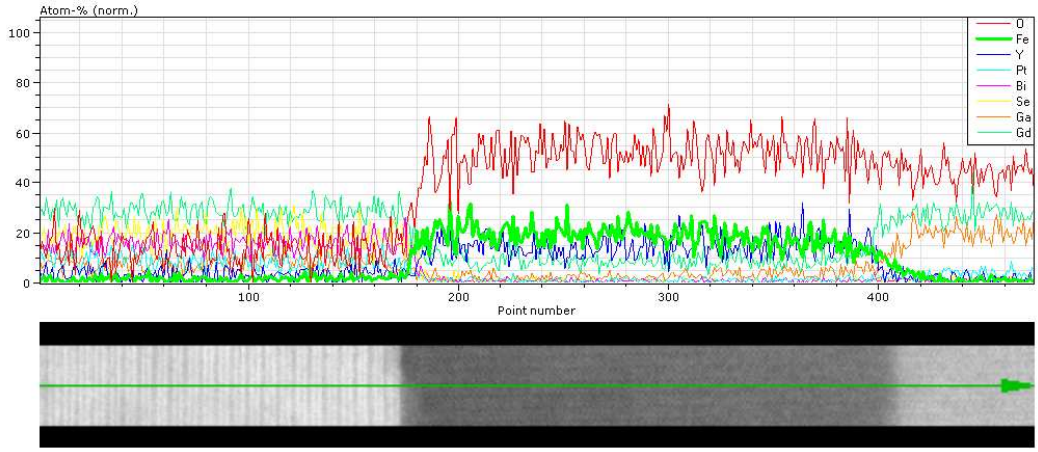

Figure 4-5. Atomic concentration of elements based on the quantification result of each pixel obtained from the EDX maps, indicating there is no intermixing at the interface.

4.3. Transport Measurement of TI/YIG Heterostructure

4.3.1. Temperature Dependence of Resistance and Carrier Density

To investigate the magnetic response of Bi_2Se_3/YIG heterostructure, the samples were patterned into standard Hall bar devices with 10 μm length and 10 μm width. Four-probe magneto-transport measurements were conducted in a PPMS.

Figure 4-6(a) provides temperature dependence of longitudinal resistance in linear and logarithmic (inset) scales of the Bi_2Se_3/YIG sample. The channel resistance initially decreases with the temperature, showing a typical metallic behavior in the temperature range of 50~300 K,[103, 153-155] in which the phonon scattering dominates (Figure 4-6(a)).

When the temperature drops below 50 K, the resistance experiences an increase, primarily due to the carrier freeze-out effect similar to those observed in lightly-doped Bi_2Se_3, similar to the low temperature region R-T behavior of Bi_2Se_3/Si shown in session 2.3.2.[155] We have attempted to extract the activation energy E_a in the temperature range of 2~50 K, where a nearly linear relation exists for $R \sim e^{E_a/k_BT}$ (Figure 4-6(a) inset, logarithmic scale). It is noted that our fitting result yields only a small activation energy less than 1 meV, which cannot be simply explained by the impurity levels in Bi_2Se_3. Instead, at this temperature range the surface conduction can be enhanced compared to that at higher temperatures, thus becoming a non-negligible component. Hall carrier densities n_H are extracted from $n_H = (R_H e)^{-1}$,where R_H is the Hall slope, e is the electron charge (see Session 2.3.2). In Figure 4-6(b), the carrier density reduces as temperature decreases in the temperature range of 2 ~ 100 K, resulting in the dominance of surface transport at low temperature. The carrier density of the Bi_2Se_3/YIG sample was ~8.2×10^{12} cm^{-2} at 2 K, comparable to the density of ~7×10^{12} cm^{-2} in the Bi_2Se_3/Si sample, indicating the similar sample quality.

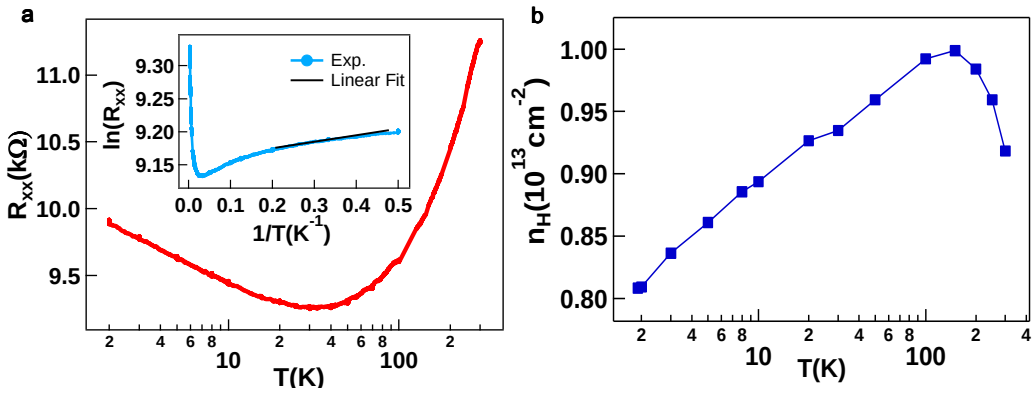

Figure 4-6. a, Temperature dependence of longitudinal resistance in linear and logarithmic (inset) scales of Bi_2Se_3/YIG sample. **b**, Hall carrier densities as a function of temperature, extracted from the Hall traces at ±4 T at each temperature point. This indicates at T < 6 K, the surface conduction is predominating.

4.3.2. Magnetoresistance of Bi_2Se_3/YIG

Figure 4-7(a) presents the longitudinal MR measurements of a non-magnetic control sample, Bi_2Se_3/Si. With an out-of-plane magnetic field, the MR exhibited weak anti-localization (WAL) behavior with a sharp cusp at the low-field region. With *H* (magnetic field) applied in the plane, however, the MR cusp feature disappeared completely. Instead, the MR showed a parabolic H^2 dependence, which results from the Lorentz deflection of carriers.[112] These are characteristic transport features expected in a non-magnetic TI, which have been reported previously for high quality TI thin films.[69, 70, 77, 112, 156]

In sharp contrast to the non-hysteretic MR of Bi_2Se_3/Si, the longitudinal MR of Bi_2Se_3/YIG showed hysteresis loops in the low field region distorting the WAL and parabolic MR backgrounds, with the application of perpendicular and in-plane field, respectively (Figures 4-7(b)-(c)). In Figure 4-7(b), the hysteresis loop shows a butterfly shape with two separate minima of MR, at $H_{min} = \pm 90$ Oe, most prominent at 2 K. The

magnetic feature in the MR of the TI indicates the presence of the proximity effect at the interface. As the temperature increased, the loop was gradually obscured by the background MR signal and could not be clearly resolved above 25 K (See Figure 4-8). The reduction of the hysteretic signal is attributed to the increasing transport contribution of the bulk Bi_2Se_3 channel at higher temperature. This indicates the interfacial origin of the hysteretic loop presumably with contribution of the topological surface states. On the other hand, the H_{min} of each hysteresis loop showed a weak temperature dependence, to be discussed in detail later, implying that the magnetic property may survive to higher temperatures, due to the high T_c of the YIG.

With an in-plane magnetic field, however, the MR hysteresis loops were square shaped with two sharp steps within each sweep (see Figure 4-7(c)). For instance, sweeping from negative to positive field, a sharp increase in MR appeared at $H_r = -1.45$ kOe following by a sharp drop at $H_f = 1.84$ kOe, as indicated by the arrows. H_r and H_f did not vary much as the temperature increased, which can be attributed to the modest temperature dependence of YIG magnetization within this temperature range. The comparison between the temperature dependence of the two MR geometries (Figures 4-7(b)-(c)) suggests that while their hysteretic MR shared a common origin in the proximity effect, the switching process of the YIG differed for different applied magnetic field directions. Moreover, we have performed in-plane rotation magnetic field measurement at H=4 kOe, in which the MR results of Bi_2Se_3/YIG exhibit an anisotropic MR (AMR) behavior as shown in Figure

4-7(d). The AMR ratio of Bi_2Se_3/YIG is measured at ~0.2% while the control sample (Bi_2Se_3/Si) does not exhibit any AMR as expected. It is important to note that the ~1% amplitude of the hysteretic MR (Figure 4-7 (b)-(c)) is much larger than AMR ratio of 0.2%, which indicates that the AMR is not a dominant mechanism in the hysteretic behavior. Nevertheless, both MR and AMR strongly suggest the presence of magnetic order in the TI induced by the magnetic substrate.

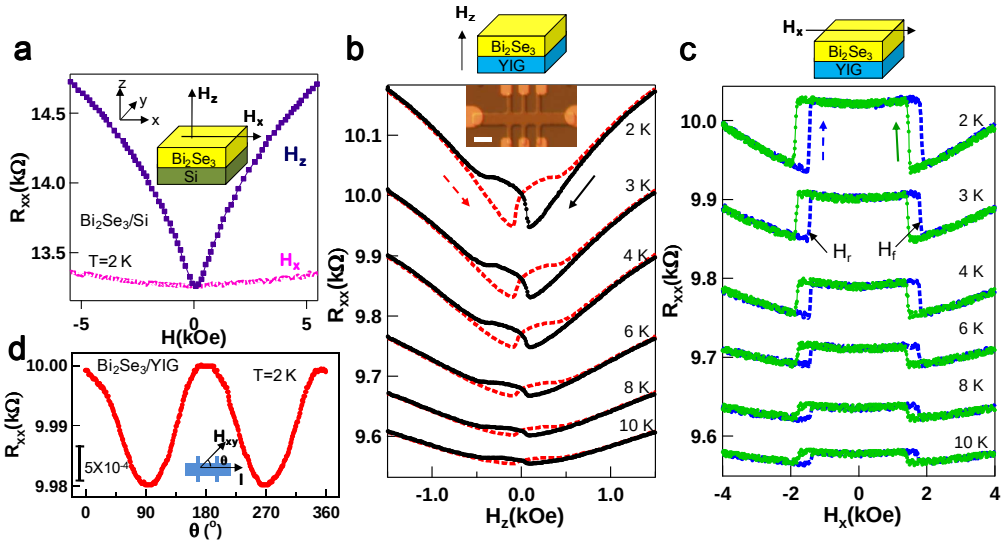

Figure 4-7. Magnetoresistances (MR) of Bi_2Se_3/Si (control sample) and Bi_2Se_3/YIG with out-of-plane and in-plane magnetic field applied. a, The non-hysteretic WAL behavior is obtained with out-of-plane field applied in Bi_2Se_3/Si. The parabolic MR curve is observed with in-plane field applied for Bi_2Se_3/YIG. **b**, Temperature dependent MR with an out-of-plane field applied. The hysteretic feature associated with the magnetic property of TI bottom surface disappears above 25 K, as the Bi_2Se_3 bulk component starts to dominate at higher temperature. Inset: An optical image of a Hall bar device structure with a 10 μm

scale bar. **c**, Temperature dependent MR with in-plane field applied. Similarly, due to the increasing bulk conduction contribution, the square shaped feature cannot be observed above 25 K. **d**, Anisotropic mangnetoresistance in Bi_2Se_3/YIG sample at H=4 kOe , with AMR ratio ~0.2%. (This also appears in one of my publications Ref. 59.)

In order to clearly investigate the temperature dependence of the hysteretic magnetoresistance (MR) in Bi_2Se_3/YIG, the detailed analysis is performed as shown in Figure 4-8. The MR ratio used to characterize the hysteretic behavior in MR, is defined as $(R_{max}-R_s)/R_{max}\times 100\%$, where R_{max} and R_s are obtained from ΔMR after background subtraction. Here, R_{max} presents the maximum resistance in ΔMR, while R_s is the resistance at saturation region. For both out-of-plane and in-plane case, the MR ratio reduces as temperature increases as shown in the red curve in Figure. 4-8(a)-(b), suggesting that the diminishing of the hysteretic signal at T > 25 K is presumably due to the dominant transport through the bulk Bi_2Se_3 channel. Moreover, the temperature dependences of H_s for both out-of-plane and in-plane field are consistent with the MOKE results. With out-of-plane magnetic field (Figure 4-8(a) blue curve), H_s increases as temperature arises; while with in-plane magnetic field (Figure 4-8(b)), H_s decreases as temperature increases.

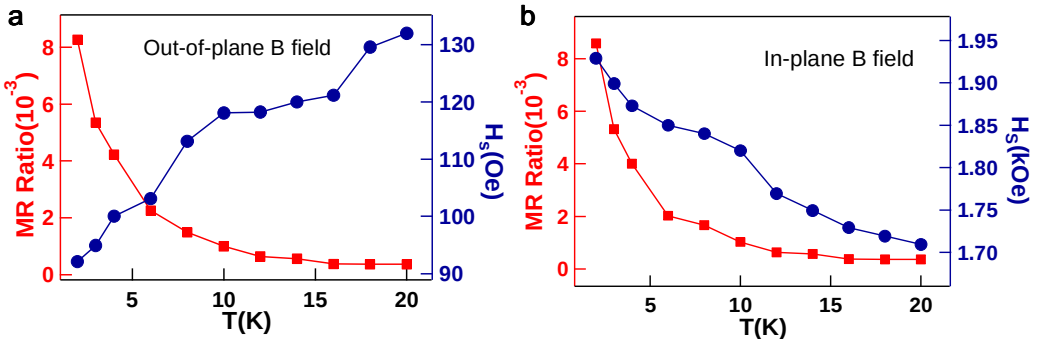

Figure 4-8. a-b, MR ratio (red square) and H_s (blue circle) as a function of temperature with out-of-plane (a) and in-plane magnetic field (b) applied. For both out-of-plane and in-plane case, the MR ratio reduces as temperature increases as shown in the red curves in (a) and (b). With out-of-plane magnetic field, H_s increases as temperature arises (a); while with in-plane magnetic field, H_s decreases as temperature increases (b), consistent with the MOKE data.

To further investigate the magnetic properties of the TI/FMI bilayer and verify the role of broken/preserved TRS in the spectrum of TI, MOKE measurements were performed at various temperatures to study both the out-of-plane (polar mode) and in-plane components (longitudinal mode) of the magnetic moment of the YIG layer and the Bi_2Se_3/YIG bilayer. The sample was mounted in a cryostat and cooled to 4.4 K at zero magnetic field. A laser beam with wavelength of 750 nm was focused either on the YIG or the Bi_2Se_3/YIG portion of the device and MOKE measurements were performed at increasing temperatures.

4.4. MOKE Measurements of TI/YIG Heterostructure

4.4.1. Polar and Longitudinal MOKE Measurement Setup

Magneto-optical Kerr effect (MOKE) describes rotation of polarization plane of a reflected light of an object with respect to the linearly polarized incident light due to its interaction with the magnetic moment of the object and thus can be used to directly probe the magnetization of materials; a well-established experimental technique. In our measurements, we used a linear polarized 750 nm laser beam for incident light and employed a half-wave plate and a Wollaston prism to resolve the Kerr rotation along with Si balanced photodetector for detection(see Figures 4-9(a)-(b)). While the Kerr rotation with an out-of-plane external field and normally incident light (Polar MOKE) is dominated by the out-of-plane component of the magnetic moment, the geometry of in-plane magnetic field and angled incident light (Longitudinal MOKE) can reveal field-dependent behavior of the in-plane component of the magnetic moment as well. The magnetic field range we applied is ± 6 kOe for the setup.

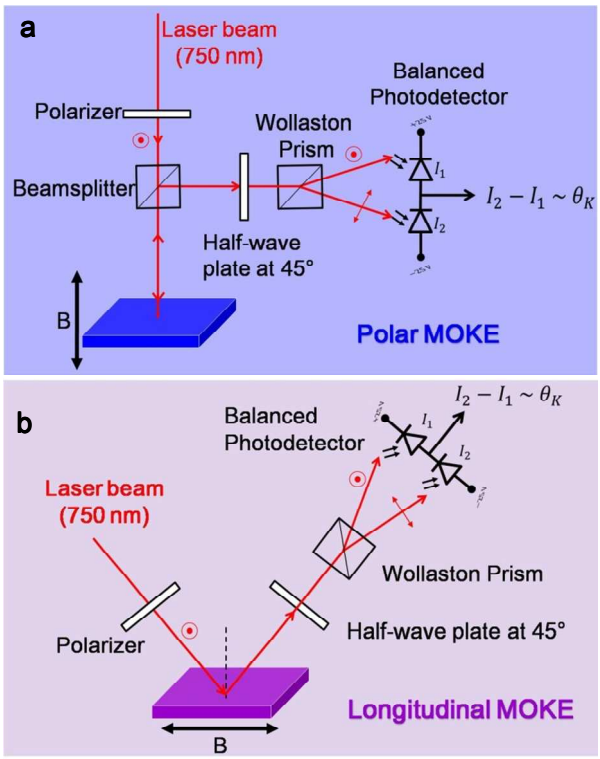

Figure 4-9. a-b, Polar (a) and Longitudinal (b) MOKE measurement setup. While the Kerr rotation with an out-of-plane external field and normally incident light (Polar MOKE) is dominated by the out-of-plane component of the magnetic moment, the geometry of in-plane magnetic field and angled incident light (Longitudinal MOKE) can reveal field-dependent behavior of the in-plane component of the magnetic moment.

4.4.2. Temperature Dependence of Polar and Longitudinal Mode of YIG

We show comprehensive temperature dependent polar and longitudinal MOKE of YIG data in Figures. 4-10a-b. The magnetization of YIG substrate is tilted from perfect in-plane

to canted out-of-plane during cooled down process. This can be confirmed by comparing the saturation field (H_s) of polar and longitudinal MOKE hysteresis loops. The H_s obtained from polar MOKE data (Figure 4-10a) increases as temperature arises, and are summarized in the red curve in Figure 4-10c. While the H_s of longitudinal mode hysteresis loops (Figure 4-10b) decreases as temperature increases, indicated by the blue curve Figure 4-10c. Comparing the temperature dependence of H_s of both curves in Figure 4-10c, the longitudinal one shows relatively steeper slope while the polar one shows relatively constant change. The opposite temperature dependence of H_s for the polar and longitudinal modes is mainly due to the fact that the out-of-plane anisotropy is weakened while the in-plane anisotropy is enhanced as temperature increases. The detailed mechanism will be explained in session 4.4.3. It should be noted that for temperature >200 K, the out-of-plane moment cannot be measured by MOKE within the range of available magnetic field ~6 kOe.

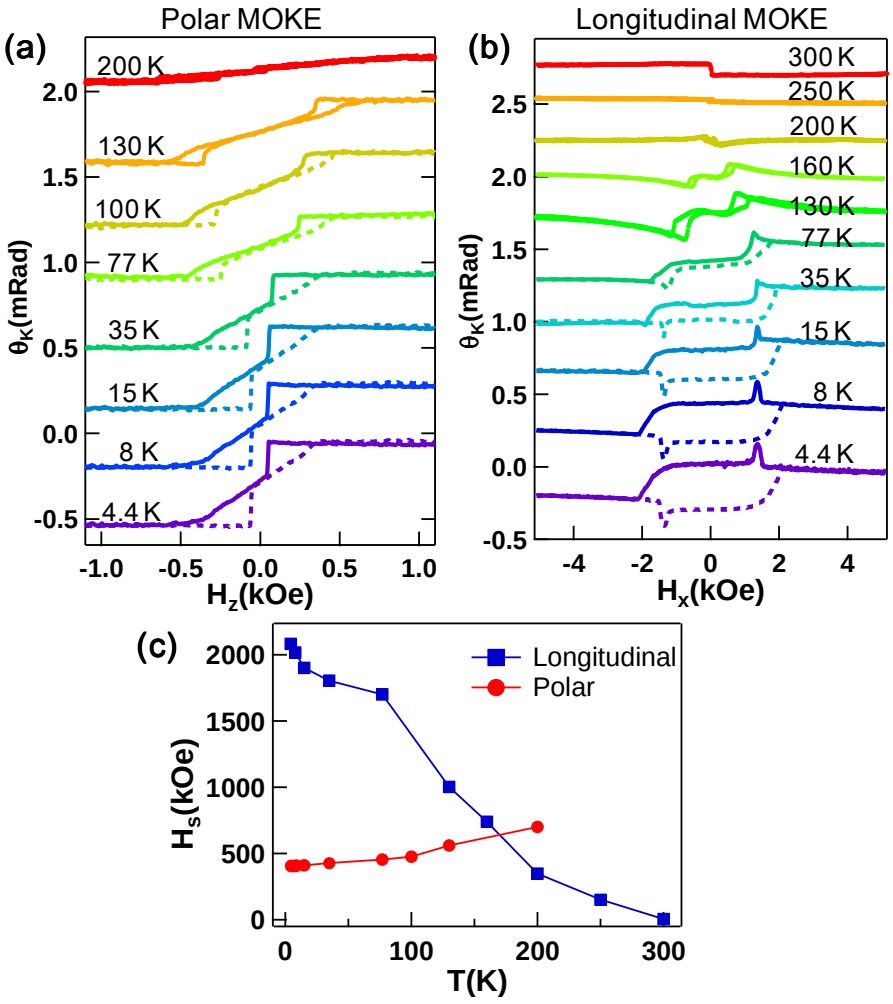

Figure 4-10. a-b, Temperature dependence of polar (a) and longitudinal (b) MOKE of YIG substrate. All curves are vertically shifted for clarification. **c**, Saturation field as a function of temperature, extracted from the hysteresis loops from **a-b**. The blue curve indicates the longitudinal mode, while the red curve indicates the polar mode. (This also appears in one of my publications Ref. 59.)

4.4.3. Micromagnetic Simulation of YIG

The presence of out-of-plane magnetization in YIG at low temperature is explained below. The YIG anisotropy includes three components: a shape anisotropy, favoring in plane magnetization; a magnetocrystalline anisotropy, favoring magnetization along the <111> axis which are at 90˚ and 35˚ to the film plane due to the negative K_1 (magnetoelastic anisotropy coefficient) at low temperature; and a magnetoelastic anisotropy which favors out-of-plane magnetization because the YIG is under in-plane tension due to thermal mismatch with GGG. Based on bulk values of saturation magnetization, magnetocrystalline anisotropy constants, magnetostriction[157], lattice parameters[158] and thermal expansion coefficients of the YIG and GGG[159, 160], the shape anisotropy is the dominant term (for M = 160 kA/m, $K_{sh} = 1.6\times10^4$ J/m^3) promoting an in-plane easy axis at low temperatures. The magnetoelastic term is small because both the magnetostriction coefficient and the strain of the YIG are small. The YIG and GGG lattice parameters are well matched at room temperature, 12.376 Å for YIG, 12.375 Å for GGG[158], but GGG has a larger thermal expansion, $\alpha = 10.4\times10^{-6}$ for YIG, 8.96×10^{-6} for GGG at room temperature[159], so the YIG will be under in-plane tensile strain and out-of-plane compressive strain at low temperature. The magnetostriction $\lambda_{111} = -2.5\times10^{-6}$ at 4 K[157] and Young's modulus of 200 GPa[161] leads to a weak out of plane anisotropy. The magnetocrystalline anisotropy K_1 = -2500 J/m^3 at 4 K[157] is expected to produce a canting of the magnetization with significant out-of-plane component.

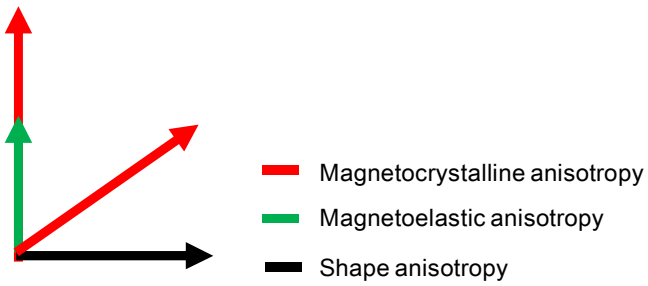

Figure 4-11. The YIG anisotropy at low temperature includes three components: a shape anisotropy, favoring in plane magnetization; a magnetocrystalline anisotropy, favoring magnetization along the <111> axis which are at 90˚ and 35˚ to the film plane, and a magnetoelastic anisotropy which favors out-of-plane magnetization.

A micromagnetic model of a 50 nm thick, 1 µm square of YIG using parameters characteristic of YIG at low temperature is shown in Figure 4-12 for an out-of-plane field. The model used the OOMMF code from NIST with cell sizes of 5 nm by 5 nm (in plane) by 25 nm (in the out-of-plane direction). M_s was 175 kA/m, K_1 was -2500 J/m^3, and damping constant was 0.5. The model included magnetocrystalline anisotropy, which required a coordinate rotation of the film to model the (111) orientation of the film, but magnetoelastic anisotropy was neglected. The model showed little remanence, but did reproduce hysteretic features near saturation similar to those seen in the polar MOKE data of YIG/GGG, and which were associated with the magnetization direction changing from the <111> out of plane direction to a <111> direction closer to the film plane as the field decreased.

The calculations predict a predominantly in plane magnetization at remanence with an out of plane canting resulting from the magnetocrystalline anisotropy. However, this is

based on bulk parameters. Imperfect stoichiometry in the YIG film would likely raise the magnetostriction as a result of the presence of magnetoelastic Fe ions with valence state other than 3+, which could provide a stronger out-of-plane contribution to the anisotropy.

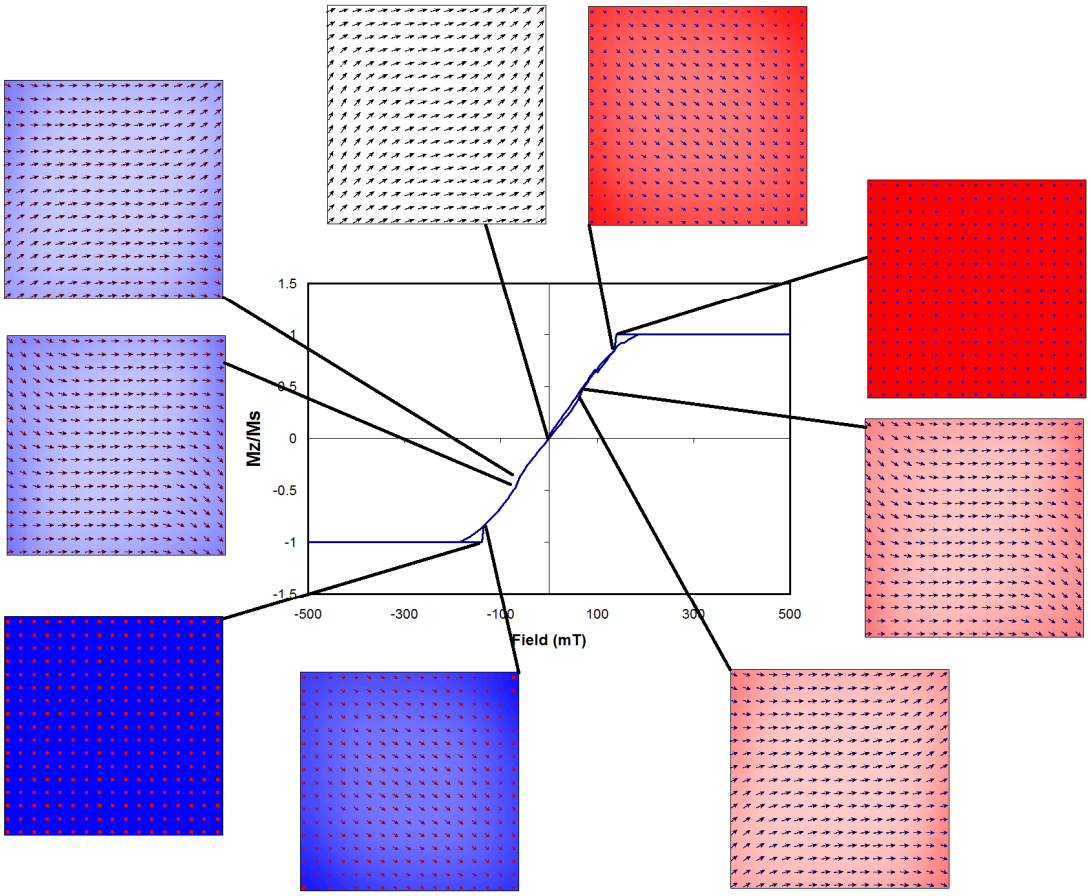

Figure 4-12. OOMMF model of YIG film, 1 µm square and 50 nm thick, for an out of plane field. Snapshots of the magnetic configuration are shown for different fields. The blue background indicates the $M_z < 0$ while the red background indicates the $M_z > 0$. The arrows present the x-y plane projection of magnetization in YIG.

4.4.4. Temperature Dependence of Polar and Longitudinal Mode of Bi_2Se_3/YIG

The polar and longitudinal MOKE signals of Bi_2Se_3/YIG differed from those of YIG in the sign of the MOKE signal as well as the shape of the longitudinal loops. However, the switching fields were the same as those of the YIG films, and hysteresis occurred up to at least 130 K for the polar signal and 77 K for the longitudinal signal (Figures 4-13**c**-**d**). Due to a decreased signal-to-noise ratio at higher temperatures, the polar MOKE of Bi_2Se_3/YIG does not provide conclusive evidence of survival of the proximity effect above 130 K. The data indicate a contribution to the MOKE signal from the Bi_2Se_3 layer, suggestive of magnetic order induced by the proximity effect at the Bi_2Se_3/YIG interface. This could be explained by exchange interaction, *i.e.*, hybridization between the *p*-orbital of Bi_2Se_3 and *d*-orbital of Fe in YIG at the interface, which induces a spin polarized state on the Bi_2Se_3 side. The direction of spin polarization of this state is presumed to be opposite to the YIG magnetization, as suggested by a recent theoretical work on proximity effect between a TI and a ferromagnetic insulator.[142] However, the possibility of an optical origin for the reversal of the sign of the polar MOKE cannot be completely ruled out. In order to clarify microscopic origin of the proximity effect, comprehensive theoretical investigation is required.

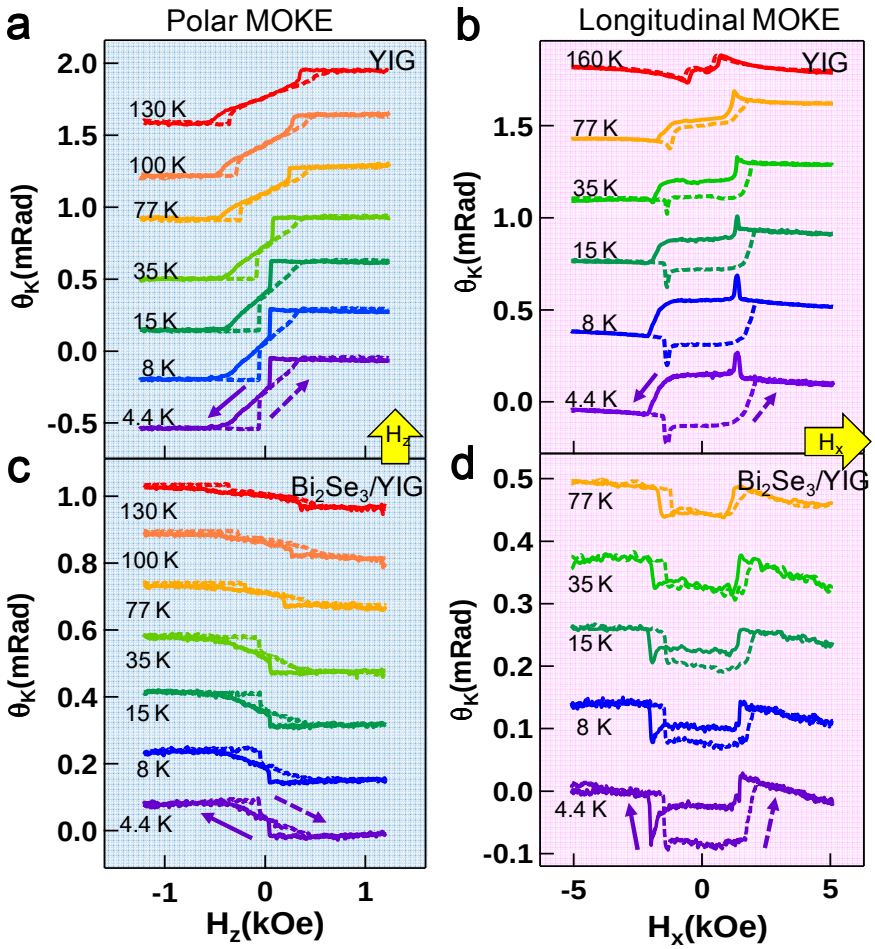

Figure 4-13. Temperature-dependent magnetization by MOKE measurements. a-b, Polar and longitudinal MOKE of YIG substrate. **c-d**, Polar and longitudinal MOKE of Bi_2Se_3/YIG heterostructure. All curves are vertically shifted for clarification. The hysteresis loops of **a** and **c** show different signs, suggesting that the exchange coupling induced spin polarization of Bi_2Se_3 is opposite to YIG magnetization. The out-of-plane magnetization of Bi_2Se_3/YIG can be clearly seen up to 130 K (**c**), indicating the high temperature magnetic order of TI induced by proximity effect. The longitudinal MOKE of Bi_2Se_3/YIG can be

measured up to 77 K (**d**), presenting a coupled but distinct switching behavior from that of YIG (**b**). (This also appears in one of my publications Ref. 59.)

In addition, to exclude any contribution from GGG substrate, we performed MOKE measurements for Bi_2Se_3/GGG control sample. Linear paramagnetic signals were observed for both GGG and Bi_2Se_3/GGG.

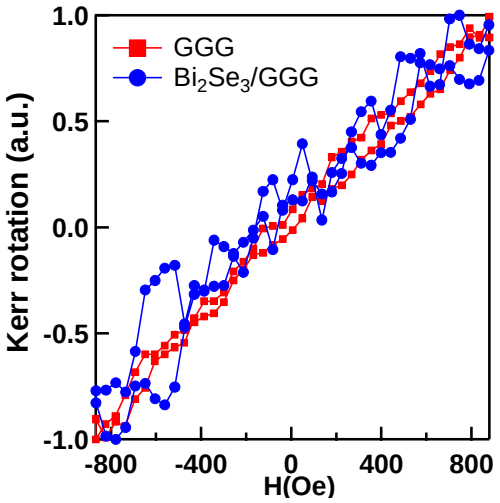

Figure 4-14. Longitudinal MOKE of GGG substrate and Bi_2Se_3/GGG showing a linear paramagnetic signal at T=77 K, which excludes any magnetic contribution from GGG substrate.

Breaking the TRS requires an out-of-plane component of the magnetization of the YIG which is readily available in our case owing to the canting of the magnetization. This can introduce a gap in the bottom SS due to proximity-induced magnetic ordering from the

exchange coupling between the Bi_2Se_3 bottom surface and the top surface of YIG. Figure 4-15**a** schematically shows the coupling between Bi_2Se_3 and the perpendicular component of the magnetization of the YIG, in which up and down magnetization is indicated by the red and blue arrows respectively. At fields below saturation, domain walls in the YIG can be formed, as illustrated in Figure 4-15**a**. In the middle of the wall, the out-of-plane magnetization vanishes leading to a gapless region of the SS, shown schematically in Figure 4-15**b**.

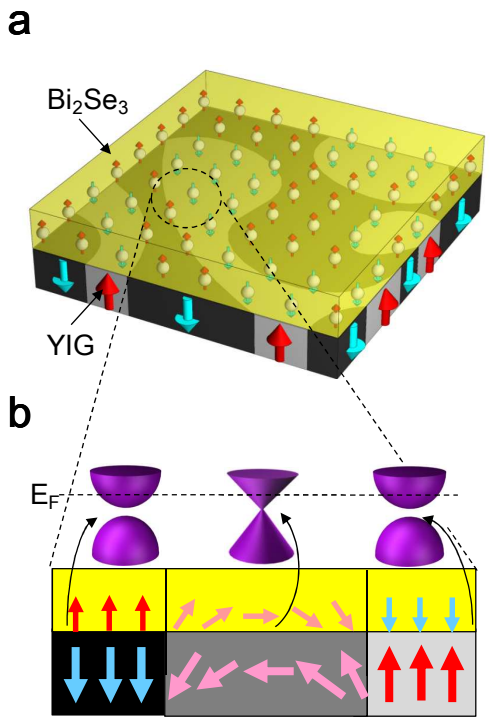

Figure 4-15. a, Schematic of the Bi_2Se_3/YIG heterostructure in the presence of YIG domain pattern. The red and blue arrows indicate up and down magnetization, respectively**. b**, Cross-sectional view of Bi_2Se_3/YIG interface. Bi_2Se_3 bottom surface state is gapped through exchange interaction by YIG out-of-plane magnetization at domain regions, while SS

remains gapless at the center of domain wall. (This also appears in one of my publications Ref. 59.)

4.5 Comparison Between Transport and MOKE

To explore the influence of the YIG on the transport of the surface states of the TI, we compare the low temperature MOKE measurements of both Bi_2Se_3/YIG and YIG with the corresponding magnetotransport measurements in Figure 4-16. [59] For sufficiently large negative perpendicular magnetic field H_z(region **I** in Figure 4-16**a**), the YIG substrate is a single domain with perpendicular magnetic moment, creating a gap in the SS at the bottom interface of the TI.[162] As the field decreases in magnitude, the perpendicular magnetization component of the YIG and the Bi_2Se_3/YIG drops abruptly at -90 Oe (Figures 4-16**a**-**b**). At the same perpendicular magnetic field H_z, instead of continuing the WAL behavior, a sharp rise of the longitudinal MR is observed, as shown by subtracting the WAL background in Figure 4-16**c**. The multi-domain configuration during the reversal process of the YIG may lead to gapped surface states within the domains and gapless SS in the domain walls, resulting in a spatially non-uniform spectrum for the surface states.[1, 3] This may introduce additional scattering for SS carriers which results in an overall increase of resistance in the device. As the perpendicular component of magnetization increases with increasing of the positive field, the number of domains decreases and hence the ΔMR of TI is gradually

reduced as shown in Figure 4-16**c**. Finally, when the field enters region **III** (~0.5 kOe), the YIG substrate is saturated in the opposite direction and the MR of the TI rejoins the WAL background. The right panel of Figure 4-16 illustrates a similar comparison of MOKE and MR measurements of both YIG and TI/YIG with an in-plane magnetic field H_x. In contrary to the out-of-plane case, with in-plane field, the TRS is restored at larger magnetic fields (regions **I** and **III**) causing a gapless spectrum of the SS. In region **II,** again, the domain nucleation leads to a rapid increase in the MR owing to the multi-domain formation of YIG. Figure 4-16**f** presents the resistance after subtraction of the parabolic background. There is no appreciable change in the ΔMR at region **II** with an in-plane field, which is consistent with the constant magnetization of YIG (Figure 4-16**d**) and TI/YIG (Figure 4-16**e**).

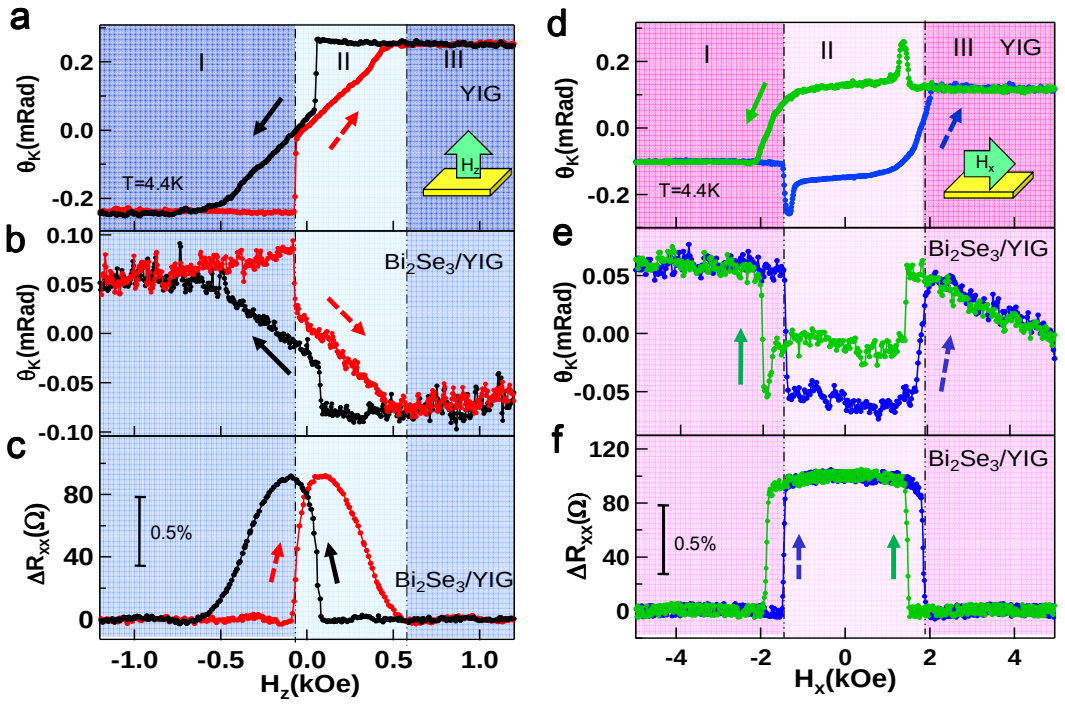

Figure 4-16. The comparison between MOKE and magnetotransport of Bi_2Se_3/YIG at 4.4 K. a-b, In Figure 4-16**a** regions **I** and **III**, the YIG substrate is single domain with magnetic moment aligned with the perpendicular magnetic field H_z. When magnetic field is swept from region **I** to ~ -90 Oe, as indicated by the dashed line, the domain nucleation is initiated in the YIG substrate, which is illustrated by a sharp increase in the polar MOKE of YIG (**a**) and correspondingly the sharp drop in the Bi_2Se_3/YIG (**b**). **c**, WAL background subtracted ΔMR shows a shape increase of resistance at ~90 Oe, which is influenced by the multi-domains in the YIG substrate. **d-e**, In-plane magnetization of YIG (**d**) and Bi_2Se_3/YIG (**e**) measured by a longitudinal-mode MOKE setup. The peaks in the hysteresis loop may come from the domain nucleation. **f**, Parabolic background subtracted MR with in-plane field applied, clearly displaying two resistance states. The switching field in the MR data is consistent with the MOKE data (**d**-**e**). (This also appears in one of my publications Ref. 59.)

The presence of domain walls during the reversal process of the YIG can result in the formation of additional chiral mode conducting channel in the TI bottom surface states, as theories predicted,[1, 3] which will lower the resistance. However, our experimental results show an increase of resistance in region **II**, suggesting that the chiral modes conduction has a minor contribution here, which could be due to the fact that the device dimension is much larger than the domain size of YIG estimated in the order of 100 nm. As mentioned before, the smaller AMR ratio (~0.2%) compared with the ΔMR ratio (~1%) in Figures 4-16**c** and **f**

suggests that the hysteretic ΔMR is not dominated by AMR. In addition to AMR and increased scattering due to spatially non-uniform SS spectrum, another possible effect that could contribute to the increase of MR is the domain wall resistance due to the mistracking of carriers spin and the background magnetization texture.[163] As the spin and momentum is perpendicular locked for surface state, the spin mistracking could be especially non-trivial when the background magnetization is not along the surface state spin direction. In order to clarify the possible different mechanisms in the hysteretic MR, further theoretical and experimental work is required.

4.6. Summary

In summary, a Bi_2Se_3/YIG heterostructure has been used to cleanly probe the surface magnetic behavior of Bi_2Se_3 due to the magnetic proximity effect. Our measured butterfly and square shaped magnetoresistance loops provided direct evidence of magnetic coupling between the insulating YIG and Bi_2Se_3. More significantly, for the first time, magnetic ordering at the Bi_2Se_3/YIG interface has been demonstrated at temperatures up to at least 130 K by MOKE measurements. Consistent with numerical simulations, while the YIG substrate shows in-plane anisotropy at room temperature, a canting of magnetization toward out-of-plane direction is clearly observed at lower temperatures by Polar MOKE, most likely due to magnetocrystalline anisotropy. The magnetic configuration of YIG is expected

to be useful to control the TRS of Bi_2Se_3 surface states, due to the coupling of magnetic order between the YIG and the Bi_2Se_3 at the interface.

Chapter 5

Conclusion

TI is a rather complex system along with intriguing physics and intrinsic material defeats. The work presented in this dissertation focused on the fundamental transport study in 3D topological insulators. Numerous MBE effort was focused on reducing bulk carrier density and improving thin film quality. In particular, *in-situ* Al surface passivation of Bi_2Se_3 inside MBE has been studied to reduce the carrier density and reveal the pristine topological surface states. To achieve the bulk insulating state, $(B_{i0.57}Sb_{0.43})_2Te_3$ material has been grown and optimized, in which we observed the ambipolar effect in 4-9 QLs thin films. We have demonstrated a crossover from weak antilocalization to weak localization in 4 and 5 QLs $(B_{i0.57}Sb_{0.43})_2Te_3$ thin films by sweeping gate voltage. Moreover, to realize the room temperature operation, we have studied the high temperature magnetic properties in Bi_2Se_3/YIG heterostructure by both magnetotransport and MOKE methods.

Specifically, in chapter 2, we show that *in situ* Al passivation inside a MBE chamber could inhibit the degradation process and reveal the pristine topological surface states. Dual evidence from SdH oscillations and weak antilocalization WAL effect, originated from the π Berry phase, suggests that the helically spin-polarized surface states are well preserved by the proposed in situ Al passivation. In contrast, we show the degradation of surface states for the unpassivated control samples, in which the 2D carrier density is increased 39.2% due

to ambient *n*-doping, the SdH oscillations are completely absent, and a large deviation from WAL is observed.

In chapter 3, we demonstrate the evidence of a surface gap opening in TI thin films of $(B_{i0.57}Sb_{0.43})_2Te_3$ below six quintuple layers through transport and scanning tunneling spectroscopy measurements. By effective tuning the Fermi level via gate-voltage control, we unveil a striking competition between WL and WAL at low magnetic fields in nonmagnetic ultrathin films, possibly owing to the change of the net Berry phase. Furthermore, when the Fermi level is swept into the surface gap of ultrathin samples, the overall unitary behaviors are revealed at higher magnetic fields, which are in contrast to the pure WAL signals obtained in thicker films. These findings show an exotic phenomenon characterizing the gapped TI surface states and point to the future realization of quantum spin Hall effect and dissipationless TI-based applications.

In chapter 4, we study the magnetic properties of Bi_2Se_3 surface states in the proximity of a high T_c ferrimagnetic insulator YIG. Proximity-induced butterfly and square-shaped magnetoresistance loops are observed by magneto-transport measurements with out-of-plane and in-plane fields, respectively, and can be correlated with the magnetization of the YIG substrate. More importantly, a magnetic signal from the Bi_2Se_3 up to 130 K is clearly observed by magneto-optical Kerr effect measurements. Our results demonstrate the proximity-induced TI magnetism at higher temperatures, an important step toward room-temperature application of TI-based spintronic devices.

The future work will be focusing on the engineering of a TI and FMI heterostructure to study high temperature TI-based spintronic devices, in which the TI is controlled by breaking the TRS using a FMI with perpendicular magnetization component. A YIG film with out-of-plane anisotropy at > 300 K could potentially manipulate the magnetic properties of a TI may even above room temperature.

References

1. Qi, X.-L.; Zhang, S.-C. *Reviews of Modern Physics* **2011,** 83, (4), 1057-1110.

2. Moore, J. E. *Nature* **2010,** 464, (7286), 194-198.

3. Hasan, M. Z.; Kane, C. L. *Reviews of Modern Physics* **2010,** 82, (4), 3045.

4. Zhang, Y.; He, K.; Chang, C.-Z.; Song, C.-L.; Wang, L.-L.; Chen, X.; Jia, J.-F.; Fang, Z.; Dai, X.; Shan, W.-Y.; Shen, S.-Q.; Niu, Q.; Qi, X.-L.; Zhang, S.-C.; Ma, X.-C.; Xue, Q.-K. *Nat Phys* **2010,** 6, (8), 584-588.

5. Zhang, T.; Cheng, P.; Chen, X.; Jia, J.-F.; Ma, X.; He, K.; Wang, L.; Zhang, H.; Dai, X.; Fang, Z.; Xie, X.; Xue, Q.-K. *Physical Review Letters* **2009,** 103, (26), 266803.

6. Qi, X.-L.; Hughes, T. L.; Zhang, S.-C. *Physical Review B* **2008,** 78, (19), 195424.

7. Zhang, H.; Liu, C.-X.; Qi, X.-L.; Dai, X.; Fang, Z.; Zhang, S.-C. *Nat Phys* **2009,** 5, (6), 438-442.

8. Kane, C. L.; Mele, E. J. *Physical Review Letters* **2005,** 95, (14), 146802.

9. Moore, J. E.; Balents, L. *Physical Review B* **2007,** 75, (12), 121306.

10. Klitzing, K. v.; Dorda, G.; Pepper, M. *Physical Review Letters* **1980,** 45, (6), 494-497.

11. Roth, L. M. *Physical Review* **1966,** 145, (2), 434.

12. Laughlin, R. B. *Physical Review B* **1981,** 23, (10), 5632-5633.

13. Stormer, H. L. *Reviews of Modern Physics* **1999,** 71, (4), 875-889.

14. Novoselov, K. S.; Jiang, Z.; Zhang, Y.; Morozov, S. V.; Stormer, H. L.; Zeitler, U.; Maan, J. C.; Boebinger, G. S.; Kim, P.; Geim, A. K. *Science* **2007,** 315, (5817), 1379.

15. Thouless, D. J.; Kohmoto, M.; Nightingale, M. P.; den Nijs, M. *Phys. Rev. Lett.* **1982,** 49, (6), 405--408.

16. König, M.; Wiedmann, S.; Brüne, C.; Roth, A.; Buhmann, H.; Molenkamp, L. W.; Qi, X.-L.; Zhang, S.-C. *Science* **2007,** 318, (5851), 766-770.

17. Qi, X.-L.; Zhang, S.-C. *Physics Today* **2010,** 63, (1), 33-38.

18. Bernevig, B. A.; Hughes, T. L.; Zhang, S.-C. *Science* **2006,** 314, (5806), 1757-1761.

19. Bernevig, B. A.; Zhang, S.-C. *Physical Review Letters* **2006,** 96, (10), 106802.

20. Berry, M. V. *Proceedings of the Royal Society of London. A. Mathematical and Physical Sciences* **1984,** 392, (1802), 45-57.

21. Ando, T.; Nakanishi, T.; Saito, R. *Journal of the Physical Society of Japan* **1998,** 67, 2857-2862.

22. Haldane, F. D. M. *Physical Review Letters* **1988,** 61, (18), 2015-2018.

23. Kane, C. L.; Mele, E. J. *Physical Review Letters* **2005,** 95, (22).

24. Goldberg, A. C.; Kennerly, S. W.; Little, J. W.; Shafer, T. A.; Mears, C. L.; Schaake, H. F.; Winn, M.; Taylor, M.; Uppal, P. N. *OPTICE* **2003,** 42, (1), 30-46.

25. Le, H. Q.; Arias, J. M.; Zandian, M.; Zucca, R.; Liu, Y. Z. *Applied Physics Letters* **1994,** 65, (7), 810-812.

26. Du, L.; Knez, I.; Sullivan, G.; Du, R.-R. *arXiv:1306.1925* **2013**.

27. Xu, Y.; Yan, B.; Zhang, H.-J.; Wang, J.; Xu, G.; Tang, P.; Duan, W.; Zhang, S.-C. *Physical Review Letters* **2013,** 111, (13), 136804.

28. Yu, R.; Zhang, W.; Zhang, H.-J.; Zhang, S.-C.; Dai, X.; Fang, Z. *Science* **2010,** 329, (5987), 61-64.

29. He, K.; Wang, Y.; Xue, Q.-K. *National Science Review* **2013**.

30. Liu, C.-X.; Qi, X.-L.; Dai, X.; Fang, Z.; Zhang, S.-C. *Physical Review Letters* **2008,** 101, (14), 146802.

31. Buhmann, H. **2012**.

32. Chang, C.-Z.; Zhang, J.; Feng, X.; Shen, J.; Zhang, Z.; Guo, M.; Li, K.; Ou, Y.; Wei, P.; Wang, L.-L.; Ji, Z.-Q.; Feng, Y.; Ji, S.; Chen, X.; Jia, J.; Dai, X.; Fang, Z.; Zhang, S.-C.; He, K.; Wang, Y.; Lu, L.; Ma, X.-C.; Xue, Q.-K. *Science* **2013,** 340, (6129), 167-170.

33. Kou, X.; Guo, S.-T.; Fan, Y.; Pan, L.; Lang, M.; Jiang, Y.; Shao, Q.; Nie, T.; Murata, K.; Tang, J.; Wang, Y.; He, L.; Lee, T.-K.; Lee, W.-L.; Wang, K. L. *Physical Review Letters* **2014,** 113, (13), 137201.

34. Datta, S., *Electronic transport in mesoscopic systems*. Cambridge university press: 1997.

35. Kou, X. F.; He, L.; Lang, M. R.; Fan, Y. B.; Wong, K.; Jiang, Y.; Nie, T. X.; Jiang, W. J.; Upadhyaya, P.; Xing, Z. K.; Wang, Y.; Xiu, F. X.; Schwartz, R. N.; Wang, K. L. *Nano Lett* **2013,** 13, (10), 4587-4593.

36. Roth, A.; Brune, C.; Buhmann, H.; Molenkamp, L. W.; Maciejko, J.; Qi, X. L.; Zhang, S. C. *Science* **2009,** 325, (5938), 294-297.

37. Checkelsky, J. G.; Ye, J.; Onose, Y.; Iwasa, Y.; Tokura, Y. *Nat Phys* **2012,** 8, (10), 729-733.

38. Hsieh, D.; Qian, D.; Wray, L.; Xia, Y.; Hor, Y. S.; Cava, R. J.; Hasan, M. Z. *Nature* **2008,** 452, (7190), 970-974.

39. Fu, L.; Kane, C. L. *Physical Review B* **2007,** 76, (4), 045302.

40. Chen, Y. L.; Analytis, J. G.; Chu, J.-H.; Liu, Z. K.; Mo, S.-K.; Qi, X. L.; Zhang, H. J.; Lu, D. H.; Dai, X.; Fang, Z.; Zhang, S. C.; Fisher, I. R.; Hussain, Z.; Shen, Z.-X. *Science* **2009,** 325, (5937), 178-181.

41. Hor, Y. S.; Richardella, A.; Roushan, P.; Xia, Y.; Checkelsky, J. G.; Yazdani, A.; Hasan, M. Z.; Ong, N. P.; Cava, R. J. *Phys. Rev. B* **2009,** 79, (19), 195208.

42. Hsieh, D.; Xia, Y.; Qian, D.; Wray, L.; Meier, F.; Dil, J. H.; Osterwalder, J.; Patthey, L.; Fedorov, A. V.; Lin, H.; Bansil, A.; Grauer, D.; Hor, Y. S.; Cava, R. J.; Hasan, M. Z. *Phys. Rev. Lett.* **2009,** 103, (14), 146401.

43. Hor, Y. S.; Richardella, A.; Roushan, P.; Xia, Y.; Checkelsky, J. G.; Yazdani, A.; Hasan, M. Z.; Ong, N. P.; Cava, R. J. *Physical Review B* **2009,** 79, (19), 195208.

44. Hsieh, D.; Xia, Y.; Qian, D.; Wray, L.; Dil, J. H.; Meier, F.; Osterwalder, J.; Patthey, L.; Checkelsky, J. G.; Ong, N. P.; Fedorov, A. V.; Lin, H.; Bansil, A.; Grauer, D.; Hor, Y. S.; Cava, R. J.; Hasan, M. Z. *Nature* **2009,** 460, (7259), 1101-1105.

45. Park, S. R.; Jung, W. S.; Kim, C.; Song, D. J.; Kim, C.; Kimura, S.; Lee, K. D.; Hur, N. *Physical Review B* **2010,** 81, (4), 041405.

46. Xia, Y.; Qian, D.; Hsieh, D.; Wray, L.; Pal, A.; Lin, H.; Bansil, A.; Grauer, D.; Hor, Y. S.; Cava, R. J.; Hasan, M. Z. *Nat Phys* **2009,** 5, (6), 398-402.

47. Hsieh, D.; Xia, Y.; Qian, D.; Wray, L.; Meier, F.; Dil, J. H.; Osterwalder, J.; Patthey, L.; Fedorov, A. V.; Lin, H.; Bansil, A.; Grauer, D.; Hor, Y. S.; Cava, R. J.; Hasan, M. Z. *Physical Review Letters* **2009,** 103, (14), 146401.

48. Alpichshev, Z.; Analytis, J. G.; Chu, J. H.; Fisher, I. R.; Chen, Y. L.; Shen, Z. X.; Fang, A.; Kapitulnik, A. *Physical Review Letters* **2010,** 104, (1), 016401.

49. He, L.; Xiu, F.; Wang, Y.; Fedorov, A. V.; Huang, G.; Kou, X.; Lang, M.; Beyermann, W. P.; Zou, J.; Wang, K. L. *Journal of Applied Physics* **2011,** 109, (10), 103702.

50. Lang, M.; He, L.; Xiu, F.; Yu, X.; Tang, J.; Wang, Y.; Kou, X.; Jiang, W.; Fedorov, A. V.; Wang, K. L. *ACS Nano* **2011,** 6, (1), 295-302.

51. He, L.; Xiu, F.; Yu, X.; Teague, M.; Jiang, W.; Fan, Y.; Kou, X.; Lang, M.; Wang, Y.; Huang, G.; Yeh, N.-C.; Wang, K. L. *Nano Letters* **2012,** 12, (3), 1486-1490.

52. Xinxin, Y.; Liang, H.; Murong, L.; Wanjun, J.; Faxian, X.; Zhiming, L.; Yong, W.; Xufeng, K.; Peng, Z.; Jianshi, T.; Guan, H.; Jin, Z.; Kang, L. W. *Nanotechnology* **2013,** 24, (1), 015705.

53. Lang, M.; He, L.; Kou, X.; Upadhyaya, P.; Fan, Y.; Chu, H.; Jiang, Y.; Bardarson, J. H.; Jiang, W.; Choi, E. S.; Wang, Y.; Yeh, N.-C.; Moore, J.; Wang, K. L. *Nano Letters* **2012,** 13, (1), 48-53.

54. He, L.; Kou, X.; Lang, M.; Choi, E. S.; Jiang, Y.; Nie, T.; Jiang, W.; Fan, Y.; Wang, Y.; Xiu, F.; Wang, K. L. *Sci. Rep.* **2013,** 3.

55. Kou, X. F.; Jiang, W. J.; Lang, M. R.; Xiu, F. X.; He, L.; Wang, Y.; Yu, X. X.; Fedorov, A. V.; Zhang, P.; Wang, K. L. *Journal of Applied Physics* **2012,** 112, (6), 063912-6.

56. Kou, X.; Lang, M.; Fan, Y.; Jiang, Y.; Nie, T.; Zhang, J.; Jiang, W.; Wang, Y.; Yao, Y.; He, L.; Wang, K. L. *ACS Nano* **2013**.

57. Kou, X.; He, L.; Lang, M.; Fan, Y.; Wong, K.; Jiang, Y.; Nie, T.; Jiang, W.; Upadhyaya, P.; Xing, Z.; Wang, Y.; Xiu, F.; Schwartz, R. N.; Wang, K. L. *Nano Letters* **2013,** 13, (10), 4587-4593.

58. Kou, X. F.; He, L.; Xiu, F. X.; Lang, M. R.; Liao, Z. M.; Wang, Y.; Fedorov, A. V.; Yu, X. X.; Tang, J. S.; Huang, G.; Jiang, X. W.; Zhu, J. F.; Zou, J.; Wang, K. L., *Epitaxial growth of high mobility Bi2Se3 thin films on CdS*. AIP: 2011; Vol. 98, p 242102.

59. Lang, M.; Montazeri, M.; Onbasli, M. C.; Kou, X.; Fan, Y.; Upadhyaya, P.; Yao, K.; Liu, F.; Jiang, Y.; Jiang, W.; Wong, K. L.; Yu, G.; Tang, J.; Nie, T.; He, L.; Schwartz, R. N.; Wang, Y.; Ross, C. A.; Wang, K. L. *Nano Letters* **2014,** 14, (6), 3459-3465.

60. Wang, M.-X.; Liu, C.; Xu, J.-P.; Yang, F.; Miao, L.; Yao, M.-Y.; Gao, C. L.; Shen, C.; Ma, X.; Chen, X.; Xu, Z.-A.; Liu, Y.; Zhang, S.-C.; Qian, D.; Jia, J.-F.; Xue, Q.-K. *Science* **2012**.

61. Liu, M.; Zhang, J.; Chang, C.-Z.; Zhang, Z.; Feng, X.; Li, K.; He, K.; Wang, L.-l.; Chen, X.; Dai, X.; Fang, Z.; Xue, Q.-K.; Ma, X.; Wang, Y. *Physical Review Letters* **2012,** 108, (3), 036805.

62. Chang, C.-Z.; Zhang, J.; Liu, M.; Zhang, Z.; Feng, X.; Li, K.; Wang, L.-L.; Chen, X.; Dai, X.; Fang, Z.; Qi, X.-L.; Zhang, S.-C.; Wang, Y.; He, K.; Ma, X.-C.; Xue, Q.-K. *Advanced Materials* **2013,** 25, (7), 1065-1070.

63. Zhang, D.; Richardella, A.; Rench, D. W.; Xu, S.-Y.; Kandala, A.; Flanagan, T. C.; Beidenkopf, H.; Yeats, A. L.; Buckley, B. B.; Klimov, P. V.; Awschalom, D. D.; Yazdani, A.; Schiffer, P.; Hasan, M. Z.; Samarth, N. *Physical Review B* **2012,** 86, (20), 205127.

64. Richardella, A.; Zhang, D. M.; Lee, J. S.; Koser, A.; Rench, D. W.; Yeats, A. L.; Buckley, B. B.; Awschalom, D. D.; Samarth, N. *Applied Physics Letters* **2010,** 97, (26), 262104-3.

65. Kandala, A.; Richardella, A.; Rench, D. W.; Zhang, D. M.; Flanagan, T. C.; Samarth, N. *Applied Physics Letters* **2013,** 103, (20), -.

66. Taskin, A. A.; Sasaki, S.; Segawa, K.; Ando, Y. *Physical Review Letters* **2012,** 109, (6), 066803.

67. Taskin, A. A.; Sasaki, S.; Segawa, K.; Ando, Y. *Advanced Materials* **2012,** 24, (41), 5581-5585.

68. Zhang, G.; Qin, H.; Teng, J.; Guo, J.; Guo, Q.; Dai, X.; Fang, Z.; Wu, K. *Applied Physics Letters* **2009,** 95, (5), -.

69. Kim, Y. S.; Brahlek, M.; Bansal, N.; Edrey, E.; Kapilevich, G. A.; Iida, K.; Tanimura, M.; Horibe, Y.; Cheong, S.-W.; Oh, S. *Physical Review B* **2011,** 84, (7), 073109.

70. Chen, J.; Qin, H. J.; Yang, F.; Liu, J.; Guan, T.; Qu, F. M.; Zhang, G. H.; Shi, J. R.; Xie, X. C.; Yang, C. L.; Wu, K. H.; Li, Y. Q.; Lu, L. *Physical Review Letters* **2010,** 105, (17), 176602.

71. Schreyeck, S.; Tarakina, N. V.; Karczewski, G.; Schumacher, C.; Borzenko, T.; Brüne, C.; Buhmann, H.; Gould, C.; Brunner, K.; Molenkamp, L. W. *Applied Physics Letters* **2013,** 102, (4), -.

72. Teweldebrhan, D.; Goyal, V.; Balandin, A. A. *Nano Letters* **2010,** 10, (4), 1209-1218.

73. Shahil, K. M. *Appl. Phys. Lett.* **2010,** 96, (15), 153103.

74. Kong, D.; Randel, J. C.; Peng, H.; Cha, J. J.; Meister, S.; Lai, K.; Chen, Y.; Shen, Z.-X.; Manoharan, H. C.; Cui, Y. *Nano Letters* **2009,** 10, (1), 329-333.

75. Cha, J. J.; Koski, K. J.; Cui, Y. *physica status solidi (RRL) – Rapid Research Letters* **2013,** 7, (1-2), 15-25.

76. Hong, S. S.; Cha, J. J.; Kong, D.; Cui, Y. *Nat Commun* **2012,** 3, 757.

77. Kong, D.; Chen, Y.; Cha, J. J.; Zhang, Q.; Analytis, J. G.; Lai, K.; Liu, Z.; Hong, S. S.; Koski, K. J.; Mo, S.-K.; Hussain, Z.; Fisher, I. R.; Shen, Z.-X.; Cui, Y. *Nat Nano* **2011,** 6, (11), 705-709.

78. Kong, D.; Dang, W.; Cha, J. J.; Li, H.; Meister, S.; Peng, H.; Liu, Z.; Cui, Y. *Nano Letters* **2010,** 10, (6), 2245-2250.

79. Castro Neto, A. H.; Guinea, F.; Peres, N. M. R.; Novoselov, K. S.; Geim, A. K. *Reviews of Modern Physics* **2009,** 81, (1), 109-162.

80. Ando, Y. *Journal of the Physical Society of Japan* **2013,** 82, (10), 102001.

81. Onsager, L. *Philosophical Magazine* **1952,** 43, (344), 1006-1008.

82. Butch, N. P.; Kirshenbaum, K.; Syers, P.; Sushkov, A. B.; Jenkins, G. S.; Drew, H. D.; Paglione, J. *Physical Review B* **2010,** 81, (24), 241301.

83. Analytis, J. G.; McDonald, R. D.; Riggs, S. C.; Chu, J.-H.; Boebinger, G. S.; Fisher, I. R. *Nat Phys* **2010,** 6, (12), 960-964.

84. Liu, M.; Chang, C.-Z.; Zhang, Z.; Zhang, Y.; Ruan, W.; He, K.; Wang, L.-l.; Chen, X.; Jia, J.-F.; Zhang, S.-C.; Xue, Q.-K.; Ma, X.; Wang, Y. *Physical Review B* **2011,** 83, (16), 165440.

85. Steinberg, H.; Laloë, J.-B.; Fatemi, V.; Moodera, J. S.; Jarillo-Herrero, P. *arXiv:1104.1404v1* **2011**.

86. Lang, M.; He, L.; Xiu, F.; Yu, X.; Tang, J.; Wang, Y.; Kou, X.; Jiang, W.; Fedorov, A. V.; Wang, K. L. *ACS Nano* **2011**.

87. Chen, J.; He, X. Y.; Wu, K. H.; Ji, Z. Q.; Lu, L.; Shi, J. R.; Smet, J. H.; Li, Y. Q. *Physical Review B* **2011,** 83, (24), 241304.

88. Xiu, F.; He, L.; Wang, Y.; Cheng, L.; Chang, L.-T.; Lang, M.; Huang, G.; Kou, X.; Zhou, Y.; Jiang, X.; Chen, Z.; Zou, J.; Shailos, A.; Wang, K. L. *Nat Nano* **2011,** 6, (4), 216-221.

89. Ren, Z.; Taskin, A. A.; Sasaki, S.; Segawa, K.; Ando, Y. *Physical Review B* **2010,** 82, (24), 241306.

90. Wang, Y.; Xiu, F.; Cheng, L.; He, L.; Lang, M.; Tang, J.; Kou, X.; Yu, X.; Jiang, X.; Chen, Z.; Zou, J.; Wang, K. L. *Nano Letters* **2012,** 12, (3), 1170-1175.

91. Analytis, J. G.; Chu, J.-H.; Chen, Y.; Corredor, F.; McDonald, R. D.; Shen, Z. X.; Fisher, I. R. *Physical Review B* **2010,** 81, (20), 205407.

92. Peng, H.; Lai, K.; Kong, D.; Meister, S.; Chen, Y.; Qi, X.-L.; Zhang, S.-C.; Shen, Z.-X.; Cui, Y. *Nat Mater* **2010,** 9, (3), 225-229.

93. Hikami, S.; Larkin, A. I.; Nagaoka, Y. *Prog. Theor. Phy.* **1980,** 63, (2), 707-710.

94. Lu, H.-Z.; Shi, J.; Shen, S.-Q. *Physical Review Letters* **2011,** 107, (7), 076801.

95. Bergmann, G. *Physics Reports* **1984,** 107, (1), 1-58.

96. Eto, K.; Ren, Z.; Taskin, A. A.; Segawa, K.; Ando, Y. *Physical Review B* **2010,** 81, (19), 195309.

97. Taskin, A. A.; Ren, Z.; Sasaki, S.; Segawa, K.; Ando, Y. *Physical Review Letters* **2011,** 107, (1), 016801.

98. Kong, D.; Cha, J. J.; Lai, K.; Peng, H.; Analytis, J. G.; Meister, S.; Chen, Y.; Zhang, H.-J.; Fisher, I. R.; Shen, Z.-X.; Cui, Y. *ACS Nano* **2011,** 5, (6), 4698-4703.

99. Zahid, F.; Lake, R. *Applied Physics Letters* **2010,** 97, (21), 212102.

100. Goyal, V. *Appl. Phys. Lett.* **2010,** 97, (13), 133117.

101. Hossain, M. Z.; Rumyantsev, S. L.; Shahil, K. M. F.; Teweldebrhan, D.; Shur, M.; Balandin, A. A. *ACS Nano* **2011,** 5, (4), 2657-2663.

102. Lind, H.; Lidin, S.; Häussermann, U. *Physical Review B* **2005,** 72, (18), 184101.

103. Qu, D.-X.; Hor, Y. S.; Xiong, J.; Cava, R. J.; Ong, N. P. *Science* **2010,** 329, (5993), 821-824.

104. Zhang, Y.; Tan, Y.-W.; Stormer, H. L.; Kim, P. *Nature* **2005,** 438, (7065), 201-204.

105. Novoselov, K. S.; Geim, A. K.; Morozov, S. V.; Jiang, D.; Katsnelson, M. I.; Grigorieva, I. V.; Dubonos, S. V.; Firsov, A. A. *Nature* **2005,** 438, (7065), 197-200.

106. Taskin, A. A.; Ando, Y. *Physical Review B* **2011,** 84, (3), 035301.

107. Mikitik, G. P.; Sharlai, Y. V. *Physical Review Letters* **1999,** 82, 2147-2150.

108. Dresselhaus, P. D.; Papavassiliou, C. M. A.; Wheeler, R. G.; Sacks, R. N. *Physical Review Letters* **1992,** 68, (1), 106.

109. Chen, G. L.; Han, J.; Huang, T. T.; Datta, S.; Janes, D. B. *Physical Review B* **1993,** 47, (7), 4084.

110. Koga, T.; Nitta, J.; Akazaki, T.; Takayanagi, H. *Physical Review Letters* **2002,** 89, (4), 046801.

111. Lu, H.-Z.; Shen, S.-Q. *Physical Review B* **2011,** 84, (12), 125138.

112. He, H.-T.; Wang, G.; Zhang, T.; Sou, I.-K.; Wong, G. K. L.; Wang, J.-N.; Lu, H.-Z.; Shen, S.-Q.; Zhang, F.-C. *Physical Review Letters* **2011,** 106, (16), 166805.

113. Kim, Y. S.; Brahlek, M.; Bansal, N.; Edrey, E.; Kapilevich, G. A.; lida, K.; Tanimura, M.; Horibe, Y.; Cheong, S.-W.; Oh, S. *arXiv:1104.0913v2* **2011**.

114. Cho, S.; Butch, N. P.; Paglione, J.; Fuhrer, M. S. *Nano Letters* **2011,** 11, (5), 1925-1927.

115. Zhang, L.; Hammond, R.; Dolev, M.; Liu, M.; Palevski, A.; Kapitulnik, A. *arXiv:1205.5832v1* **2012**.

116. Teague, M. L.; Chu, H.; Xiu, F. X.; He, L.; Wang, K. L.; Yeh, N. C. *Solid State Communications* **2012,** 152, (9), 747-751.

117. Zhang, J.; Chang, C.-Z.; Zhang, Z.; Wen, J.; Feng, X.; Li, K.; Liu, M.; He, K.; Wang, L.; Chen, X.; Xue, Q.-K.; Ma, X.; Wang, Y. *Nat Commun* **2011,** 2, 574.

118. Yu, X.; He, L.; Lang, M.; Jiang, W.; Xiu, F.; Liao, Z.; Wang, Y.; Kou, X.; Zhang, P.; Tang, J.; Huang, G.; Zou, J.; Wang, K. L. *Nanotechnology* **2013,** 24, (1), 015705.

119. Sacepe, B.; Oostinga, J. B.; Li, J.; Ubaldini, A.; Couto, N. J. G.; Giannini, E.; Morpurgo, A. F. *Nat Commun* **2011,** 2.

120. Ren, Z.; Taskin, A. A.; Sasaki, S.; Segawa, K.; Ando, Y. *Phys. Rev. B* **2011,** 84, (7), 075316.

121. Ren, Z.; Taskin, A. A.; Sasaki, S.; Segawa, K.; Ando, Y. *Phys. Rev. B* **2010,** 82, (24), 241306.

122. Garate, I.; Glazman, L. *Physical Review B* **2012,** 86, (3), 035422.

123. Mong, R. S. K.; Bardarson, J. H.; Moore, J. E. *Physical Review Letters* **2012,** 108, (7), 076804.

124. Ringel, Z.; Kraus, Y. E.; Stern, A. *Physical Review B* **2012,** 86, (4), 045102.

125. Ghaemi, P.; Mong, R. S. K.; Moore, J. E. *Physical Review Letters* **2010,** 105, (16), 166603.

126. Tse, W.-K.; MacDonald, A. H. *Physical Review Letters* **2010,** 105, (5), 057401.

127. Tserkovnyak, Y.; Loss, D. *Physical Review Letters* **2012,** 108, (18), 187201.

128. Qi, X.-L.; Li, R.; Zang, J.; Zhang, S.-C. *Science* **2009,** 323, (5918), 1184-1187.

129. Chen, Y. L.; Chu, J.-H.; Analytis, J. G.; Liu, Z. K.; Igarashi, K.; Kuo, H.-H.; Qi, X. L.; Mo, S. K.; Moore, R. G.; Lu, D. H.; Hashimoto, M.; Sasagawa, T.; Zhang, S. C.; Fisher, I. R.; Hussain, Z.; Shen, Z. X. *Science* **2010,** 329, (5992), 659-662.

130. Hor, Y. S.; Roushan, P.; Beidenkopf, H.; Seo, J.; Qu, D.; Checkelsky, J. G.; Wray, L. A.; Hsieh, D.; Xia, Y.; Xu, S. Y.; Qian, D.; Hasan, M. Z.; Ong, N. P.; Yazdani, A.; Cava, R. J. *Physical Review B* **2010,** 81, (19), 195203.

131. Yu, R.; Zhang, W.; Zhang, H. J.; Zhang, S. C.; Dai, X.; Fang, Z. *Science* **2010,** 329, (5987), 61-64.

132. Zhu, J. J.; Yao, D. X.; Zhang, S. C.; Chang, K. *Phys Rev Lett* **2011,** 106, (9).

133. Liu, Q.; Liu, C. X.; Xu, C. K.; Qi, X. L.; Zhang, S. C. *Phys Rev Lett* **2009,** 102, (15).

134. Ruderman, M. A.; Kittel, C. *Phys Rev* **1954,** 96, (1), 99-102.

135. Yosida, K. *Phys Rev* **1957,** 106, (5), 893-898.

136. Jungwirth, T.; Sinova, J.; Masek, J.; Kucera, J.; MacDonald, A. H. *Rev Mod Phys* **2006,** 78, (3), 809-864.

137. He, L.; Xiu, F. X.; Yu, X. X.; Teague, M.; Jiang, W. J.; Fan, Y. B.; Kou, X. F.; Lang, M. R.; Wang, Y.; Huang, G.; Yeh, N. C.; Wang, K. L. *Nano Lett* **2012,** 12, (3), 1486-1490.

138. Analytis, J. G.; McDonald, R. D.; Riggs, S. C.; Chu, J. H.; Boebinger, G. S.; Fisher, I. R. *Nature Physics* **2010,** 6, (12), 960-964.

139. Arakane, T.; Sato, T.; Souma, S.; Kosaka, K.; Nakayama, K.; Komatsu, M.; Takahashi, T.; Ren, Z.; Segawa, K.; Ando, Y. *Nat Commun* **2012,** 3.

140. Hong, S. S.; Cha, J. J.; Kong, D. S.; Cui, Y. *Nat Commun* **2012,** 3.

141. Luo, W.; Qi, X.-L. *Physical Review B* **2013,** 87, (8), 085431.

142. Eremeev, S. V.; Men'shov, V. N.; Tugushev, V. V.; Echenique, P. M.; Chulkov, E. V. *Physical Review B* **2013,** 88, (14), 144430.

143. Vobornik, I.; Manju, U.; Fujii, J.; Borgatti, F.; Torelli, P.; Krizmancic, D.; Hor, Y. S.; Cava, R. J.; Panaccione, G. *Nano Letters* **2011,** 11, (10), 4079-4082.

144. Wei, P.; Katmis, F.; Assaf, B. A.; Steinberg, H.; Jarillo-Herrero, P.; Heiman, D.; Moodera, J. S. *Physical Review Letters* **2013,** 110, (18), 186807.

145. Yang, Q. I.; Dolev, M.; Zhang, L.; Zhao, J.; Fried, A. D.; Schemm, E.; Liu, M.; Palevski, A.; Marshall, A. F.; Risbud, S. H.; Kapitulnik, A. *Physical Review B* **2013,** 88, (8), 081407.

146. Uchida, K.-i.; Adachi, H.; Ota, T.; Nakayama, H.; Maekawa, S.; Saitoh, E. *Applied Physics Letters* **2010,** 97, (17), 172505-3.

147. Jiang, W.; Upadhyaya, P.; Fan, Y.; Zhao, J.; Wang, M.; Chang, L.-T.; Lang, M.; Wong, K. L.; Lewis, M.; Lin, Y.-T.; Tang, J.; Cherepov, S.; Zhou, X.; Tserkovnyak, Y.; Schwartz, R. N.; Wang, K. L. *Physical Review Letters* **2013,** 110, (17), 177202.

148. Serga, A. A.; Chumak, A. V.; Hillebrands, B. *Journal of Physics D: Applied Physics* **2010,** 43, (26), 264002.

149. Kelly, O. d. A.; Anane, A.; Bernard, R.; Youssef, J. B.; Hahn, C.; Molpeceres, A. H.; Carretero, C.; Jacquet, E.; Deranlot, C.; Bortolotti, P.; Lebourgeois, R.; Mage, J. C.; de Loubens, G.; Klein, O.; Cros, V.; Fert, A. *Applied Physics Letters* **2013,** 103, (8), 082408-4.

150. Goto, T.; Onbasli, M. C.; Ross, C. A. *Opt. Express* **2012,** 20, (27), 28507-28517.

151. Sun, Y.; Song, Y.-Y.; Chang, H.; Kabatek, M.; Jantz, M.; Schneider, W.; Wu, M.; Schultheiss, H.; Hoffmann, A. *Applied Physics Letters* **2012,** 101, (15), 152405-5.

152. Jiang, Y.; Wang, Y.; Sagendorf, J.; West, D.; Kou, X.; Wei, X.; He, L.; Wang, K. L.; Zhang, S.; Zhang, Z. *Nano Letters* **2013,** 13, (6), 2851-2856.

153. Checkelsky, J. G.; Hor, Y. S.; Cava, R. J.; Ong, N. P. *arXiv:1003.3883v1 [cond-mat.mes-hall]* **2010**.

154. Eto, K.; Ren, Z.; Taskin, A. A.; Segawa, K.; Ando, Y. *Phys. Rev. B* **2010,** 81, (19), 195309.

155. Analytis, J. G.; Chu, J. H.; Chen, Y. L.; Corredor, F.; McDonald, R. D.; Shen, Z. X.; Fisher, I. R. *Phys. Rev. B* **2010,** 81, (20), 205407.

156. Wang, J.; DaSilva, A. M.; Chang, C.-Z.; He, K.; Jain, J. K.; Samarth, N.; Ma, X.-C.; Xue, Q.-K.; Chan, M. H. W. *Physical Review B* **2011,** 83, (24), 245438.

157. O'handley, R. C., *Modern magnetic materials: principles and applications*. Wiley New York: 2000; Vol. 830622677.

158. Geller, S.; Espinosa, G. P.; Crandall, P. B. *Journal of Applied Crystallography* **1969,** 2, (2), 86-88.

159. Sposito, A.; May-Smith, T. C.; Stenning, G. B. G.; de Groot, P. A. J.; Eason, R. W. *Opt. Mater. Express* **2013,** 3, (5), 624-632.

160. Clark, A. E.; Strakna, R. E. *Journal of Applied Physics* **1961,** 32, (6), 1172-1173.

161. Spencer, E. G.; Denton, R. T.; Bateman, T. B.; Snow, W. B.; Van Uitert, L. G. *Journal of Applied Physics* **1963,** 34, (10), 3059-3060.

162. Wray, L. A.; Xu, S.-Y.; Xia, Y.; Hsieh, D.; Fedorov, A. V.; Hor, Y. S.; Cava, R. J.; Bansil, A.; Lin, H.; Hasan, M. Z. *Nat Phys* **2011,** 7, (1), 32-37.

163. Levy, P. M.; Zhang, S. *Physical Review Letters* **1997,** 79, (25), 5110-5113.